

UC San Diego

UC San Diego Electronic Theses and Dissertations

Title

The Use of Light, Ultrasound, and their Combination in the Diagnosis and Localized Treatment of Cancer /

Permalink

<https://escholarship.org/uc/item/8z41x8d5>

Author

Schutt, Carolyn Elizabeth

Publication Date

2013

Peer reviewed|Thesis/dissertation

UNIVERSITY OF CALIFORNIA, SAN DIEGO

The Use of Light, Ultrasound, and their Combination in the Diagnosis and Localized
Treatment of Cancer

A dissertation submitted in partial satisfaction of the requirements for the degree
Doctor of Philosophy

in

Bioengineering

by

Carolyn Elizabeth Schutt

Committee in charge:

Professor Sadik Esener, Chair
Professor Michael Heller, Co-Chair
Professor Michael Berns
Professor Robert Mattrey
Professor John Watson

2013

Copyright

Carolyn Elizabeth Schutt, 2013

All rights reserved.

The Dissertation of Carolyn Elizabeth Schutt is approved, and it is acceptable in quality and form for publication on microfilm and electronically:

Co-Chair

Chair

University of California San Diego

2013

DEDICATION

To my parents, who kept buying me chemistry sets for Christmas and never stopped encouraging my curiosity, even when asked “*why?*” or “*how?*” for the millionth time. I am forever grateful for your love and support.

To my husband and best friend, who has remained an unwavering pillar of support and encouragement. I am forever blessed that I get to spend my life with you as we explore the *why's* and *how's* of everything.

EPIGRAPH

The universe is full of magical things patiently waiting for our wits to grow sharper.

Eden Phillpots

Life is the bubbles

Sebastian the crab
“Under the Sea” (Howard Ashman)

TABLE OF CONTENTS

SIGNATURE PAGE	iii
DEDICATION	iv
EPIGRAPH	v
TABLE OF CONTENTS	vi
LIST OF FIGURES	xi
LIST OF TABLES	xv
ACKNOWLEDGEMENTS	xvi
VITA.....	xxi
ABSTRACT OF THE DISSERTATION.....	xxiii
Introduction	1
Overview: A Localized Approach for Cancer Detection and Therapy	1
Localization of Detection.....	1
Acousto-fluorescent Contrast Agent Approach	2
Drug Delivery Localization	4
Ultrasound-Controlled Microcapillary Damage Approach.....	5
Chemotherapy Prodrug Approaches	6
Photoactivatable Chemotherapy Prodrug Nanoparticles	6
Dissertation Organization	8
Chapter 1.....	9
Toward Optical Tumor Microenvironment Characterization: Manipulating Nanoscale Features on the Surface of Dye-Loaded Microbubbles to Increase their Ultrasound- Modulated Fluorescence Output	
Abstract	10

Introduction.....	11
Methods and Materials.....	17
Materials	17
Microbubble Manufacturing.....	18
Microbubble Temperature Treatment.....	19
3D Structured Illumination Super-Resolution Microscopy.....	20
Acousto-Fluorescence Detection System and Signal Acquisition	20
Acousto-Fluorescence Signal Analysis Program	22
Results.....	23
Microbubble Manufacturing and Temperature Treatment	23
Ultrasound-Modulated Fluorescence Signal Analysis	29
Discussion.....	33
Conclusion.....	37
Acknowledgements.....	38
Chapter 2.....	39
Increasing the Signal to Noise Ratio for the Detection of Modulated Fluorescence Generated by Ultrasound-Driven Dye-Loaded Microbubbles in Scattering Media	
Abstract.....	40
Introduction.....	41
Materials and Methods.....	47
Materials.....	47
Microbubble Preparation	47
Harmonic Signal Detection	47
Fundamental Frequency Detection in Scattering Media	48

Results.....	50
Harmonic Signal Detection	50
Fundamental Frequency Detection in Scattering Media	55
Discussion.....	57
Conclusions.....	60
Chapter 3.....	62
Toward Ultrasound-Enhanced Drug Delivery: The Influence of Distance Between Microbubbles on the Fluid Flow Produced During Ultrasound-Mediated Inertial Cavitation	
Abstract.....	63
Introduction.....	64
Materials and Methods.....	68
Materials.....	68
Microbubble Fabrication	69
Ultrasound Exposure	70
Video Analysis	73
Results.....	74
Debris Cloud Observation	74
Analysis of Debris Cloud Shape Dependence on Inter-Microbubble Distance and Microbubble Size.....	76
Discussion.....	81
Conclusions.....	84
Acknowledgements.....	85

Chapter 4.....	86
Toward Light-Activated Localized Prodrug Nanoparticle Therapy: Drug Delivery Nanoparticles formed from Light-Activated Doxorubicin Prodrug Monomers	
Abstract.....	87
Introduction.....	88
Materials and Methods.....	93
Materials.....	93
DOX-PCB Nanoparticle Synthesis.....	93
Particle Characterization.....	94
Light Activated Drug Release Characterization.....	95
Cellular Localization.....	97
Cytotoxicity.....	99
Results.....	100
Particle Characterization.....	100
Light-Activated Drug Release Characterization.....	102
Cellular Localization.....	103
Cytotoxicity.....	105
Discussion.....	106
Conclusions.....	108
Acknowledgements.....	108
Dissertation Conclusions.....	110
Acousto-Fluorescent Contrast Agent Development.....	110
Acousto-Fluorescent Contrast Agent Detection.....	111
Investigation of Inter-microbubble Distance on Fluid Jet Direction.....	111

Photoactivatable Chemotherapy Prodrug Nanoparticles	112
Dissertation Future Directions.....	113
References	116

LIST OF FIGURES

Figure 1.1 Schematic representation of fluorescence intensity modulation (“blinking”) mechanism.	14
Figure 1.2 Conventional imaging of DiI surface-loaded microbubbles.	24
Figure 1.3 Super-resolution microscopy images of surface-loaded fluorescent microbubbles prepared with various temperature treatment regimens.	26
Figure 1.4 Example time and frequency domain signals acquired from rapid-cooled microbubbles and bubbles that were not temperature-treated.	28
Figure 1.5 The percentage of microbubbles that displayed detectable fluorescence modulation under different temperature treatment regimens.	31
Figure 1.6 Batch-to-batch variability of the fluorescence modulation percentage for each temperature treatment regimen.	32
Figure 2.1 Schematic of the acousto-optic detection setup used to collect the modulated fluorescence signal from the dye loaded microbubbles.	50

Figure 2.2 Example time and frequency domain signals acquired from rapid-cooled microbubbles that displayed harmonic signals and bubbles that were not temperature-treated. 51

Figure 2.3 Percentage of microbubbles produced under the different thermal treatment processes that displayed a detectable 2nd, 3rd, and 4th harmonic signal. 53

Figure 2.4 Batch-to-batch variability of the detectable harmonic fluorescence modulation percentage for each temperature treatment. 54

Figure 2.5 The lock-in amplifier signal to noise ratio (SNR) for both the fluorescence modulated and scattered light modulated signals versus the reduced scattering coefficient of the media. 57

Figure 3.1 Schematic diagram of the microscope system used to observe and record the interaction of the fluorescent microbubbles with the focused ultrasound. 71

Figure 3.2 Still frames from videos showing examples of the three categories of debris cloud expansion. 75

Figure 3.3 Three microbubbles are in physical contact with one another before ultrasound exposure. 76

Figure 3.4 Box plots of the distance between the microbubble and its nearest neighbor in microns for each of the three debris cloud expansion categories.....	78
Figure 3.5 Box plots for the diameter of the microbubbles in each of the three debris cloud expansion categories.....	79
Figure 3.6 Scatter plot showing the diameters of the microbubbles plotted against distance between the microbubble and its nearest neighbor.	80
Figure 4.1 Molecular structure of DOX-PCB. The DOX molecule is attached to a photocleavable nitrophenyl compound that has a short polyethylene glycol linker attached to a biotin molecule at the opposite end.....	92
Figure 4.2 Three dimensional conformation structure of the DOX-PCB prodrug monomer.....	92
Figure 4.3 Scanning electron microscope image of the DOX-PCB nanoparticles produced by the nanoprecipitation process of the DOX-PCB monomer. The wide field view shows the uniformity of the nanoparticle structures. Inset: SEM image of a single DOX-PCB nanoparticle.....	102
Figure 4.4 The concentration of released DOX from the DOX-PCB nanoparticles increased linearly with the duration of 365 nm light exposure ($R^2 = .93$).	103

Figure 4.5 Light microscopy images of DOX and DOX-PCB nanoparticle localization within live PTK2 kidney epithelial cells.. 104

Figure 4.6 Cell toxicity results on human lung cancer cells of DOX-PCB prodrug nanoparticles, photoactivated DOX-PCB nanoparticles and free DOX. DOX-PCB prodrug nanoparticles 105

LIST OF TABLES

Table 1.1 Data summary for Figure 1.5 showing the bubble count that exhibited fluorescence modulation and no modulation for various temperature treatments.	32
Table 2.1 Summary of the absolute numbers of microbubbles made under different thermal treatment regimens that displayed detectable higher harmonic signal production.....	55
Table 3.1 Summary of microbubble data acquired from video analysis.	77
Table 4.1 Characterization of DOX-PCB nanoparticle size and zeta potential (mean \pm standard deviation).....	101

ACKNOWLEDGEMENTS

I am incredibly grateful to have had the opportunity to work with some remarkable individuals during my graduate school career. These people have shaped both my intellectual and personal development in a multitude of ways.

I would like to thank Professor Sadik Esener for being an extraordinary mentor and Ph.D. advisor. His support and confidence in me has had an immeasurable impact on my personal and scientific development. He is truly inspiring in his ability to cross disciplines and his willingness to consider and develop out-of-the-box solutions. From him I have learned volumes about the process of innovation and how to cultivate the right environment to make that happen. I have truly benefitted from watching his inspiring example of how to be a successful innovator while always treating one's colleagues with dignity and respect.

I am also grateful to Professor John Watson for his guidance as a member of my committee and his valuable perspective on translation of technology to the clinic. Additionally, his mentorship in the Bioengineering community has helped me to develop my leadership skills and become a more effective advocate for bioengineering research and engineering education.

Professor Robert Mattrey has my utmost appreciation for sharing with me his valuable clinical perspective and wealth of expertise in ultrasonography and medical imaging. I appreciate the many discussions we've had about my various projects and the support and encouragement he has provided all along the way.

Professor Michael Berns deserves special recognition for his valuable advice and perspective on my projects, especially in the areas of microscopy and cell replication. I truly appreciate his willingness to discuss the details of my projects and help me find ways to answer the important questions. His expertise and guidance has been a truly valued resource.

Professor Michael Heller deserves gratitude for being a very supportive member of my committee. I am grateful for him always being willing to talk and discuss new ideas. I am inspired by his contagious zeal and enthusiasm for research as well as his untiring dedication to the success of his students. I always learn something new and interesting from our conversations.

My colleagues in the Esener lab group have contributed immensely to my intellectual development and provided the morale boost that comes with working with great people. I first want to thank Stuart Ibsen for his support and advice on many projects. His insights and experience in photocleavable prodrug development, signal processing and the microscopy monitoring of ultrasound interactions have been truly invaluable. Our spirited discussion and debate has led to many new and exciting ideas. His perseverance and tenacity in the face of challenges has been an inspiration to me along with his contagious enthusiasm and sense of wonder. Mark Hsu and Michael Benchimol are greatly appreciated for their guidance and assistance especially in the areas of optics and electrical engineering. I have enjoyed our many discussions and their insights and advice have been a great help to me along the way. Inanc Ortac deserves recognition for his help in the lab and his fun uplifting presence. I have shared many great conversations with Gen Yong and Ya-san Yeh and appreciate their

advice and assistance. I have enjoyed working with Sahar Baghdadchi and appreciate her insights and discussion in the areas of optics and electronics. I am also grateful to Rebecca Saenz for helping to teach me how to do tissue culture work and for her friendship in the lab. Dr. Andrew Goodwin is appreciated for his perspectives on microbubble development. I appreciate Corbin Clawson for his caring personality and advice in the early stages of my graduate work. I am also thankful to Marta Sartor for her laughter and help in the lab in the first few years. Ahmet Erten also deserves recognition for his help and the humor he brought to our conversations. Negin Mokhtari, Mukanth Vaidyanathan and Jinous Valizadeh are also appreciated colleagues who have helped to enrich my experience. Through all of the lunches and lab meetings, I am lucky to have these individuals as colleagues and friends.

I have been truly fortunate to work with some very bright and dedicated undergraduate students. I am grateful to Selin Esener, Stacey Kuo and William Thrift for their assistance and contributions in the lab. I appreciate the efforts of Rachel Ellena, Hima Potu, and Edward Tunggaldjaja in their Senior Design Project work. I have enjoyed working with all of these students and appreciate the enthusiasm and fresh perspectives that they have brought to the research. I know that they all have bright futures ahead.

I am grateful to Dr. Linda Shi and Dr. Michelle Duquette-Huber of the Berns Laboratory for their advice and help with the DOXPCB cell localization studies. Thanks also to Nick Hyun of the Berns Lab for his supportive and kind presence.

I appreciate the advice and perspectives of Eran Zahavy on the photocleavable prodrug work. He is a truly creative and dedicated researcher and I have learned a lot from him and his approaches to problem solving.

I am grateful to Professor Liangfang Zhang for keeping his door open to me for our discussions of aspects of nanoparticle development over the past few years. His expertise and insights have been very helpful.

Dr. Santosh Aryal deserves much recognition for his help with chemistry advice and nanoparticle imaging. His friendly personality and generosity in sharing his expertise are truly appreciated.

I am grateful to Professor David Hall for his advice and assistance in the areas of fluorescence imaging, optics and photophysics. I appreciate our varied and enthusiastic discussions and admire his creative ideas and perspectives.

Dr. Ebonee Williams also deserves recognition for her support and mentorship in the area of engineering leadership. Her advice and encouragement has been a treasured resource during my graduate career.

I also want to thank my other colleagues and friends from the UCSD Moores Cancer Center and Jacobs School of Engineering over the years including Sergio Sandoval, Natalie Mendez, Ila Bharati Summitt, Diahn Futalan, Wenjin Cui, Guixin Shi, Laura Restrepo, and many others. I appreciate all of the conversations, advice, laughter, and varied perspectives on life and research that you have shared with me.

I am also grateful to the UCSD Department of Bioengineering personnel and all of my professors for providing me with my educational foundation and helping to guide me along my path as an engineering student and researcher.

Finally, I want to thank my family, especially my Mom, Dad, and brother for their continuous support and encouragement throughout my education. Their belief in me and support of my interests in engineering has made a huge difference in my life.

The following co-authors have contributed significantly to the work presented in each chapter. I am grateful for their help, insight, and contributions.

Chapter 1, in part, has been submitted for publication of the material as it may appear in Small, 2014, Carolyn Schutt, Stuart Ibsen, Michael Benchimol, Mark Hsu, Sadik Esener, Wiley-VCH 2014. The dissertation author was the primary investigator and author of this paper.

Chapter 2, in part, is currently being prepared for submission for publication of the material. Carolyn Schutt, Stuart Ibsen, Michael Benchimol, Mark Hsu, Sadik Esener. The dissertation author was the primary investigator and author of this material.

Chapter 3, in full, has been submitted for publication of the material as it may appear in the Journal of the Acoustical Society of America, 2014, Carolyn Schutt, Stuart Ibsen, William Thrift, Sadik Esener, Acoustical Society of America 2014. The dissertation author was the primary investigator and author of this paper.

Chapter 4, in full, is currently being prepared for submission for publication of the material. Carolyn Schutt, Stuart Ibsen, Eran Zahavy, Santosh Aryal, Michael Berns, Sadik Esener. The dissertation author was the primary investigator and author of this material.

VITA

Bachelor of Science, Bioengineering; June 2007
University of California San Diego, La Jolla, CA

Master of Science, Bioengineering; December 2009
University of California San Diego, La Jolla, CA

Doctor of Philosophy, Bioengineering; December 2013
University of California San Diego, La Jolla, CA

PUBLICATIONS

- C Schutt, S Ibsen, E Zahavy, S Aryal, M Berns, and S Esener. Drug Delivery Nanoparticles formed from Light-Activated Doxorubicin Prodrug Monomers. In preparation for submission.
- C Schutt, S Ibsen, M Benchimol, M Hsu, and S Esener. Effect of Microbubble Shell Lipid Partitioning on High Order Harmonic Fluorescence Modulations. In preparation for submission.
- C Schutt, S Ibsen, M Benchimol, M Hsu, and S Esener. Increasing the Ultrasound-Modulated Fluorescence Output of Dye-Loaded Microbubbles by Manipulating their Nanoscale Surface Features. Under review at Small.
- C Schutt, S Ibsen, W Thrift, and S Esener. The Influence of Distance Between Microbubbles on the Resulting Shape of Ultrasound-Induced Inertial Cavitation Shockwaves. Under review at JASA.
- S Ibsen, R Mora, G Shi, C Schutt, W Cui, M Benchimol, V Serra, and S Esener. Removal of Ligand Bound Liposomes from Cell Surfaces by Microbubble Inertial Cavitation. Under review at JASA.
- S Ibsen, C Schutt, and S Esener. Microbubble-mediated Ultrasound Therapy: A Review of its Potential in Cancer Treatment. *Drug Design, Development and Therapy*. 2013(7): 375-388 (2013).
- M Benchimol, M Hsu, C Schutt, D Hall, R Mattrey, and S Esener. Phospholipid/carbocyanine Dye-Shelled Microbubbles as Ultrasound-Modulated Fluorescent Contrast Agents. *Soft Matter*. 9(8): 2384-2388 (2013).

- C Schutt, M Benchimol, M Hsu, and S Esener. Ultrasound-Modulated Fluorescent Contrast Agent for Optical Imaging through Turbid Media. *Unconventional Imaging, Proc. SPIE 8165*: 81650B1-B7 (2011).
- S Ibsen, M Benchimol, D Simberg, C Schutt, J Steiner, and S Esener. A Novel Nested Liposome Drug Delivery Vehicle Capable of Ultrasound Triggered Release of its Payload. *J Control Release*. 155(3): 358-356 (2011).
- Q Zhang, Z Wang, H Ran, X Fu, X Li, Y Zheng, M Peng, M Chen, and C Schutt. Enhanced Gene Delivery into Skeletal Muscles with Ultrasound and Microbubble Techniques. *Academic Radiology*. 12(3): 262-267 (2006).

FIELDS OF STUDY

Major Field: Bioengineering

Studies in Drug Delivery and Light-Based Cancer Diagnostics
Professor Sadik Esener

ABSTRACT OF THE DISSERTATION

The Use of Light, Ultrasound, and their Combination in the Diagnosis and Localized Treatment of Cancer

by

Carolyn Elizabeth Schutt

Doctor of Philosophy in Bioengineering

University of California, San Diego, 2013

Professor Sadik Esener, Chair

Professor Michael Heller, Co-Chair

The small size of early stage tumors makes them difficult to detect and treat given current techniques that are applied at a systemic level. Addressing these challenges requires a shift from whole-body approaches to localized strategies. Localized light generation within a small tissue volume can yield spatially-resolved chemical information about the tissue microenvironment. This could help differentiate small cancerous lesions from benign masses enabling the detection of smaller, earlier-

stage tumors. The detection of this locally-generated light is made difficult by the highly-scattering nature of biological tissue. A process was developed here to create fluorescent microbubbles that generate light in the small focal zone of an ultrasound beam by consistently modulating their fluorescence intensity. By amplifying these characteristic intensity modulations with a lock-in amplifier, the fluorescence from these locally-activated microbubbles was detected in a light-scattering environment. It was shown that these microbubbles also displayed harmonic oscillations beyond the ultrasound driving frequency which could be used to further improve the signal to noise ratio for detection.

Once a tumor is detected, localizing treatment to just the tumor volume can reduce systemic side effects. Localized drug deposition can be achieved by using ultrasound to damage the tumor microcapillaries. Fluid jets that are formed through the inertial cavitation of microbubbles in the ultrasound focal zone can increase the level of damage, especially if they are directed horizontally along the capillary surface. Data presented here shows that shorter distances between microbubble pairs at the time of ultrasound exposure significantly increased the chances of this horizontally-oriented jet formation.

Another localized treatment technique uses locally-delivered light to activate a photocleavable prodrug. Manufacturing techniques developed here created nanoparticles that consisted entirely of photocleavable prodrug monomers. The particles were 30 times less toxic than the pure active drug. Pure active chemotherapy drug was released from the particles only when exposed to the light and was shown to

kill tumor cells. The nanoparticle form of the chemotherapy prodrug monomers will increase their circulation time and allow tumor accumulation by extravasation.

Introduction

Overview: A Localized Approach for Cancer Detection and Therapy

The goal of detecting and treating cancer at the earliest possible stage is itself a scientific challenge but the realization of that goal presents a second challenge as well. By treating tumors earlier the chances of long-term survival increase [1] thus making the long-term health problems from the side effects of current chemotherapy a major concern [2]. Both the detection and the treatment of cancer can be improved by using a localized approach. By localizing the detection scheme, detailed analysis can be made point by point through a tissue region to look for signs of a tumor. Once found, localized techniques can be used to kill the tumor cells reducing harmful systemic side effects. The work conducted in this dissertation looks to increase the localization of both the detection and treatment of cancer by using light, ultrasound, and their combination in unique ways.

Localization of Detection

Current imaging techniques of ultrasound [3-5], magnetic resonance imaging (MRI) [6-8], computed tomography scanning (CT scan) [9], and even simple 2D X-ray images [10] can detect dense tissue masses that do not belong in a region of healthy tissue. However, in many cases, especially if the mass is small, there is difficulty in specifying whether the observed mass is malignant or benign [11]. In the case of breast cancer, x-ray mammography is the most frequently employed imaging

method for early diagnosis. X-ray mammograms suffer from poor diagnostic accuracy, with a high rate of positive mammogram results being false positives [11]. False positive results can lead to unnecessary, painful biopsies yielding benign lesions. The ability to obtain information about the chemical environment within the mass, especially the presence of hypoxic regions [12], would allow the determination of malignancy to be much more accurate and allow lesions to be caught at earlier stages [13, 14]. Optical fluorescence detection is a highly sensitive modality which can be used to determine the chemical nature of a sample. This can be done through the use of chemically-sensitive dyes or techniques which relate light absorption to molecular content [15, 16]. However, when using these optical techniques inside the body, the tissue scatters light to such a high degree [17] that it is very difficult to tell whether or not detected photons have passed through the suspected mass. Ultrasound, in contrast, experiences significantly less scatter in the body and can easily be focused to small volumes within deep tissue [18]. Designing a particle that can interact with the ultrasound focal zone to produce fluorescence that changes in intensity at a known frequency would help solve this scattering problem by localizing the origin of this “blinking” fluorescence to the tumor tissue. This fluorescence intensity-modulating signal can be detected at the surface of the body and will be known to originate from photons that have passed through the tumor.

Acousto-fluorescent Contrast Agent Approach

A particle that changes its fluorescence intensity in response to focused ultrasound can be designed by taking advantage of the physical interaction between

ultrasound and microbubbles of gas. Due to the compressibility of gas, microbubbles undergo radial size oscillations in response to ultrasound when exposed to the compression and rarefaction portions of an ultrasound pulse [19-22]. By loading the lipid-coated surface of the microbubble with a fluorophore that quenches itself in close proximity, the ultrasound-induced size oscillations translate to changes in fluorophore surface density, creating a particle that modulates its fluorescence emission intensity at the applied ultrasound frequency. Recent efforts from our research group have provided an initial experimental demonstration of these fluorescence-modulating microbubbles [23, 24]. However, only a small subpopulation of these microbubbles was observed to produce fluorescence modulations. This presents a significant challenge for detecting the fluorescence signal in a light-scattering environment. A robust and consistent fluorescence modulation signal is required for the use of detectors that lock on to the blinking frequency and extract the signal from the large background of scattered light that did not originate from the ultrasound focus. The work of the first chapter of this dissertation is aimed at modifying the surface nanostructure of these contrast agent microbubbles to enhance their ability to produce detectable fluorescence intensity modulations in response to ultrasound. The second chapter of this dissertation develops strategies to increase the signal to noise ratio for the detection of these contrast agents, including the production of higher harmonic fluorescence modulation signals. This chapter also demonstrates the ability to now detect these enhanced microbubble fluorescence modulations in a light-scattering media.

Drug Delivery Localization

The major challenge with chemotherapy drugs lies in the fact that most are designed to affect all rapidly dividing cells [25]. This can be very effective for tumors that are well developed and actively growing [26], but for smaller tumors that are earlier in their development the cells may not be replicating nearly as fast [27-29]. In these cases the drugs will have less effect on these slower growing cells requiring prolonged exposures to produce a therapeutic effect. The goal is to expose the tumor to the highest concentration of chemotherapy drugs for the longest time possible. However, the chemotherapy drugs also have systemic effects on the replication of normal non-tumor cells which creates potentially harmful short-term and long-term side effects, especially if doses are prolonged [30, 31]. These side effects include neutropenia [30] which can leave cancer patients susceptible to serious infection and cause potentially detrimental delays and reductions in a patient's chemotherapy dose. Of particular concern are long-term side effects such as cardiotoxicity which can result in the appearance of cardiomyopathy and congestive heart failure after many years of latency post-treatment [32]. As the chances of long-term cancer survival increase, these latent side effects become a major issue. Localized chemotherapeutic delivery approaches can reduce these side effects by creating elevated drug exposure in the tumor and restricting the exposure seen by healthy tissues.

Ultrasound-Controlled Microcapillary Damage Approach

One way to help deliver more therapeutic into the tumor for a longer period of time is to cause damage to the tumor capillaries [33, 34]. This damage and endothelial cell dislodgment can allow more drug molecules or slow-release drug delivery nanoparticles to extravasate from circulation into the tumor tissue. This extravasation enhancement is important for smaller tumors where the characteristic tumor “leaky” vasculature [35] may not have developed [28, 29], leaving these tumors with a reduced capability to accumulate drug molecules or nanoparticles via extravasation compared to larger tumors. Capillary disruption can be effectively localized by using focused ultrasound [18]. The use of microbubbles can increase the extent of capillary damage because they cause a local dissipation of the ultrasound wave energy through the creation of an inertial cavitation shockwave. Microbubbles that undergo inertial cavitation while in contact with a rigid or flexible boundary form fluid jets that are directed perpendicularly toward the boundary surface [36-38]. While the formation of this perpendicular jet can be used to create microcapillary damage, the damage could be enhanced by influencing the concentrated jet to have a directional component that is oriented horizontally along the capillary surface, affecting a larger surface area. Chapter 3 of this dissertation investigates the influence of inter-microbubble distance on this horizontal directional component of jet formation and their ability to create localized microcapillary damage. Designing microbubbles to produce this enhanced localized disruption of the capillary wall would be beneficial for many drug delivery scenarios and antitumor applications.

Chemotherapy Prodrug Approaches

Another strategy to localize drug delivery is through the use of a prodrug. Prodrugs are chemically-modified versions of an active drug that reduce its toxicity to all tissues with the goal of restoring the drug's therapeutic properties when triggered [39-41]. Most prodrug designs rely on inherent differences between the tumor and the healthy tissue as a trigger. These include biochemical and environmental differences such as enzymatic cleavage by enzymes that are over secreted by the tumor [42-44], and tumor-associated hypoxia or low pH [45, 46]. Another possible prodrug activation scheme involves receptor-mediated endocytosis triggered by antibody/tumor antigen binding to tumor cell surface proteins with subsequent drug activation in the low pH environment of the intracellular endosome [47]. Prodrugs that rely on biochemical triggers to release active drugs have specificity problems because the tumor microenvironment can be shared with other tissues within the body [48, 49]. Light can be used as an alternative prodrug trigger to avoid this uncontrolled biochemical activation [50]. The light exposure can be localized to the tumor tissue by using fiber optics and light emitting diode technology [51].

Photoactivatable Chemotherapy Prodrug Nanoparticles

A nanoparticle comprised of light-activatable chemotherapy prodrug would offer additional advantages for localized delivery. A nanoparticle form could enhance circulation time of the prodrug, allowing the particles to accumulate in tumors by extravasation through any tumor-associated discontinuous endothelium [52, 53]. A prodrug nanoparticle could also be functionalized to allow targeted delivery and to

allow for active uptake via endocytosis which could deliver more prodrug to the tumor cells. The work in Chapter 4 of this dissertation focuses on the development, characterization and biological effects of a new class of nanoparticle formed entirely of photocleavable chemotherapy prodrug monomers.

The strategies of localized acousto-fluorescence detection and localized ultrasound-mediated and light-activated therapy developed in this dissertation could potentially be used in concert to develop an entirely localized approach to cancer detection and treatment. A tumor that is detected and spatially resolved in the body can become the activation zone for an ultrasound or light-activated localized chemotherapy dose.

Dissertation Organization

This dissertation is organized into four chapters.

Chapter 1 uses thermal treatment techniques to manipulate the nanoscale surface of fluorescent contrast agent microbubbles, creating a more even distribution of lipophilic dye. This homogeneous distribution was shown to significantly increase the fraction of microbubbles that would produce detectable fluorescence modulation when exposed to ultrasound.

Chapter 2 documents the ability of the surface-modified microbubbles described in Chapter 1 to produce ultrasound-induced higher harmonic fluorescence modulations that can be used to enhance the signal-to-noise ratio for detection in tissue. This chapter also documents the ability of the surface-modified microbubbles described in Chapter 1 to be detected in a light-scattering environment through the use of a lock-in amplifier.

Chapter 3 establishes a correlation between the inter-microbubble distance of microbubble pairs and the horizontal directional component of the fluid jet formed when the microbubbles are exposed to ultrasound.

Chapter 4 focuses on the design, synthesis, and biological effects of a new type of drug delivery nanoparticle that is entirely composed of light activated prodrug monomers.

Chapter 1

Toward Optical Tumor Microenvironment Characterization:

Manipulating Nanoscale Features on the Surface of Dye-Loaded
Microbubbles to Increase their Ultrasound-Modulated Fluorescence
Output

Abstract

Developing an optical contrast agent that can generate light would help overcome some of the major challenges of deep tissue optical analysis. One class of contrast agents considered here are microbubbles of perfluorocarbon gas stabilized with lipid monolayer coatings which have an extensive history of use as ultrasound contrast agents. The compressibility of the gas allows the bubbles and their lipid monolayers to expand and contract with the ultrasound pressure waves resulting in high ultrasound reflectivity. The different lipid species that form the monolayer can distribute and partition in various ways including the formation of concentrated lipid islands. In this study the dynamics of how these nanoscale islands accommodate the expansion of the microbubbles are monitored by measuring the fluorescence intensity changes that occur as self-quenching lipophilic dye molecules embedded in the lipid monolayer change their distance from one another. It was found that when the dye molecules were concentrated in islands, only 5% of the microbubbles displayed measurable fluorescence intensity modulation indicating the islands were not able to expand sufficiently for the dye molecules to separate from one another. When the microbubbles were heated and cooled rapidly through the lipid transition temperature the islands were melted creating an even distribution of dye about the entire monolayer. This resulted in over 50% of the microbubbles displaying the fluorescence-modulated signal indicating that the dye molecules could now separate sufficiently to change their self-quenching efficiency. This has significant impact in improving the future efficacy of these microbubbles as optical contrast agents for deep

tissue imaging. Uniform lipid distributions are also important for microbubble applications that involve crosslinking the surface to increase microbubble stiffness and impart resistance to low intensity imaging ultrasound. Homogeneous distribution of lipid species on the microbubble surface also allows for a uniform surface PEG coating which has implications on microbubble circulation time, storage life, and the efficiency of ligand-based targeting.

Introduction

Generating light inside the body has the potential to overcome many of the challenges currently facing optical imaging in deep tissue. Current methods of optical analysis of tissue involve illuminating the body surface with light to allow the photons to penetrate into a region of interest and then detecting the photons that scatter their way back to the tissue surface. The photons are highly scattered by the tissue making their actual paths unknown for depths greater than 2-3 mm [54]. This makes it difficult to optically probe a specific tissue region of interest because it is unknown if detected photons actually passed through that region. There is also a large background of detected photons that did not pass through the region of interest. Generating a beacon of light at a known location within the deep tissue and detecting the photons at the body surface would allow information to be gained about the optical properties of that specific deep tissue region.

In contrast to the behavior of light in deep tissue, ultrasound experiences significantly less scatter and can be focused to known locations of just a few cubic

millimeters [18]. The work described here looks to use low intensity ultrasound to generate light in a specific tissue region by taking advantage of the physical interaction between ultrasound and microbubbles of gas.

Microbubbles of perfluorocarbon gas have been used for many years as contrast agents to allow ultrasound to visualize the vasculature [55, 56]. The difference in compressibility between the gas of the microbubble and the surrounding water allows the microbubble to radially oscillate in size when exposed to the compression and rarefaction portions of an ultrasound pulse [19, 21, 22, 57]. This compressibility difference enables populations of microbubbles to be highly reflective to ultrasound [55, 58]. A common stable formulation for the gas used in contrast agent microbubbles consists of an air/perfluorocarbon mixture [59]. The perfluorocarbon gas has low solubility in water and helps stabilize the microbubble more effectively than pure air or nitrogen [59, 60].

The small radius of curvature of the gas microbubble results in a high water surface tension that creates a net inward radial force increasing the pressure on the microbubble [61]. This higher-than-ambient pressure on the microbubble accelerates the gas dissolution into the water and can rapidly shrink the microbubble. This surface tension can be greatly reduced by coating the gas surface with a monolayer of lipids resulting in a significant lifetime increase [62, 63]. The type and ratio of lipids in these membranes can have dramatic impacts on the flexibility and fluidity of the membrane as a whole [64]. As the microbubble undergoes compression and expansion this lipid monolayer also expands and contracts [62]. Small sections of the shell have been

shown to come off during compression [65, 66] and during the expansion phase individual lipid molecules are theorized to separate from one another [67].

Recent efforts from our group have utilized the lipid separation during the expansion phase to generate an optical signal by placing a self-quenching lipophilic dye [68-70] into the lipid monolayer [24]. These dye molecules are separated during the expansion phase resulting in a greater number of emitted fluorescent photons than in the compression phase where the dye molecules come close together increasing their ability to self-quench. This creates an intensity modulated (or “blinking”) fluorescence signal which is modulated at the frequency of the applied ultrasound energy as illustrated in Figure 1.1. A contrast agent which creates fluorescence modulations using a microbubble loaded with a dye-quencher pair has been theoretically modeled [71].

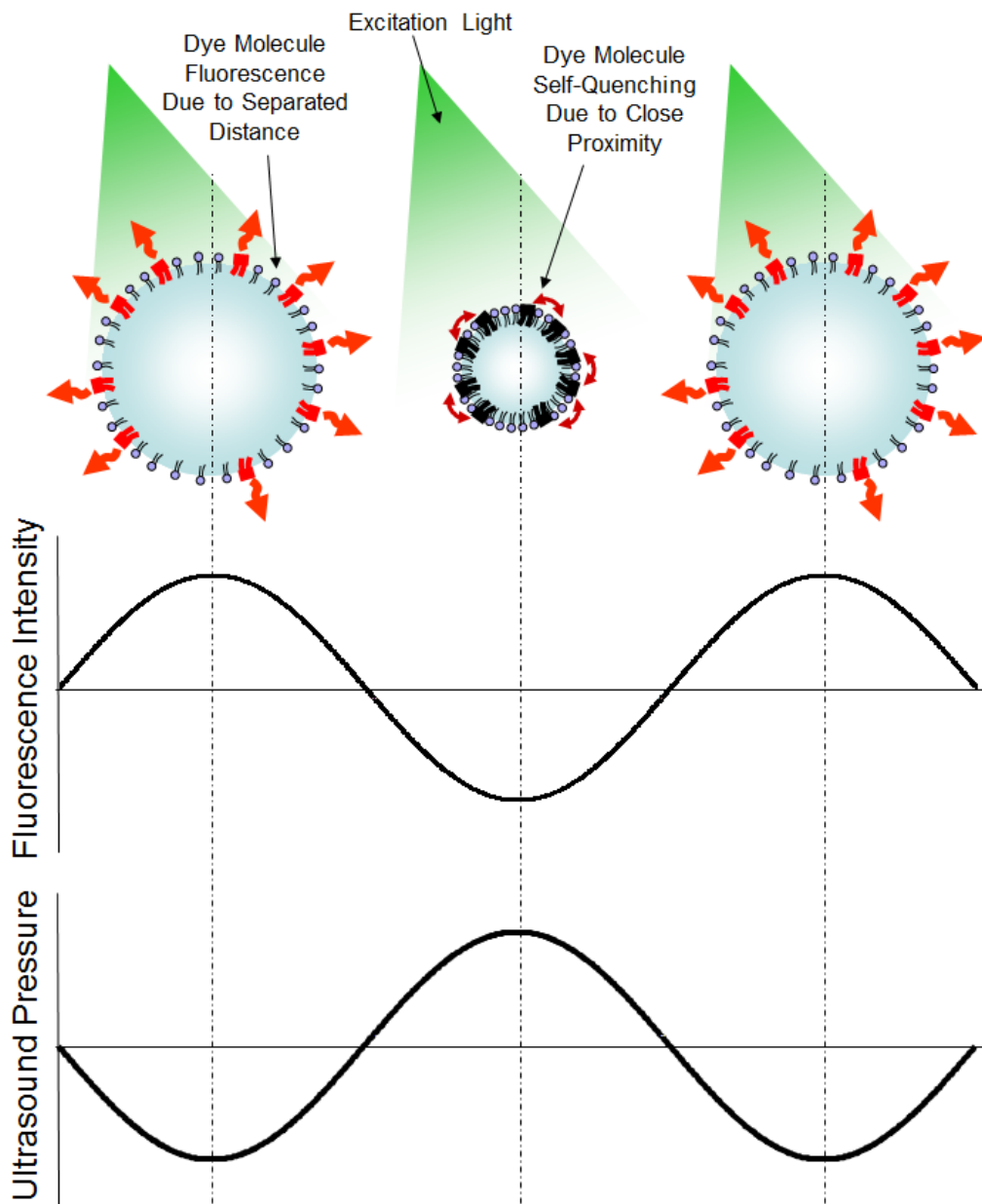


Figure 1.1 Schematic of fluorescence intensity modulation (“blinking”) mechanism. Microbubbles undergo size oscillations in response to the ultrasound pressure wave. At low ultrasound pressure, the bubble expands, separating the dye molecules and preventing them from quenching. At high ultrasound pressure, the bubble is compressed, and the dye molecules are quenched due to close proximity. This results in a fluorescence intensity modulation signal at the same frequency as the applied ultrasound wave.

Blinking will only occur in the focal zone of the ultrasound allowing the spatial location of this modulated signal to be identified from within deep tissue. The excitation light that is applied at the body surface can be filtered out at the detectors to allow collection of just the fluorescent photons. Lock-in amplification electronics can be used to remove the non-blinking fluorescent background generated from microbubbles not in the ultrasound focal zone by locking on to the blinking frequency and measuring only the blinking signal. The frequency of blinking will match that of the driving ultrasound. This approach can be used to overcome the spatial resolution limitations of optical imaging in deep tissue due to strong optical scattering. Use of this hybrid technique has many valuable clinical applications including the detection of tumor-associated biochemical information from suspected lesions to improve cancer diagnosis accuracy.

An imaging system utilizing this ultrasound-modulated fluorescent microbubble probe would enable the extraction of optical biochemical information with millimeter-scale resolution in highly scattering environments. Specialized detection systems have been developed to successfully monitor this blinking effect *in-vitro* and were used in this study [24, 72]. These systems use a high time resolution photomultiplier tube (PMT) to count the number of photons that are produced by individual microbubbles as they flow through the co-localized focal zone of an excitation laser and ultrasound transducer. By placing wavelength interference filters in front of the PMT, the fluorescent photons pass through while the scattered excitation photons are blocked. By removing the filter the system can also be used to monitor the photons that are side-scattered at 90° from the excitation laser, resulting

from microbubble interaction with the excitation laser. The number of scattered photons increases with the expansion of the microbubble and decreases with the bubble's contraction in a nonlinear size-dependence described by Mie scattering [73, 74]. This results in the production of scattered-light modulation signals occurring at the applied ultrasound frequency. Previously, such scattered excitation light modulations have been consistently observed for all samples containing dye-loaded microbubbles, however only a distinct subpopulation was observed to produce fluorescence modulations. It was hypothesized that the nanoscale lipid partitioning on the surface of the microbubble might be affecting the microbubble blinking ability. The work described here looks to study the effect of lipid partitioning on the microbubbles' ability to blink.

Typical manufacturing processes for lipid-coated microbubbles involve the use of a probe sonicator or rapid shaker which simultaneously pushes the air/perfluorocarbon gas mixture into the water phase to create bubbles while breaking up lipid micelles in the water and allowing them to recondense onto the gas/water interface of the microbubble [75]. The probe sonicator has the additional effect of raising the temperature of the fabrication solution which then slowly cools to room temperature after the sonicator power is removed. The different lipids and lipophilic dyes used to create the monolayer have been shown to naturally aggregate into islands of various configurations when allowed to slowly cool to room temperature [62, 76]. There is considerable interest in determining how these variations in lipid partitioning affect the dynamics of the surface as the lipid surface accommodates the expanding and contracting size changes of the microbubble in response to ultrasound. Kwan and

Borden have studied the lipid shell mechanics during bubble growth and dissolution due to gas exchange which occurs on a much slower time scale than the individual ultrasound-induced expansion and contraction events [67]. By monitoring the intensity of the fluorescence-modulated signal produced by self-quenching dye-loaded microbubbles, the real-time expansion and contraction of these lipid structures can be monitored. Understanding which lipid species and structures are involved in allowing microbubble expansion is important information for applications that involve manipulating the surface properties of the microbubble through crosslinking or other methods to control the ultrasound reflectivity properties. In this work different lipid surface structures were created by applying various temperature treatment regimens to the fluorophore surface-loaded microbubbles. The nanoscale surface structure of these bubbles was investigated using 3D structured illumination super-resolution microscopy (3D-SIM). The acousto-fluorescence detection system described above was used to understand how the observed structures expanded and contracted in response to the applied ultrasound through analysis of the acquired fluorescence and scattered-light signals.

Methods and Materials

Materials

Distearoyl phosphatidylcholine (DSPC) was purchased from Avanti Polar Lipids, Inc. (Alabaster, AL) and distearoyl phosphatidylethanolamine-methyl poly(ethylene glycol) MW5000 (mPEG-DSPE 5k) was purchased from Laysan Bio,

Inc. (Arab, AL). Dulbecco's phosphate buffered saline (DPBS) was purchased from Hyclone Laboratories Inc. (Logan, UT). DiO was purchased from Biotium, Inc. CA. Perfluorohexane (PFH) was purchased from Sigma-Aldrich (St. Louis, MO).

Microbubble Manufacturing

50 μ l of 20 mg/ml DSPC in chloroform, 20 μ l of 50 mg/ml mPEG-DSPE 5k in chloroform, and 30 μ l of 1mM DiI in chloroform were added successively to a 4 ml glass vial under vortex to ensure proper mixing. DiI was added at a ratio of 2 mol %, which was previously shown to be an effective fluorophore loading concentration to achieve fluorescence modulation at diagnostic ultrasound pressures [24]. The chloroform was evaporated under an argon or nitrogen stream while mixing on the vortexer to make a thin film of lipid along the inner surface of the vial. 500 μ l of PBS was added to the vial and the lipids were resuspended by vortexing for 15sec with subsequent heating at 75°C for 1 min. This cycle of vortexing and heating was repeated until the lipids were well suspended and no residue was left on the vial walls. The sample was allowed to cool to room temperature.

The vial top was covered with parafilm to create a gas barrier to the external atmosphere. 1 ml of PFH was drawn into a 5ml syringe with a 22 gauge needle. The syringe was agitated and allowed to sit for at least 3min to allow the air inside the syringe to saturate with the PFH. The needle of the syringe was bent at 130° into a hook configuration and poked through the parafilm into the vial headspace. The syringe was then pumped 65 times into the vial head space while being careful to prevent any liquid PFH from entering the vial. This saturated the air in the vial

headspace with a PFH/air mixture. The tip of the XL-2000 probe sonicator (QSonica LLC., Newtown, CT) was immediately inserted through the parafilm and positioned 1mm below the gas/water interface. The probe sonicator was then turned on at 25 W for 3 seconds. The resulting microbubbles were allowed to sit for at least 5 minutes before further processing.

Excess lipid and dye in the sonicated solution was washed from the microbubbles. The microbubbles were transferred to a microcentrifuge tube and centrifuged at 1000 rpm for 3 min to float the bubbles. The supernatant was partially removed and replaced with PBS. This process was repeated 1-2 additional times.

Microbubbles were imaged using conventional brightfield and fluorescence microscopy using a Nikon upright microscope fitted with a high numerical aperture objective (Nikon 60x oil immersion NA = 1.4).

Microbubble Temperature Treatment

The washed microbubble samples were temperature treated according to the following five temperature regimens which were adapted from Borden et al. [76]. Heating was performed at 75°C which is above the 56°C lipid transition temperature of the DSPC shell component.

1. “Rapid-cooling”: 3 minutes of heating at 75°C, followed by 5 minutes of cooling at 0°C. Rapid is used in reference to the rate of degrees/minute at which the lipids pass through the transition temperature.
2. “Slow-cooling”: 3 minutes of heating at 75°C, followed by 5 minutes of cooling at 45°C.

3. “Rapid-cooling, short intervals”: 1 minute of heating at 75°C, followed by 1 minute of cooling at 0°C.
4. “Slow-cooling, short intervals”: 1 minute of heating at 75°C, followed by 1 minute of cooling at 45°C.
5. “No treatment”: washed microbubbles were kept at room temperature.

To achieve these temperature regimens the microbubbles were drawn into an 18 inch long 20 gauge metal needle and the end of the needle was then blocked by insertion into a rubber stopper. The needle was fully immersed into water baths at the indicated temperatures and durations described above, with an immediate full-immersion transition between the different temperature baths. The treated microbubbles were then transferred into microcentrifuge tubes.

3D Structured Illumination Super-Resolution Microscopy (3D-SIM)

Microbubble nanostructures were visualized using a 3D structured illumination super-resolution microscopy (3D-SIM) technique on the OMX system (Applied Precision Inc., Issaquah, WA) with a 100x oil immersion objective. Microbubbles were immobilized in glycerol immediately prior to imaging to avoid motion artifacts during image acquisition.

Acousto-Fluorescence Detection System and Signal Acquisition

Fluorescence and scattered-light modulation signals were acquired from insonated microbubbles using a previously described in-house designed acousto-

fluorescence detection system [24, 72]. Briefly, a 532 nm laser, 2.25 MHz US transducer and collection objective were aligned mutually orthogonally and confocally with a water bath interaction zone. The 2.25 MHz ultrasound was pulsed at a 1Hz repetition rate with 15 sine wave cycles per pulse and a pressure of 1.0 MPa. The 2.25 MHz frequency is within the resonance frequency range of the 1-5 μm microbubbles. A syringe pump was used to deliver a dilute solution of microbubbles into the interaction zone to simultaneously interact with both the ultrasound pressure wave and laser excitation. To load microbubble samples into the system, bubbles were loaded into a 60 ml syringe pre-filled with water to obtain sufficiently dilute solutions to achieve approximately 1 bubble per ultrasound pulse. To detect fluorescence, the light collected from the objective was collimated and passed through a series of wavelength interference filters to filter out the scattered light, detecting only fluorescence emission. The only difference between the setup used here and setup used in Benchimol et al. [24] is that only one PMT was used to collect both fluorescence and scatter signals. Scattered light oscillations were obtained by removal of the fluorescence filters from the optical path. All the microbubbles were observed to scatter light but only a fraction of those actually displayed measurable fluorescence intensity modulation. The flow rate of microbubbles through the system was kept constant over the entire monitoring period. Signals were acquired from the PMT using a LabVIEW acquisition program which generated both time and frequency domain data. Each microbubble sample was monitored by acquiring signals during insonation in the scattered-light detection configuration for a period of about 5 minutes, yielding 300 signals. This established the number of microbubbles that were running through

the system per minute. Immediately following this acquisition the fluorescence filters were inserted into the system and fluorescence signals were acquired for an equal number of microbubbles over an equal time period.

Acousto-Fluorescence Signal Analysis Program

A custom program was developed in LabVIEW 8.1 to systematically analyze acquired signals for the presence of fluorescence and scattered-light modulations at the applied ultrasound frequency. The program determined the presence of a modulation in a collected signal by sampling the magnitude of the acquired Fourier transform at the 2.25 MHz frequency and comparing it with the background noise level of the signal, excluding very low frequency noise. A signal detection threshold level of 1.25 times the background level was determined and validated by testing on control microbubbles prepared with no fluorescent dye which did not generate ultrasound-modulated fluorescence signals. At this detection threshold level, no false positive signals were generated by the analysis program and this threshold was used to evaluate all microbubble treatments for incidence of modulation signals. By applying this threshold, the number of microbubbles that scattered the excitation laser light was counted for a set of 300 acquired scatter-configuration signals. The same threshold was then applied to count fluorescence modulations for the corresponding set of 300 acquired fluorescence-mode signals. Triplicate batches of microbubbles were prepared using the four above-described temperature regimens as well as no treatment. The three batches of all five treatments were prepared and analyzed on separate days.

Signals acquired from all three days were combined for each temperature treatment regimen and the number of fluorescence modulating microbubbles was divided by the number of scattering microbubbles to compute a percentage of fluorescence-modulating microbubbles for each treatment. The proportions of fluorescence-modulating microbubbles were analyzed for statistically significant differences using a chi-square test. A post hoc comparison was then conducted between groups using the Bonferonni adjustment. The percentage of fluorescence-modulating microbubbles was also calculated for each treatment for each of the three days (batches). The mean fluorescence-modulation percentage of the three batches and standard deviation was calculated for each treatment to show batch-to-batch variability.

Results

Microbubble Manufacturing and Temperature Treatment

Microbubbles surface-loaded with fluorescent DiI in the lipid monolayer were prepared by the manufacturing process described above and are shown prior to temperature treatment in Figure 1.2a and b. The bulk solution of microbubbles with no temperature treatment is shown prior to washing in Figure 1.2c. Using conventional fluorescence microscopy with a high numerical aperture, all prepared bubbles were seen to have surface-loaded fluorescence, but no microstructural features or presence of discrete domains could be seen on the bubble surface with this microscopy technique. No visible difference in fluorophore surface patterning could be seen

between bubbles that were not temperature treated and bubbles that were subjected to various times and regimens of thermal treatment. Microbubbles were found to be stable through the temperature treatment processes, persisting for several days; however the microbubble yields were lower after thermal treatment likely due to rupture of the least stable bubbles.

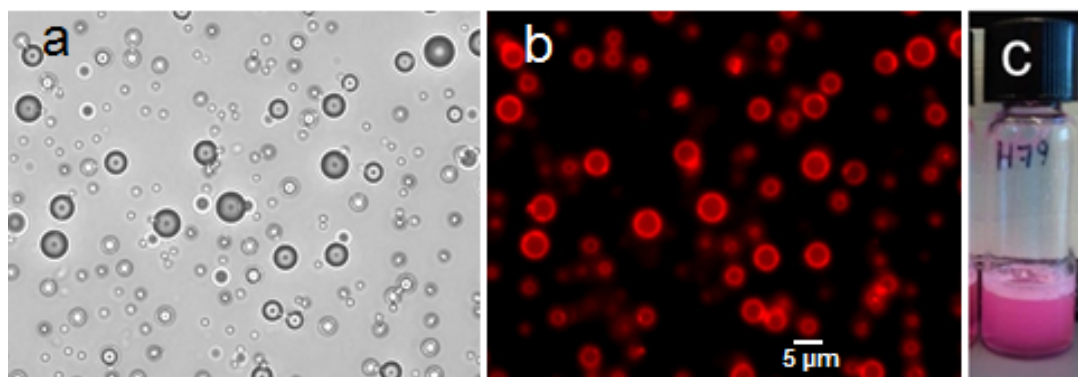


Figure 1.2 Conventional imaging of DiI surface-loaded microbubbles. (a) Brightfield illumination. Each microbubble appears as a circle with white and dark regions created due to interference resulting from a lensing effect caused by the index of refraction mismatch between the water and the gas. (b) Fluorescent image of the same field of microbubbles. Fluorescence from the center of individual microbubbles indicates presence of surface-loaded fluorophore. (c) Image of the bulk microbubble solution prior to washing showing the microbubbles as a turbid pink suspension.

3D Structured Illumination Super-Resolution Microscopy

Surface patterning of the lipids and fluorophore was not visible in the conventional fluorescence images shown in Figure 1.2b. This imaging system did not have the capability to resolve features below the diffraction limit and fluorescence

from all sections of the microbubble appeared as a summed 2D projection creating what appears to be a uniform hazy distribution of fluorescence across each microbubble. The use of 3D structured illumination super-resolution microscopy (3D-SIM) allowed visualization of microbubble surface features below the diffraction limit. The axial sectioning capability of this technique allowed removal of the confounding fluorescence from out-of-focus layers to reveal the nanoscale surface structure and island partitioning of the fluorophore. Top surface and cross-section images of microbubbles exposed to various temperature treatments are seen in Figure 1.3. Under no temperature treatment, the fluorophore was seen to have partitioned into isolated island structures creating a speckled appearance, with most of the structures less than 500 nm in size. These structures were seen on the surface of the microbubble as well as its cross-section indicating that these structures were prevalent over the entire microbubble surface. With microbubbles that were surface-melted followed by “rapid-cooling” through the lipid transition temperature, these island structures were seen to have disappeared and were replaced with a uniform fluorescence over the surface and cross-section of the microbubble. When the microbubbles were allowed to “slowly cool” through the transition temperature, the images displayed that the fluorophore was again partitioning into concentrated islands although to a lesser degree than the bubbles with no thermal treatment.

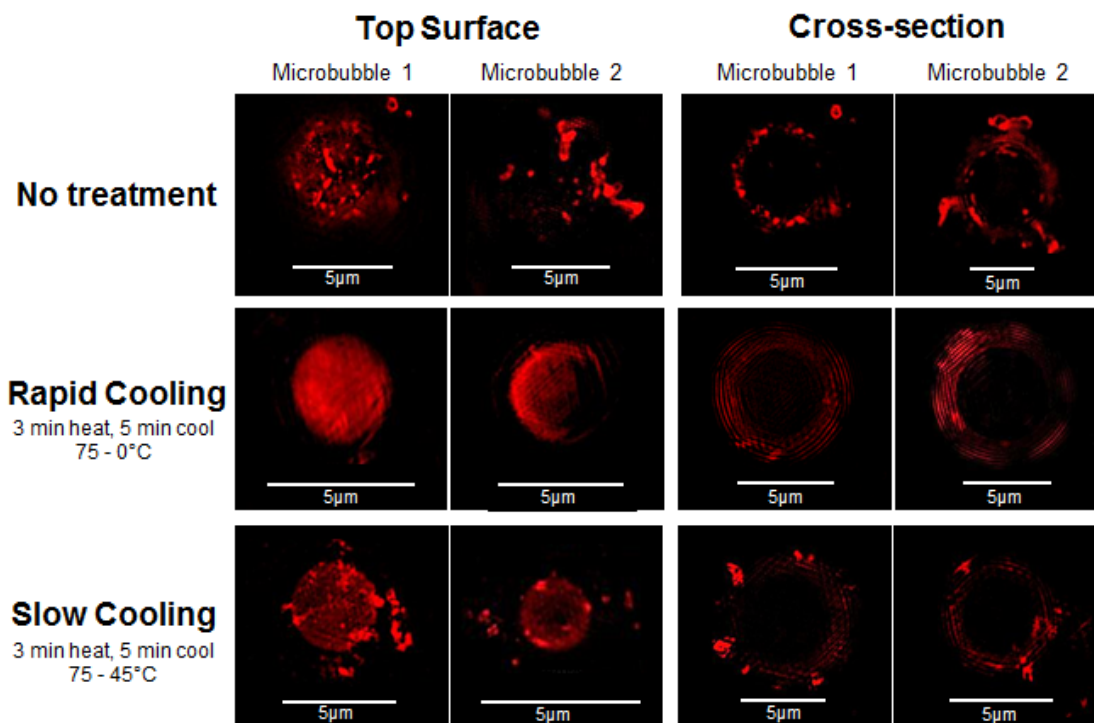


Figure 1.3 Super-resolution microscopy images of surface-loaded fluorescent microbubbles prepared with various temperature treatment regimens. Microbubbles that did not undergo temperature treatment displayed highly concentrated islands of fluorescence seen on both the top surface and in cross-sections. For microbubbles that were heated to 75°C for 3 minutes to melt the lipid monolayer followed by cooling at 0°C for 5 minutes (“rapid-cooling”), the fluorophore was seen to uniformly coat the surface of the microbubble. This fluorophore distribution suggests that the concentrated fluorophore in the islands was melted to a more homogenous distribution during the heating phase and then when rapidly cooled this even distribution was solidified into place. When the microbubbles were heated to 75°C for 3 minutes followed by cooling at 45°C for 5 minutes (“slow-cooling”), island structures were able to re-form before the fluid motion of the lipids was restricted. The crosshatch patterns seen in some of the cross-sectional images are image reconstruction artifacts from the 3D-SIM technique.

Acousto-Fluorescence Detection System Signals

Time domain signals and frequency spectra of typical acquired scattered light and fluorescence signals are shown in Figure 1.4 for microbubbles of different thermal treatment regimens. Signals acquired from detected laser side-scatter resulting from microbubble interaction with the excitation laser are shown in Figure 1.4a with the corresponding spectra shown in Figure 1.4b. Both rapid-cooled and non-temperature-treated bubbles display a peak at the 2.25 MHz ultrasound driving frequency, indicating that both types of bubbles undergo size modulation in response to the applied ultrasound pressure. However, when the fluorescence filters are applied to look at signals resulting from ultrasound-modulated self-quenching of the surface-loaded fluorophore, there is a lack of detectable modulating signal for bubbles that did not undergo thermal treatment as shown in Figure 1.4c. The 2.25 MHz peak resulting from fluorescence intensity modulation is clearly visible for the rapid-cooled microbubble shown in Figure 1.4d.

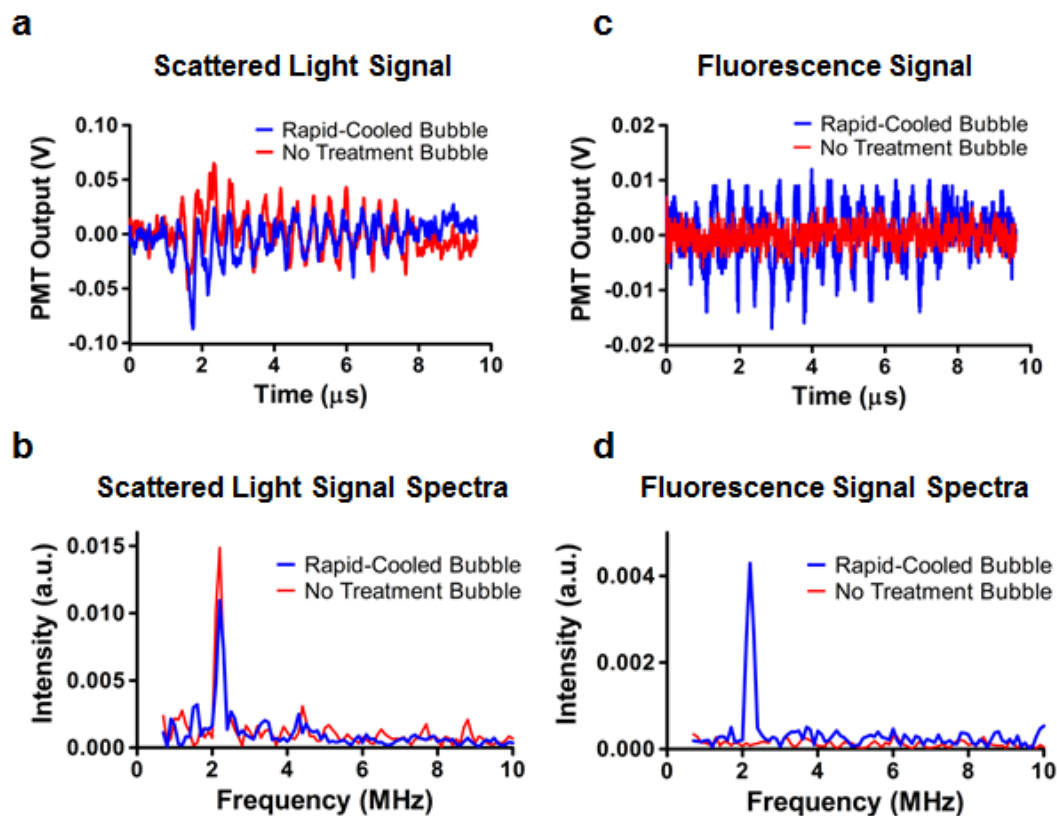


Figure 1.4 Example time and frequency domain signals acquired from rapid-cooled microbubbles and bubbles that were not temperature-treated. (a) Time domain signals acquired from side-scatter of the excitation laser resulting from microbubble size oscillations. Both rapid-cooled and non-treated bubbles display characteristic oscillations. (b) Frequency spectra of the acquired scattered light signals shown in panel a. Both rapid-cooled and non-treated bubbles display strong peaks at the 2.25 MHz ultrasound driving frequency. (c) Acquired time domain fluorescence signals. Rapid-cooled bubbles show a characteristic fluorescence oscillation that is not seen in a typical untreated bubble. (d) Frequency spectra of the acquired fluorescence signals shown in panel c. The rapid-cooled microbubble displays a clear peak at the driving frequency resulting from ultrasound-driven cyclic quenching of the surface dye. A typical untreated microbubble does not show any clear peak in the frequency spectra.

Ultrasound-Modulated Fluorescence Signal Analysis

The percentage of microbubbles that displayed a detectable fluorescence intensity modulation as defined by the signal analysis threshold is shown for the different temperature treatment groups in Figure 1.5. Less than 5% of the microbubbles that did not undergo temperature treatment displayed a detectable fluorescence modulation signal. Microbubbles that were rapid-cooled (heating at 75°C for 3 minutes with subsequent cooling for 5 minutes at 0°C) showed a ten-fold increase in the generation of this signal, with over 50% producing fluorescence modulations. A chi-square test conducted at the 0.05 significance level showed that the percentage of bubbles that displayed fluorescence-modulation was not independent of the different temperature treatments. A post hoc comparison between groups using the Bonferroni adjustment found that the fluorescence modulation percentage of the rapid-cooled microbubble group was significantly different from all other thermal treatment groups ($p < 0.05$). The symbols in Figure 1.5 denote significant differences between groups ($p < 0.05$). Approximately 19% of the microbubbles that were slow-cooled through the transition temperature (heating at 75°C for 3 minutes followed by cooling for 5 minutes at 45°C) displayed a detectable fluorescence modulation signal. Microbubbles that were heated and rapidly-cooled for 1 minute time intervals (1 minute 75°C, 1 minute 0°C) displayed fluorescence modulation incidence of approximately 19% and microbubbles that were heated and slow-cooled for the same time intervals (1 minute 75°C, 1 minute 45°C) displayed fluorescence modulation incidence of approximately 7%. There was no significant difference between the microbubbles that were heated and slow-cooled for 1 minute intervals and those

bubbles that received no treatment. These two groups had significantly lower fluorescence modulation incidence than the other treatment groups. A data summary for Figure 1.5 of the total bubble counts that displayed modulation and no modulation for each temperature treatment is given in Table 1.1. Batch-to-batch variability is shown in Figure 1.6 where the mean fluorescence modulation percentage of the three batches and standard deviation was calculated for each treatment.

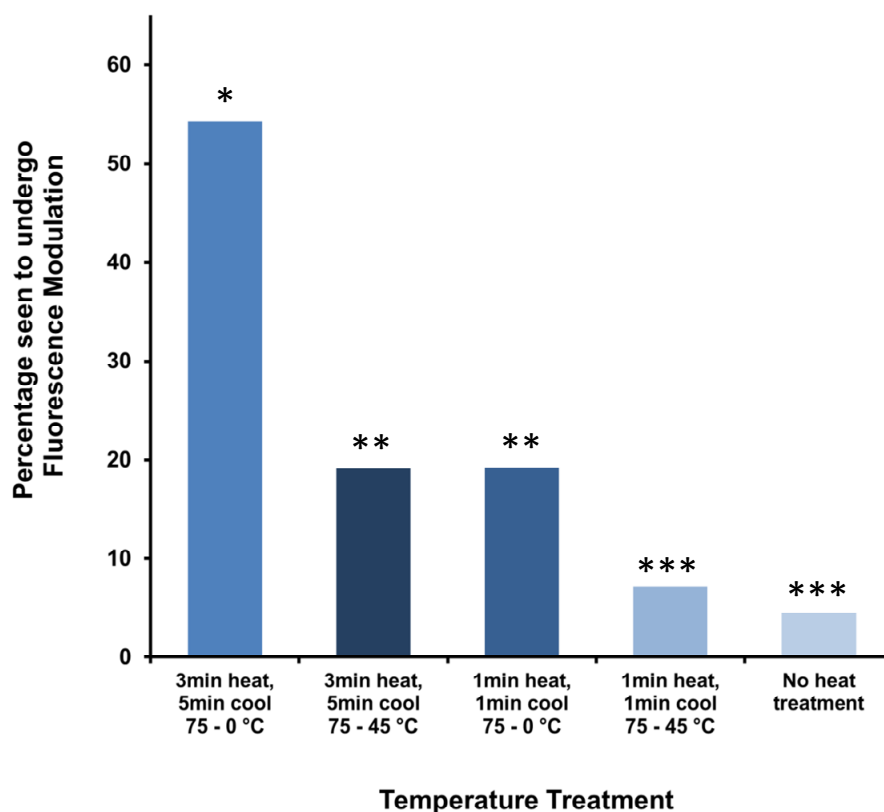


Figure 1.5 The percentage of microbubbles that displayed detectable fluorescence modulation under different temperature treatment regimens. Fluorescence modulation percentages from the combined signals acquired from all three microbubble batches, each of which included all five temperature treatments (combined bubble count data shown in Table 1.1). A ten-fold increase in fluorescence modulation incidence was seen in rapidly-cooled microbubbles (3 minutes 75°C, 5 minutes 0°C) as compared to bubbles that were left untreated. Other treatment regimens including slow-cooling (3 minutes 75°C, 5 minutes 45°C) as well as shorter time intervals of heating and cooling (1 minute 75°C, 1 minute 0°C and 1 minute 75°C, 1 minute 45°C) were less effective than rapid cooling at generating fluorescence modulations. The symbols indicate significant differences using a chi-square test with post hoc comparisons between groups using the Bonferroni adjustment ($p > 0.05$).

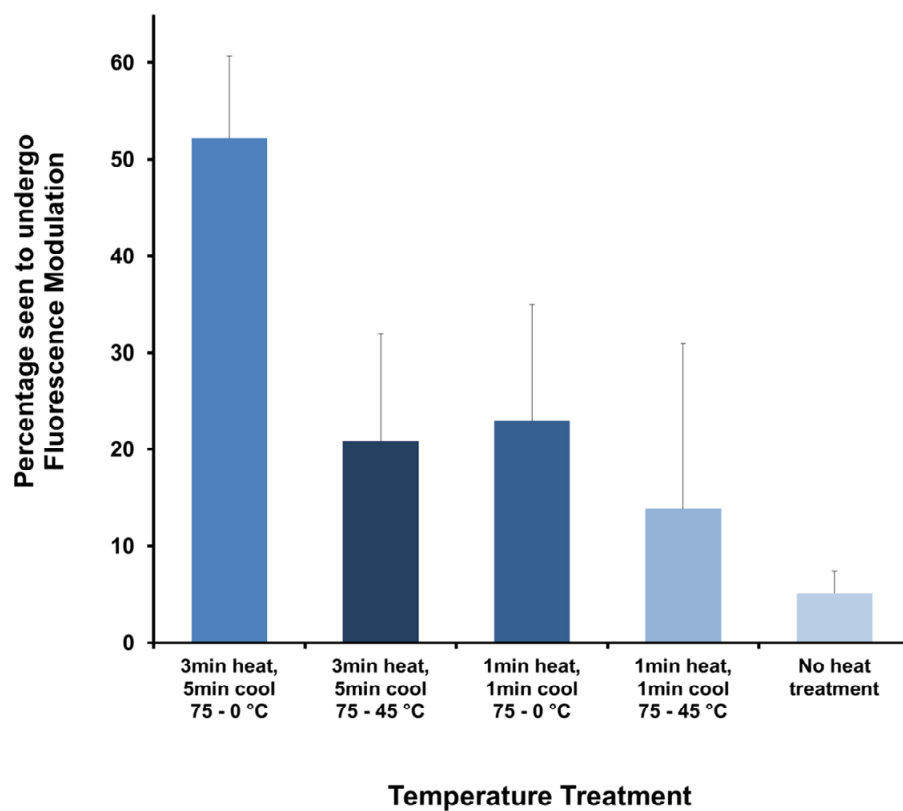


Figure 1.6 Batch-to-batch variability of the fluorescence modulation percentage for each temperature treatment regimen. Data shown as the mean fluorescence modulation percentage and standard deviation of three batches of microbubbles prepared and analyzed on separate days. Microbubbles slow-cooled for 1 minute time intervals (1 minute 75°C, 1 minute 45°C) showed the highest batch-to-batch variation.

Table 1.1 Data summary for Figure 1.5 showing the bubble count that exhibited fluorescence modulation and no modulation for various temperature treatments.

		Treatment					Total
		No Treatment	3 min heat, 5 min cool 75 - 0 °C	3 min heat, 5 min cool 75 - 45 °C	1 min heat, 1 min cool 75 - 0 °C	1 min heat, 1 min cool 75 - 45 °C	
Response	No Modulation	600	161	351	348	455	1915
	Modulation	28	191	83	83	35	420
Total		628	352	434	431	490	2335

Discussion

Microbubbles fabricated using the described probe sonication process displayed a lipid surface layer where the majority of the lipophilic dye was concentrated in islands and in large structures that extended beyond the spherical surface. These islands were either formed as a result of incomplete breaking of the micelles by the sonication probe or by recondensation of the lipid and fluorophore species into these structures as the sonicated samples slowly cooled to room temperature. The dye and associated lipids were observed to partition into different structures at different temperatures due to the fluidity of the monolayer. The transition temperatures of the species forming the shell are 55°C for DSPC and 74°C for DSPE. When heated to 75°C both lipid types showed increased fluidity and the islands of

concentrated lipid dissociated and distributed evenly throughout the monolayer. At room temperature (25°C) the monolayer's fluidity was greatly reduced and the lipids were solidified in place.

The different cooling rates from the 75°C melting temperature resulted in distinct final surface structures. When cooled rapidly from 75°C to 0°C the lipids and dye did not have the opportunity to recondense into islands and were “frozen in place” in the distributed state. When cooled slowly, the lipid monolayer passed through a temperature region where the different lipids were allowed to recondense back into the energetically favorable tightly packed island structures forming concentrated regions of the lipid species and dye. In bubbles of similar composition, carbocyanine dyes such as DiI have been observed to preferentially partition into the pegylated lipid domain [66, 77]. The islands were still observed when the microbubbles were heated to 75°C for only 1 min and rapidly cooled supporting that the short heating time was insufficient to melt the islands and allow them to distribute.

Microbubbles subjected to all four described temperature regimens (as well as no treatment) were able to undergo oscillations when exposed to ultrasound as detected by the strong excitation laser side-scattering signals. Only 5% of the microbubbles that did not undergo any temperature treatment displayed any detectable fluorescence modulation. This indicates that the dye molecules in the islands were not able to separate from one another far enough to prevent self-quenching and that the islands of DSPE-PEG5K and dye did not expand significantly when exposed to ultrasound. Another possibility is that the dye molecules were too concentrated in the islands to undergo fluorescence modulation even if the islands did expand.

Over 50% of the microbubbles that underwent the 5 minute heating and subsequent rapid cooling treatment showed measurable fluorescence intensity modulation. This indicates that when the dye was distributed evenly across the surface of the microbubble the dye molecules were more likely to be able to move far enough from one another to change the amount of self-quenching that occurred as the microbubble expanded. Another potential contributor to the increase in signal incidence with rapid-cooling is that the observed lipids and fluorophore extending outward from the surface of the bubble could have been melted back onto the main gas sphere, providing more available fluorophore coupled to the size-oscillating microbubble. Higher fluorescence modulation percentages could potentially be achieved through an extended heating period, an even more rapid temperature quenching rate, or multiple cycles of rapid-cooling. A general trend was seen in Figure 1.5 that the more thermal manipulation the microbubbles received (longer intervals, more rapid cooling), the higher the incidence of fluorescence modulation.

Increasing the percentage of microbubbles that display detectable fluorescence intensity modulation is essential to improving the future efficacy of these microbubbles as optical imaging contrast agents. Imaging techniques using these microbubbles can allow extraction of tissue biochemical information with previously unattainable spatial precision by using the ultrasound-modulated signal to extract the signal generated from the ultrasound focal zone. The biochemical information obtained could allow for detection of tumor-associated hallmarks such as hypoxia [13, 14] and angiogenesis [78] and could lead to significant improvements in the accuracy of cancer diagnostic techniques. This detection method requires the consistent

generation of a modulating-fluorescence signal, which is enabled through the use of a rapidly-cooled thermal regimen to produce more effectively modulating bubbles.

This microbubble temperature treatment method and the resultant dynamic bubble behavior under ultrasound have implications for applications that require the lipids of the microbubble monolayer to be well distributed. For example, applications that require surface-crosslinking and manipulation of microbubble stiffness to change the acoustic properties will need to take island formation into account when designing the linking chemistry between the different lipid species. The crosslinking is more likely to be effective at constraining microbubble expansion if it is made evenly across the surface rather than just between islands. Evenly distributed crosslinking could also help increase microbubble stability when exposed to low level ultrasound to extend their effective imaging lifetime.

Evenly distributed lipid coatings are also important when covering the bubble surface with PEG or other coatings to prevent immune system recognition. When the pegylated lipids all congregate into island structures, this leaves regions where the PEG coating does not cover the surface potentially reducing the circulation half-life of the microbubble. This PEG layer also helps increase microbubble stability during storage as it helps prevent coalescence. The PEG prevents physical contact of lipid layers from neighboring microbubbles.

A uniform coating is also important when using targeting ligands on the microbubbles to cause preferential accumulation in specific tissues. Targeting ligands are most frequently coupled to the surface of microbubbles and liposomes by attachment at the ends of the same lengthy PEG chains used to avoid immune

recognition. As an illustrative example, the use of cRGD peptide as a targeting ligand for the neovasculature marker $\alpha v\beta 3$ integrin [78, 79] could be made more efficient by controlling the distribution of the associated PEG. Targeting efficiency would be enhanced when the cRGD covers the entire surface of the microbubble evenly rather than being concentrated into islands which may or may not come into contact with cells as the bubble passes through the vasculature.

Conclusion

Lipid-coated microbubbles containing self-quenching lipophilic dye molecules were manufactured by a probe sonication method resulting in surface nanostructures that displayed islands of high dye concentration. The dye molecules in these islands were not able to separate sufficiently from one another during the expansion phase of microbubble interaction with ultrasound to modulate their self-quenching properties. Temperature treating these microbubbles to melt the lipid islands allowed the dye to evenly distribute about the surface of the microbubble. Subsequent rapid cooling was applied to solidify the lipids in place preserving this distributed state. The even distribution allowed the dye molecules to separate sufficiently from one another to change their self-quenching efficiency resulting in a ten-fold increase of detectable fluorescence intensity modulations. This supports that the lipid islands were not able to expand sufficiently with the rest of the lipid monolayer. The enhanced efficiency of these contrast agents to generate ultrasound-induced fluorescence modulations enables the development of imaging techniques which make use of their precisely-controlled

fluorescence signal and promise to improve optical detection of clinically relevant biochemical information in deep tissue.

Acknowledgements

Support was provided by Grant Numbers T32 CA121938 and R25 CA153915 from the National Cancer Institute and NIH P30 grant NS047101. The content is solely the responsibility of the authors and does not necessarily represent the official views of the National Cancer Institute or the National Institutes of Health.

Chapter 1, in part, has been submitted for publication of the material as it may appear in Small, 2014, Carolyn Schutt, Stuart Ibsen, Michael Benchimol, Mark Hsu, Sadik Esener, Wiley-VCH 2014. The dissertation author was the primary investigator and author of this paper.

Chapter 2

Increasing the Signal to Noise Ratio for the Detection of Modulated
Fluorescence Generated by Ultrasound-Driven Dye-Loaded Microbubbles
in Scattering Media

Abstract

As described in Chapter 1, a new dye-loaded microbubble optical contrast agent has been developed that can modulate the intensity of fluorescence light production when exposed to ultrasound. This essentially creates a microbubble that can “blink” inside the focal zone of the ultrasound. The fluorescence light modulation has been detected in a non-scattering media at the fundamental driving frequency of the ultrasound as expected. However, microbubbles are known to oscillate at higher harmonic frequencies in addition to the fundamental frequency. Detecting these harmonic signals could produce a higher signal to noise ratio for fluorescence imaging applications by allowing reflections or artifacts of the fundamental ultrasound driving frequency to be filtered out. Here we demonstrate for the first time that the rapid-cooling thermal treatment technique described in Chapter 1 can reproducibly create microbubbles that are capable of generating 2nd, 3rd, and even 4th harmonic intensity modulations. Although the detection of harmonics is possible in a non-scattering media, it has not yet been demonstrated that a dye-loaded microbubble can produce any modulated fluorescence intensity signal that can be detected from within a scattering media. Whereas the fluorescence modulation signals are relatively straightforward to detect by using a spectral analysis on a collected signal when the microbubbles are in a non-scattering media, in a scattering environment the modulated signal must now contend with a higher level of background photons scattered towards the detector. We demonstrate for the first time the detection of the fundamental frequency in the modulated fluorescence signal produced by the blinking microbubble

and compare that to the modulated scattering signal produced by the microbubbles from within media that have increasing scattering coefficients. It was determined that the fluorescence modulation generated by these rapid-cooled microbubbles created a larger signal to noise ratio at the fundamental driving frequency than the modulated photon scattering signal produced by the microbubbles.

Introduction

The main challenge of using photons in the visible light spectrum for biological imaging is the high degree of photon scattering that occurs in the tissue [80]. Most optical information about deep tissue comes from the degree of absorption or differential absorption of photons at certain wavelengths of light [16]. However, the scattering that occurs in tissue prevents most photons from having a straight line migration through the tissue [81]. Existing schemes use photons that are produced external to the body and are introduced to the tissue from the body surface to flood the general tissue region including the region of interest [82]. When using non-invasive methods to detect and analyze these photons at the body surface it is very difficult to distinguish which photons have passed through the deep tissue (> 1 mm) region of interest and which photons have been multiply scattered through other tissue regions and then up to the detector.

An analogous problem exists when using fluorescent probes that pass through the circulation. The tissue scattering makes it difficult to deliver excitation photons to a spatially selective tissue region of interest, such as a suspected lesion, and instead

the excitation light floods the entire general tissue area. This creates a large background of fluorescent photons from the entire area which can overwhelm the photons emitted from the region of interest. This background level of fluorescent photons can be reduced by targeting the dyes to surface proteins expressed by the tissue type of interest, allowing them to accumulate while the unbound dye molecules are washed out from the surrounding tissue. However, it is not always clear which proteins can be used for targeting, especially when dealing with suspected tumor lesions. Inadvertent adhesion or non-specific binding of the dye to other tissue structures in the general area reached by the excitation light can confound the interpretation of the collected fluorescent light as it pertains to the tissue region of interest.

To address both the tissue scattering and the dye localization issues, the tissue region of interest can be modified to change its optical properties. Ultrasound energy can be tightly focused in tissue [18] and thus can be used to highlight a certain region of choice to differentiate it from the surrounding tissue by changing its refractive index and the distance between scatterers. These changing tissue properties modulate the number of photons that get scattered to the surface to reach the detector. This modulated intensity of photons differentiates those that pass through the tissue region of interest from the photons that pass only through the surrounding tissue. Hybrid imaging techniques such as acousto-optic imaging employ this modulated photon intensity and benefit from improved spatial resolution of the detected optical information [83-86]. However, the small quantity of modulated photons generated compared to all the unmodulated photons makes low signal to noise a significant

challenge and key area of focus for transition of these techniques to clinical application [71, 87]. Microbubble-based contrast agents interact with focused ultrasound creating significant oscillations in their diameter which change their photon scattering properties [19, 21, 22, 57]. In non-scattering media the change in the scattering properties of the microbubbles can be monitored as a modulated intensity of scattered photons viewed from an angle perpendicular to the incident light [72, 73, 88]. These microbubbles could be injected in-vivo and allowed to circulate to the tissue region of interest that is simultaneously being exposed to an incident light and focused ultrasound, both of which are generated external to the body. Monitoring for an oscillation in the intensity of the returned photons that are scattered back to the body surface indicates that those photons passed through the tissue region of interest highlighted by the ultrasound and their intensity relative to other nearby tissue regions can yield absorption information which can be useful for disease state diagnosis. However, using a photon intensity modulation method that is based on scattering properties of the microbubbles may produce a low signal to noise ratio due to the high scattering coefficient that is inherent in tissue.

To address this challenge a new manufacturing method has been developed as described in Chapter 1 to produce microbubble-based imaging contrast agents that modulate the production of fluorescent photons in a method that is entirely independent of scattering. The dye loaded microbubbles interact with focused ultrasound, expanding and contracting in diameter which increases and decreases the distance between individual fluorescent dye molecules. This effectively modulates the self-quenching efficiency of the dyes resulting in an intensity modulation of the

fluorescent light production. The incorporation of fluorophores in these contrast agents also takes advantage of the high sensitivity of fluorescence imaging and allows for the use of dyes that are environmentally sensitive in wavelength or intensity [89-91]. The fluorescence generated can be used to provide information about tissue chemical state, such as oxygenation and pH which can be markers for disease [12-14, 92]. In this imaging scheme, since the excitation light floods the general tissue region fluorescent photons will be produced all over this area. The photons produced in the ultrasound focal zone have the same wavelength as the fluorescent photons created in the surrounding tissue, but the intensity of the fluorescent light is modulated over time at the same 2.25 MHz frequency as the driving ultrasound. Thus from within a nearly constant background of fluorescent photon production there is a small increase and decrease in the number of produced photons within the focal zone at 2.25 MHz. This small signal is relatively straightforward to detect by using a spectral analysis on a collected signal when the microbubbles are in a non-scattering media as described in Chapter 1. A rapid-cooling thermal treatment procedure significantly increased the incidence of this microbubble-generated modulated fluorescence signal as described in the previous chapter.

By passive hydrophone monitoring of microbubbles exposed to ultrasound as well as light-scattering techniques it has been shown that microbubbles oscillate in diameter at the fundamental driving frequency of the ultrasound and also at higher harmonics [72, 93]. This production of harmonic signals resulting from asymmetric oscillations of the microbubbles in response to ultrasound has been observed with ultrasound-modulated photon scattering of microbubbles [72] but not yet with

modulated fluorescence. In Chapter 1, the surface morphology of the lipid and dye on the contrast agent microbubbles was manipulated using several thermal treatment techniques. The techniques are now employed to characterize their effect on the generation of fluorescence modulation harmonic signals. The first study in this chapter looks at the potential of using the non-linear properties of the microbubbles' interaction with ultrasound to produce detectable 2nd, 3rd and 4th harmonic fluorescence intensity-modulated signals that may enable a higher signal to noise ratio than the fundamental 2.25 MHz driving ultrasound frequency. The harmonic signals at 4.5, 6.75, and 9 MHz will be lower in intensity than the fundamental driving frequency, but because they are only produced by the microbubbles these frequencies would have virtually no background noise to contend with, producing an excellent signal to noise ratio. Microbubble-specific harmonic signals are used in this manner in ultrasonography to improve signal to noise [93, 94]. Detection of the higher harmonics would also reduce the potential for interference from other acousto-optic effects. The modulated-fluorescence harmonic signals described in this work could also be exploited to avoid any possible electrical noise from the ultrasound signal generator or other possible effects from the 2.25 MHz ultrasound frequency interacting with tissues in the body.

While the detection of harmonic fluorescence modulations may be possible in a non-scattering media, it has not yet been demonstrated that a dye-loaded microbubble can produce any modulated fluorescence intensity signal that can be detected from within a scattering media. In a scattering environment such as biological tissue, the modulated signal must contend with a higher level of background photons

scattered toward the detector. To address this challenge, the second study of this chapter takes the approach of using a lock-in amplifier [95] to detect the 2.25 MHz fundamental frequency oscillation in the raw PMT signal instead of traditional spectral analysis. This method was chosen due to the higher signal to noise ratio (SNR) produced by the lock-in amplifier's correlation analysis. The signal to noise ratio was measured from the lock-in amplifier while detecting the modulated fluorescence signal produced by the dye-loaded microbubble contrast agents. This was compared to the signal to noise ratio measured while detecting the modulated scattering signal generated by these bubbles. The lock-in amplifier uses the driving signal of the ultrasound transducer as a reference signal when analyzing the collected signal from the photo-multiplier tube (PMT) detector monitoring microbubble fluorescence oscillations. The lock-in amplifier was used to isolate and amplify the component of the PMT signal at the supplied reference frequency. The resulting signal generated by the lock-in amplifier was used to detect the modulated signal in increasingly scattering environments. Lock in amplifiers have been used before for acousto-optic detection in a scattering media [96, 97] but not with fluorescent dye-loaded microbubbles. This technology can help remove the high background level of unmodulated fluorescent photons in a scattering environment and allow the 2.25 MHz modulated signal to be detected.

Materials and Methods

Materials

Distearoyl phosphatidylcholine (DSPC) was purchased from Avanti Polar Lipids, Inc. (Alabaster, AL) and distearoyl phosphatidylethanolamine-methyl poly(ethylene glycol) MW5000 (mPEG-DSPE 5k) was purchased from Laysan Bio, Inc. (Arab, AL). Dulbecco's phosphate buffered saline (DPBS) was purchased from Hyclone Laboratories Inc. (Logan, UT). DiO was purchased from Biotium, Inc. CA. Perfluorohexane (PFH) was purchased from Sigma-Aldrich (St. Louis, MO).

Microbubble Preparation

The microbubbles were prepared as described in Chapter 1 for use in generating both fluorescence modulated signals and modulated photon scattering signals. The microbubbles used for detection in scattering media with the lock-in amplifier were treated with the rapid-cooling procedure described in Chapter 1. Microbubbles used in the harmonic fluorescence signal detection study were treated with the five thermal treatment regimens described in detail in Chapter 1.

Harmonic Signal Detection

The in-house acousto-optic detection system described in the literature [24, 72] used for the study described in Chapter 1 was also used here. As in Chapter 1, the 2.25 MHz ultrasound was pulsed at a 1Hz repetition rate with 15 sine wave cycles per pulse and a pressure of 1.0 MPa. The PMT signal was monitored directly and recorded using

custom-written LabView data collection software for analysis of harmonic signals when the microbubbles were in a non-scattering media. Three separate batches of microbubbles were manufactured and tested on three different days. The criteria used to scan for signals in Chapter 1 were modified here to look for 2nd, 3rd, and 4th harmonic peaks at 4.5, 6.75, and 9 MHz. To be considered a detected signal the intensity of the peak at these frequencies had to be at least 1.25 times the amplitude of the surrounding noise floor. The signals that met these criteria were tagged and counted for statistical analysis. Statistical significance between treatment conditions was determined using a chi-squared test with post hoc comparisons between groups using the Bonferroni adjustment ($p > 0.05$).

Fundamental Frequency Detection in Scattering Media

The same in-house acousto-optic detection system as mentioned above was used to detect the fundamental frequency in scattering media with the following modifications as shown in Figure 2.1. The output of the photomultiplier tube (PMT) and the 2.25 MHz sine wave created by the function generator were both plugged into an RF Lock-In Amplifier (Stanford Research Systems, Model SR844, Sunnyvale, CA). A T-junction splitter was used to allow the function generator to drive the ultrasound transducer and also serve as the reference signal for the lock-in amplifier. An oscilloscope was used to monitor the signal generated by the lock-in amplifier looking for the correlation signal that indicated a detected frequency match between the PMT signal and the 2.25 MHz reference signal. The microbubbles were detected at a 12.2 mm depth inside the scattering media. Two different ultrasound pressures were

investigated, as specified in the results. The scattering coefficient of the media was increased by adding increasing amounts of a solution of 20% Intralipid® (20% fat emulsion used for intravascular injection, Sigma-Aldrich St. Louis, MO). The volume of 20% Intralipid added to the tank was used to calculate the reduced scattering coefficient (μ_s') by using the μ_s' value measured from Driver et al. for 1% volume/volume Intralipid and the published approximation that μ_s' can be scaled linearly with Intralipid concentration [98]. A correction factor was applied to account for the μ_s' dependence on wavelength using wavelength dependence data published in Michels et al. [99]. The noise floor of the lock-in amplifier output signal was first measured while microbubbles were flowing through the system but no ultrasound was running. The ultrasound was turned on and the following signal increase was used to measure the signal to noise ratio. The signal to noise ratio for the modulated fluorescent signal generated by the microbubbles was compared to the signal to noise ratio from the modulated scattering signal.

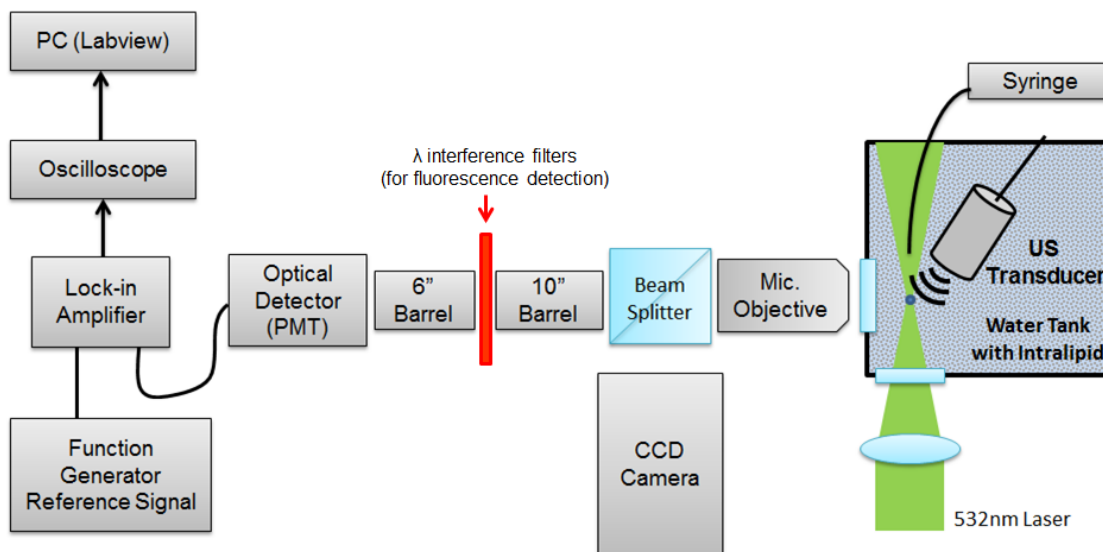


Figure 2.1 Schematic of the acousto-optic detection setup used to collect the modulated fluorescence signal from the dye loaded microbubbles. To detect scattered-light modulations, the wavelength interference filter was removed.

Results

Harmonic Signal Detection

The use of the thermal treatment techniques described in Chapter 1 to manipulate the microbubble shell nanostructure resulted in fluorescent signals that were intense enough to allow some of the microbubbles to produce detectable harmonic signals. An example of these harmonic signals is shown in Figure 2.2.

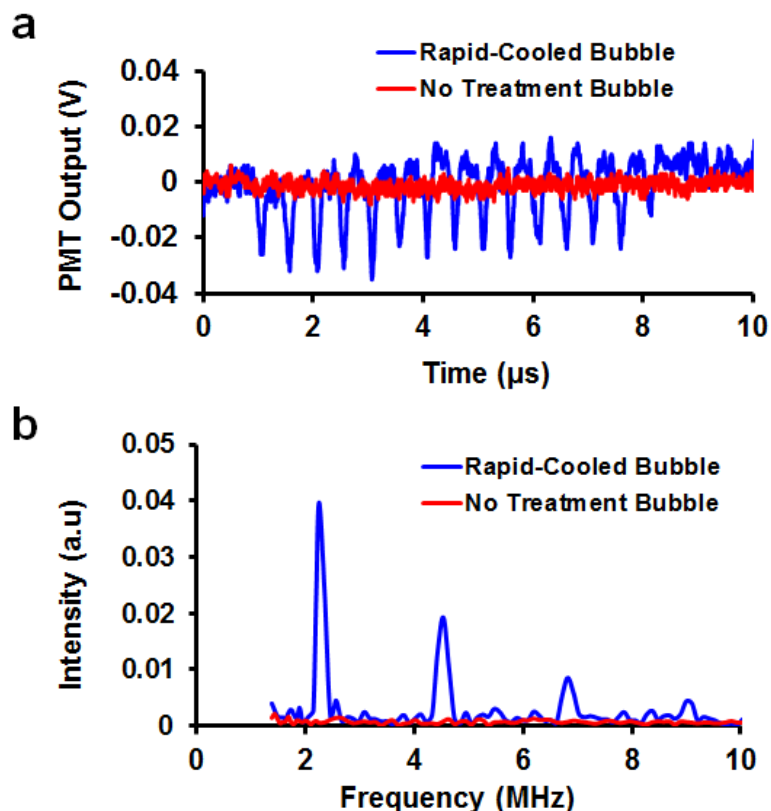


Figure 2.2 Example time and frequency domain signals acquired from rapid-cooled microbubbles that displayed harmonic signals and bubbles that were not temperature-treated. (a) Acquired time domain fluorescence signals. The rapid-cooled bubble signal shown here displays a fluorescence oscillation that is not seen in a typical untreated bubble. (b) Frequency spectra of the acquired fluorescence signals shown in panel a. The rapid-cooled microbubble displays clear peaks at the 2nd, 3rd and 4th harmonic frequencies of 4.5, 6.75, and 9 MHz. These peaks are lower in intensity than the peak at the fundamental driving frequency at 2.25 MHz. The untreated microbubble does not show any clear peak in the frequency spectra at either the fundamental or harmonic frequencies.

The percentage of microbubbles that displayed a detectable fluorescence intensity modulation as defined by the signal analysis threshold is shown for the different temperature treatment groups in Figure 2.3. A summary of this data is shown in Table 2.1. The rapidly-cooled microbubbles (3 minutes 75°C, 5 minutes 0°C)

displayed the highest incidence of harmonic signals of the 5 different heat treatment regimens which is consistent with the data observed for the fundamental frequency as discussed in Chapter 1. The microbubbles that underwent this rapid-cooling treatment had significantly higher percentages of 2nd and 3rd harmonics than the other treatments. The 4th harmonic observations were so rare that the small number of samples made statistical comparisons unreliable. However, 11 confirmed observations are enough to show that 4th harmonic signals can be generated and detected. There were no observed instances of 5th harmonic signals. Figure 2.4 shows the batch-to-batch variability for the different thermal treatment regimens.

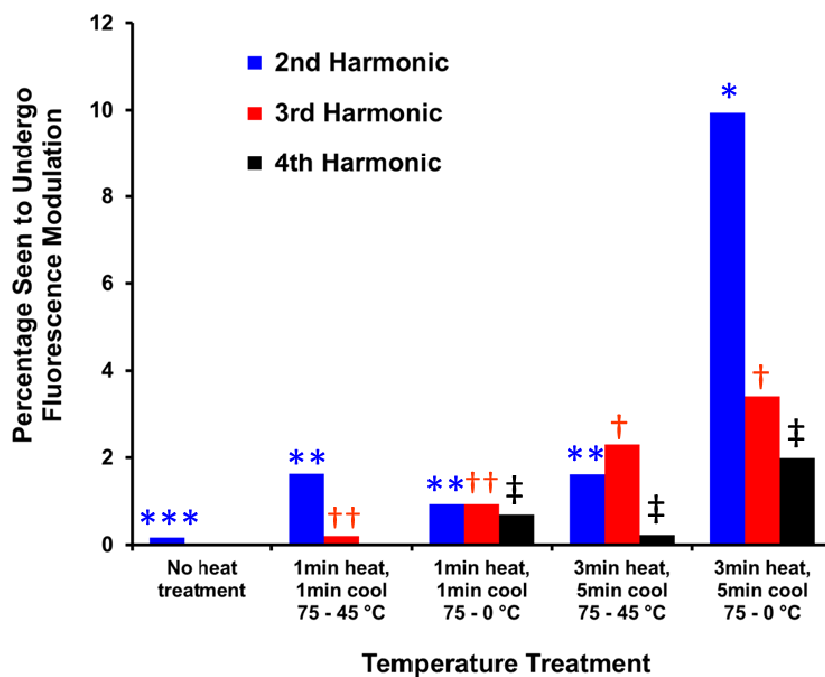


Figure 2.3 Percentage of microbubbles produced under the different thermal treatment processes that displayed a detectable 2nd, 3rd, and 4th harmonic signal. Percentages of microbubbles that produced detectable harmonic fluorescence modulations combining all the signals acquired from three microbubble batches for all five temperature treatments (combined bubble count data shown in Table 2.1). The symbols indicate statistically significant differences using a chi-square test with post hoc comparisons between groups using the Bonferroni adjustment ($p > 0.05$). The 4th harmonic signals were relatively rare to observe and did not lend themselves to reliable statistics, but the data documents the ability to generate 4th harmonic signals in the rapidly-cooled microbubbles. As can be seen the rapidly-cooled microbubbles (3 minutes 75°C, 5 minutes 0°C) had a higher percentage of microbubbles displaying detectable harmonic signals than the other treatments especially in the 2nd harmonic.

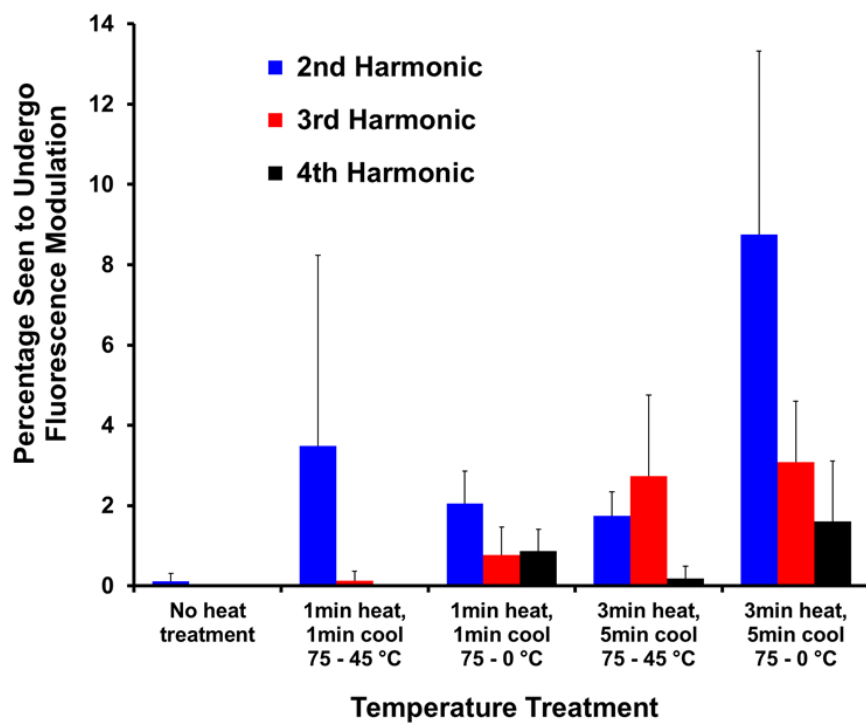


Figure 2.4 Batch-to-batch variability of the detectable harmonic fluorescence modulation percentage for each temperature treatment. Data is shown as the mean fluorescence modulation percentage and standard deviation of three batches of microbubbles prepared and analyzed on separate days.

Table 2.1 Summary of the absolute numbers of microbubbles made under different thermal treatment regimens that displayed detectable higher harmonic signal production.

		Treatment				
		No Treatment	3 min heat, 5 min cool 75 - 0 °C	3 min heat, 5 min cool 75 - 45 °C	1 min heat, 1 min cool 75 - 0 °C	1 min heat, 1 min cool 75 - 45 °C
2nd Harmonic	No Modulation	627	317	427	427	482
	Modulation	1	35	7	4	8
3rd Harmonic	No Modulation	628	340	424	427	489
	Modulation	0	12	10	4	1
4th Harmonic	No Modulation	628	345	433	428	490
	Modulation	0	7	1	3	0

Fundamental Frequency Detection in Scattering Media

The SNR of the modulated scattering signal and the modulated fluorescence signal at different ultrasound intensities and in media of different scattering coefficients is shown in Figure 2.5. The scattering properties of the media were manipulated by using increasing concentrations of 20% Intralipid in the water tank. Due to the wavelength dependence of the reduced scattering coefficient (μ_s') there is a slight difference in the plotted μ_s' value between the fluorescence (emission at 570 nm) and scattered photon (532 nm) modulating bubbles for a given Intralipid

concentration. At ultrasound pressures of 1.3 MPa (peak to peak), the modulation of the fluorescence signal created a SNR that was approximately 1.3 times higher than the SNR for the modulated scattering signal at the lowest Intralipid concentration tested. It should be noted that at zero Intralipid concentration, the internal structures of the water tank still likely produced a nonzero amount of scattering and some small amount of scattering particles were likely present in the water itself. As the scattering coefficient of the media increased the amount of light reaching the PMT decreased causing a reduction in the overall SNR resulting in a convergence of the modulated fluorescent signal and modulated scattered-light signal SNR values.

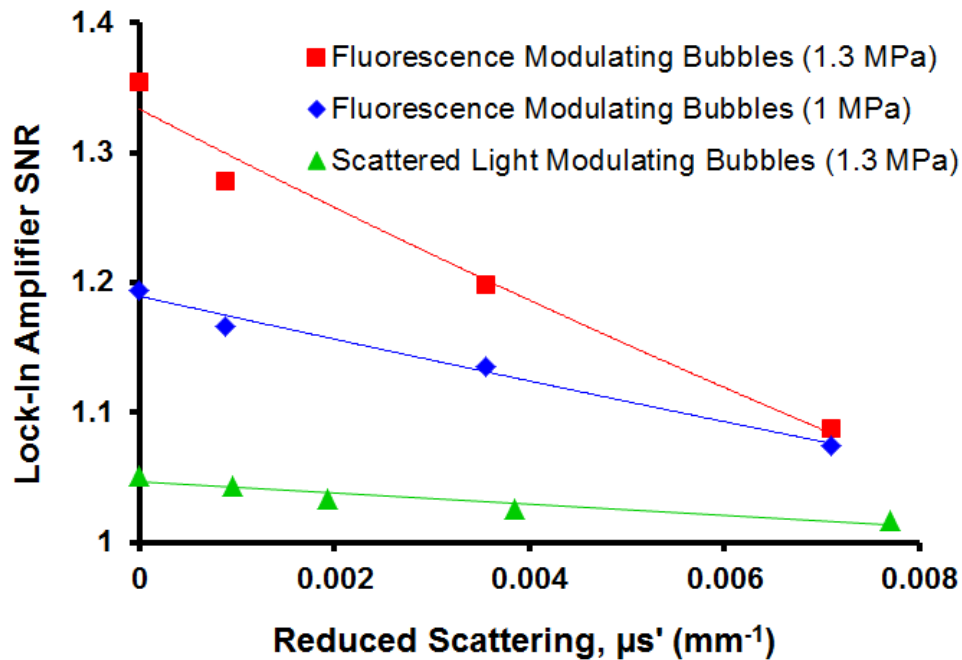


Figure 2.5 The lock-in amplifier signal to noise ratio (SNR) for both the fluorescence modulated and scattered light modulated signals versus the reduced scattering coefficient of the media. The SNR for the fluorescence modulated signal at 1.3 MPa (peak to peak) was 1.3 times higher than the SNR for the scattered light modulated signal at low values of scattering coefficient. As expected, when the ultrasound pressure was reduced to 1 MPa (peak to peak), the SNR for the fluorescence modulated signal was also reduced due to the reduction in the size oscillations that the microbubbles underwent.

Discussion

The rapid-cooling treatment of the microbubble contrast agents as described in Chapter 1 produced microbubbles capable of producing detectable modulated fluorescent signals at the 2nd, 3rd, and even 4th harmonics when in a non-scattering media. As illustrated in Chapter 1, the rapid-cooling procedure results in a more even

distribution of the lipids and dye on the microbubble shell. The distributed dye formation appears better able to translate the asymmetric oscillations of the microbubble into detectable fluorescence modulations at the harmonic frequencies, likely due to the more favorable dye-dye separation distance on the rapid-cooled bubbles which is elaborated upon in Chapter 1. These higher harmonics signals which are produced solely by the microbubbles can provide a means to avoid background interference from other signals at the fundamental frequency, such as electrical noise or other acousto-optic effects on tissue.

When in a scattering media, the fluorescence modulated signal at the fundamental frequency produced by the dye-loaded contrast agent microbubbles yielded a higher SNR when compared to the modulated scattering signal. This was observed in media both with and without Intralipid. The improvement in the detection of the fluorescence modulated signal in scattering media is most likely due to the fact that the fluorescent photons generated by the microbubble contrast agents were produced independently of any scattering mechanism. The fluorescence modulation involved the creation of higher and lower numbers of fluorescent photons in time due to the microbubble size oscillations. This populated the scattering media with higher and lower numbers of photons. The only interference scattering had on the collected signal was in creating a constant reduction in the amount of the photons that reached the detector by increasing their path length through the media and also increasing their likelihood of water absorption.

The scattering modulation had a lower SNR in comparison to the fluorescence modulation because unlike the fluoresce modulation, the scattering modulation

mechanism did not cause an increase and decrease in the number of photons being created in the scattering media over time. The photons were introduced into the media from the outside excitation source and the number of photons in the media was constant over time. The microbubbles' size expansion and contraction created variable scattering bodies that in a non-scattering media would scatter photons towards the detector in a time-varying fashion. This detectable scattering effect was easily overwhelmed by the bulk scattering that occurred when the microbubbles were inside a scattering media because the photons were being scattered towards the detector by the media itself. It is important to note that the lock-in amplifier requires the generation of an oscillating signal of long enough duration in order to amplify the signal out of the noise. This was enabled by the consistent generation of a modulated-fluorescence signal of detectable amplitude made possible by the microbubble rapid-cooling described in Chapter 1. It may also be possible to detect higher harmonic fluorescence modulations in scattering media using the lock-in amplifier approach. A potential issue for harmonic detection is that the lower incidence of higher harmonic signals may not provide signals of long enough duration for the lock-in amplifier to extract. Future work will investigate the ability of the feasibility of this detection approach. In the future, the number of microbubble-generated fluorescent photons that exit the scattering tissue and reach the detector could be improved by replacing the red fluorophores in the current bubble design with near-infrared fluorophores which have better tissue-penetration.

Conclusions

The rapid-cooling thermal treatment method for manufacturing the microbubbles as described in Chapter 1 produced microbubbles capable of generating detectable modulated fluorescence signals at the 2nd, 3rd, and even 4th harmonic modes of microbubble vibration. The rapidly-cooled microbubbles (3 minutes 75°C, 5 minutes 0°C) had a statistically significant higher percentage that produced 2nd and 3rd harmonic signals. The detection of 11 4th harmonic signals shows that although rare it can be produced under these conditions. The detection of these higher harmonic signals opens up the possibility of using them to increase the SNR even further avoiding any background from the 2.25 MHz fundamental driving frequency.

The fluorescence modulated signal generated at the fundamental frequency by the contrast agent microbubbles was detected for the first time in a scattering media environment. The SNR of the modulated fluorescence signal was higher than the SNR of the modulated scattering signal. The scattered light modulation signal of the microbubbles was lost in the bulk scattering of the media whereas the production of the fluorescence modulation was independent of scattering and was less affected.

Acknowledgements

Support was provided by Grant Numbers T32 CA121938 and R25 CA153915 from the National Cancer Institute. The content is solely the responsibility of the authors and does not necessarily represent the official views of the National Cancer Institute or the National Institutes of Health.

Chapter 2, in part, is currently being prepared for submission for publication of the material. Carolyn Schutt, Stuart Ibsen, Michael Benchimol, Mark Hsu, Sadik Esener. The dissertation author was the primary investigator and author of this material.

Chapter 3

Toward Ultrasound-Enhanced Drug Delivery:

The Influence of Distance Between Microbubbles on the Fluid Flow
Produced During Ultrasound-Mediated Inertial Cavitation

Abstract

Microbubbles that undergo inertial cavitation while in contact with a rigid or flexible boundary form fluid jets that are directed perpendicularly toward the boundary surface. The formation of this perpendicular jet is desirable when using the microbubbles to create damage in the microcapillaries of a tumor to enhance drug extravasation and delivery. However, more damage could be caused by influencing the concentrated jet to have a directional component that is horizontal to the capillary surface allowing the jet to affect a larger surface area. This study investigated the influence of inter-microbubble distance on the horizontal directional component of jet formation through the observation of lipid debris clouds created by the destruction of the microbubble lipid monolayer. It was observed that at distances smaller than 37 μm the microbubbles began to interact with one another resulting in distorted and ellipsoid-shaped debris clouds suggesting the creation of a horizontal directional component in the jet. At inter-microbubble distances less than 10 μm , significantly elongated debris clouds were observed. These distortions show a significant distance dependent interaction between microbubbles that influences the direction of the jet. It was observed that microbubbles in physical contact with one another exclusively caused these significantly elongated debris clouds.

Introduction

The use of microbubbles as drug delivery vehicles has become a field of considerable interest in recent years [100-105]. One of the unique properties of microbubbles that distinguishes them from other drug delivery vehicles is their sensitivity to focused ultrasound. The compressibility of the gas within the microbubble allows the ultrasound to drive size oscillations creating a mechanical actuation force. At low ultrasound intensities these size oscillations result in microstreaming of fluid around the microbubble [106]. At higher ultrasound intensities, and at the correct ultrasound frequency, resonance behavior can be achieved, resulting in size oscillations that are large enough to force the microbubble to undergo an adiabatic implosion known as inertial cavitation [107]. This cavitation event produces a shockwave that radiates out from the microbubble itself and can affect the membranes of nearby cells [108, 109]. An attractive property of these shockwaves is that they can compromise the integrity of the membranes of nearby cells in a process known as sonoporation. This modification in membrane permeability can occur for periods of time that are long enough [110, 111] to allow nearby drugs to flow down their concentration gradient and enter the cell [110, 112]. Sonoporation is a widely-used in-vitro method to help facilitate gene transfection into cell populations [108]. It is also being explored to help increase drug delivery in-vivo [113].

Microbubble-enhanced drug delivery can extend from the cellular level to whole capillaries. Microbubbles used as clinical ultrasound contrast agents are approximately 2.5 μm in diameter [114] which prevents them from easily

extravasating into tissues forcing them to stay mainly in the circulation [115]. Their compressibility and small size allows them to travel through the microcapillaries [116]. If the microbubbles are exposed to ultrasound and undergo inertial cavitation while in the capillaries they can cause capillary rupture [33]. These ruptures can assist other drug delivery particles to extravasate from the circulation to the target tissue. This is of interest for drug delivery in cancerous tumors. Tumors naturally have a “leaky” vasculature [35] with discontinuous endothelium that allows nanoparticle drug delivery vehicles, such as Doxil[®], to passively extravasate and accumulate in tumor tissue over time [117, 118]. These vehicles slowly release their payloads into the tissue resulting in therapeutic effect. This extravasation effect can be enhanced by microbubble-induced capillary ruptures [33, 34]. This could help overcome one of the major limitations in drug delivery which is getting enough of the drug delivery vehicle into the tissue for a therapeutic effect. The ultrasound can be focused to small volumes [18] allowing the capillary damage to be limited to the tumor tissue and leaving tissues outside the tumor unaffected.

There are two main types of microbubble inertial cavitation shockwaves that can rupture capillaries. The first is a symmetric collapse of the microbubble with a resulting radial expansion of the shockwave [107]. The second is an asymmetric collapse of the microbubble resulting in a jet of fluid [22, 119]. The asymmetric collapse of microbubbles is of particular interest because it concentrates the energy into a smaller volume [120] and can project that energy for longer distances [120]. This can result in additional capillary damage by dislodging cells and causing endothelial cell death.

The direction of the jet can play an important role in the size of the damaged capillary surface region. When laser-created bubbles in the 2-3 mm diameter range come into direct contact with a rigid surface they undergo an asymmetric collapse pointed directly at the surface. This dissipates the energy of the jet in a radial pattern across the surface causing the bubble to appear to flatten out over the rigid surface [36, 37]. When these laser-created bubbles come into direct contact with a flexible surface, such as a gel, they too jet directly towards the surface [38]. A microbubble that produces a fluid jet aimed directly at the microcapillary wall will induce limited localized damage to a single cell, or a small group of cells. Influencing the jet to have a directional component that is parallel to the capillary wall will expose a larger group of cells to the concentrated energy and cause more endothelial cell dislodgement. Finding ways to redirect the jet would be beneficial for drug delivery and antitumor applications.

Little is known about the jetting behavior of preformed microbubbles stabilized with a lipid coating that are in the clinically relevant size range of 1-3 μ m in diameter. Larger microbubbles are unable to enter the microvasculature and are removed quickly from circulation. Most observations of microbubble jet formation have been conducted with uncoated laser-generated microbubbles larger than 100 μ m in diameter near a rigid surface [120, 121], or at the air-water interface [122]. Asymmetric collapse with jet formation has been observed with lipid coated microbubbles in the 10-20 μ m diameter range [22, 123]. However, microbubbles in the 1-3 μ m diameter range are too small to allow for reliable direct observation of the involution of an asymmetric collapse using white light imaging. Direct observation is

useful at this size scale to monitor secondary Bjerknes forces that cause translations, merging [124] and cluster formation between microbubbles [61, 125]. However, the optical distortions created by the index of refraction difference between the gas and the surrounding water as well as the microbubbles' small size obscure the actual dynamics of collapse and involution that is the hallmark of jet formation. This makes directly observing the collapse dynamics and determining jetting direction in a statistically significant number of 1-3 μm microbubbles a challenge.

To overcome the limitations of direct observation at this small size scale fluorescence imaging was used to study the fluid flow that occurred as a result of the microbubble inertial cavitation event. A fluorescent dye was incorporated into the lipid monolayer that surrounded each microbubble. The inertial cavitation event fragmented the lipid monolayer into a fine debris cloud that was larger than the original microbubble and did not suffer from any optical distortions from the gas. The shape of the fluorescent debris cloud revealed details about the direction of the jet through the resulting fluid motion. The 1-3 μm diameter lipid-coated microbubbles studied here were positioned against a glass cover slip which served as a rigid surface. If these 1-3 μm diameter bubbles behaved in a similar manner to millimeter sized bubbles they too should jet towards the surface and flatten out over the glass creating a circular lipid debris cloud which could be monitored by fluorescence microscopy. The formation of a fluid jet with a strong horizontal directional component along the surface of the glass would result in an elongated debris cloud that could extend beyond the physical location of the original microbubble.

This study investigated if the direction of jetting could be influenced and directed horizontally along the surface by ensonifying microbubbles as pairs with varying inter-microbubble distances. It has been demonstrated with bubbles on the millimeter scale that bubble oscillation behavior is affected by the proximity of the bubbles to one another. Two distinct millimeter scale uncoated bubbles generated by dual laser pulses have been shown to create jets toward each other as they collapse [37]. Microbubbles also change their oscillation behavior as they approach one another, producing chaotic type oscillations [126]. The shape and symmetry of the fluorescent lipid debris clouds created by the two microbubbles can be used to determine if a horizontal component of the jet was produced.

Materials and Methods

Materials

Distearoyl phosphatidylcholine (DSPC) was purchased from Avanti Polar Lipids, Inc. (Alabaster, AL) and distearoyl phosphatidylethanolamine-methyl poly(ethylene glycol) MW5000 (mPEG-DSPE 5k) was purchased from Laysan Bio, Inc. (Arab, AL). Dulbecco's phosphate buffered saline (DPBS) was purchased from Hyclone Laboratories Inc. (Logan, UT). 3,3'-dioctadecyloxycarbocyanine, perchlorate (DiO) was purchased from Biotium, Inc. (Hayward, CA). Perfluorohexane (PFH) was purchased from Sigma-Aldrich (St. Louis, MO).

Microbubble Fabrication

To fabricate lipid-coated microbubbles, stock solutions of lipid and lipophilic dye were prepared in chloroform at 20 mg/ml DSPC, 50 mg/ml mPEG-DSPE 5k, and 1 mM DiO. 50 μ l of the DSPC solution, 20 μ l of the mPEG-DSPE 5k solution, and 30 μ l of the DiO were successively added to a 4 ml glass vial while vortexing. The amount of DiO in the combined solution was 2 mol % of the total lipid and dye content. The chloroform was evaporated under an argon gas stream while the solution was under vortex. This created a lipid film along the inner surface of the vial. A volume of 500 μ l of DPBS was added to the film and the lipids and dye were resuspended by vortexing the vial for 15 seconds followed by heating at 75 °C for 1 minute. The cycle of vortexing and heating was repeated until the lipids were well suspended and no lipid residue was left on the vial walls. The sample was left to cool to ambient temperature.

To create the gas microbubbles, the top of the vial was first covered with Parafilm to create a barrier between the gas in the vial and outside the vial. A 5 ml syringe equipped with a 22 gauge needle was used to draw up 1 ml of liquid PFH. With the plunger fully drawn back, the syringe was rotated to coat the walls with the liquid PFH and left to sit for at least 3 minutes to encourage vaporization of PFH into the air within the syringe creating an air/PFH vapor mixture. The syringe needle was then bent at a 130° angle into a hook shape and was inserted through the Parafilm cover into the vial headspace. Next, the syringe was pumped 65 times into the vial headspace to inject the PFH/air mixture into the vial headspace. Care was taken to prevent any liquid PFH from entering the vial. The XL-2000 probe sonicator (QSonica

LLC., Newtown, CT) tip was immediately inserted through the Parafilm cover and positioned 1 mm below the gas/liquid interface. The probe sonicator was then operated at 25 W for 3 seconds to create microbubbles. The resulting bubbles were left to sit for at least 5 minutes before further processing.

Excess lipid and dye was removed from the microbubble sample by a washing procedure. The microbubbles were moved to a microcentrifuge tube and centrifuged at 1000 rpm for 3 minutes which caused the bubbles to float to the top of the liquid. The supernatant was partially removed and replaced with additional DPBS. This process was repeated 1-3 additional times and helped to reduce fluorescence background in the images from dye that was not associated with bubbles.

Ultrasound Exposure

The ultrasound experiments were carried out using a custom-designed system that combined fluorescence imaging with ultrasound [127]. A schematic of the system and the sample holder setup for these experiments is shown in Figure 3.1.

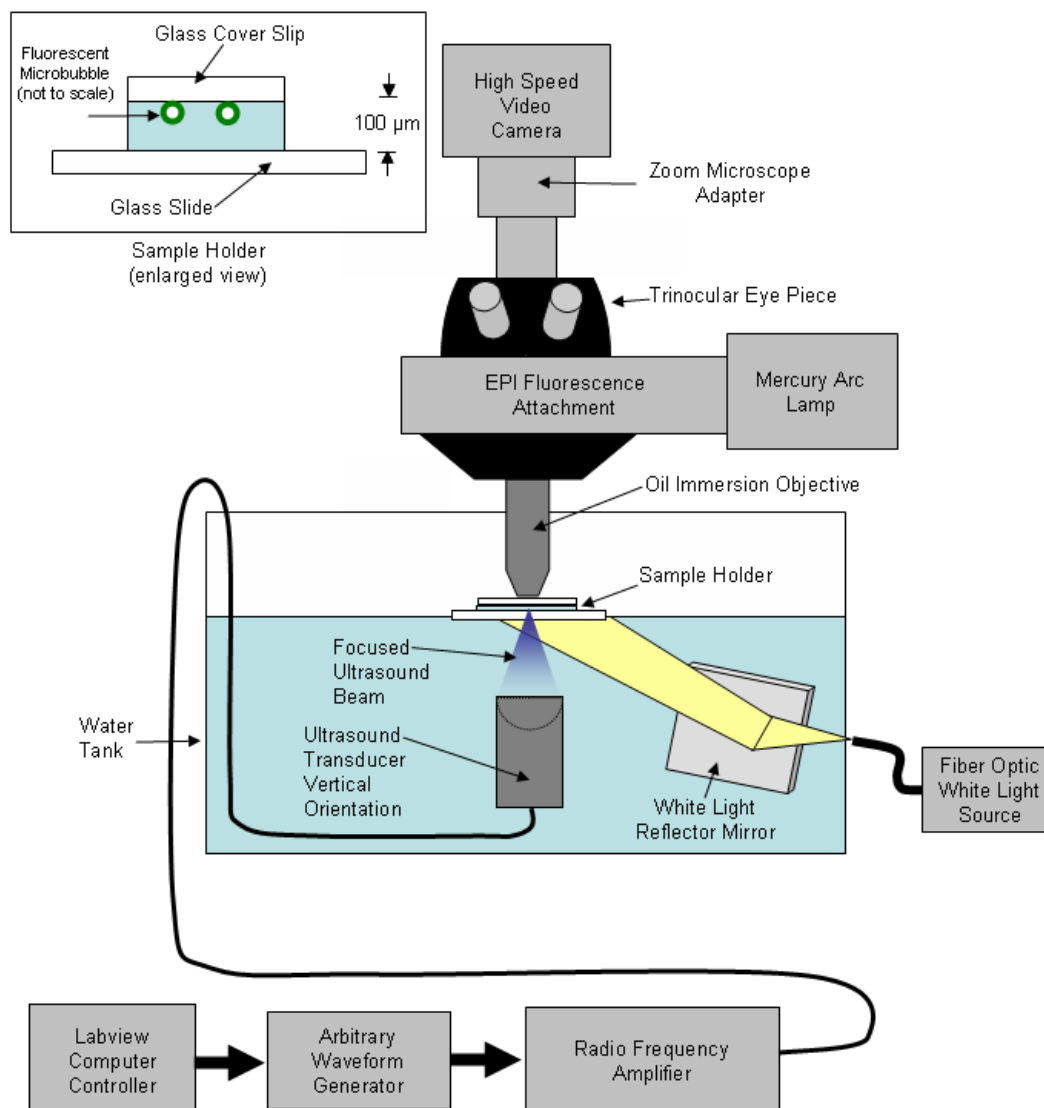


Figure 3.1 Schematic diagram of the microscope system and sample holder setup used to observe and record the interaction of the fluorescent microbubbles with the focused ultrasound [127].

A ten gallon tank of water was used to allow coupling between the ultrasound transducer and the microbubble sample. The fluorescent microbubbles in MilliQ purified water were placed in 10 μl samples on a glass microscope slide and then covered with a glass cover slip for imaging. The glass slide was then placed at the air-

water interface such that just the bottom of the slide was in contact with the water. By preventing the water level from reaching the top of the glass slide, the microbubble sample was prevented from being washed into the tank water. Positioning the microbubble sample at the air-water interface allowed a 100X oil immersion objective to collect the images. The use of a high numerical aperture oil immersion objective allowed more fluorescent light to be collected from the microbubbles in order to achieve higher frame rates and allow debris cloud resolution.

The contact between the bottom side of the glass slide and the water allowed the ultrasound to travel through the water and hit the bottom of the glass slide. The ultrasound intensity was attenuated by the glass but not enough to prevent microbubble cavitation from occurring in the sample.

A 3 minute time delay between sample preparation and exposure to ultrasound allowed all the microbubbles to settle up against the glass cover slip due to their buoyancy. This ensured that there were no microbubbles in different focal planes and allowed all the microbubbles to be visible to the optical system.

The ultrasound was focused to a 1 mm² focal cross-sectional area allowing microbubbles within this region to be affected by the ultrasound pulse. The samples were scanned for microbubble pairs at different distances from one another. Once a group was identified it was centered into the ultrasound focal zone and hit with an ultrasound pulse that consisted of a 10 ms 2.25 MHz sine wave with a pressure of 1.6 MPa (peak-to-peak). Inertial cavitation of microbubbles can begin to occur at ultrasound peak pressure amplitudes as low as 0.58 MPa [128]. The interaction was recorded at 60 frames per second and saved for subsequent analysis.

Video Analysis

The videos were analyzed using ImageJ software to measure the starting edge-to-edge distance of each microbubble to its nearest neighbor microbubble (“inter-bubble distance”) before ultrasound exposure. Isolated microbubbles with no other microbubbles visible in the microscope field of view were assigned the distance between the bubble edge and the edge of the field of view. The inertial cavitation event caused the fluorescent lipid monolayer on the microbubbles to fragment leaving behind a debris cloud. The dimensions of the fluorescent debris cloud for each microbubble were then measured and assigned to one of three categories. The first category was radial, where a circular pattern of debris was seen, resulting from conditions where the fluid jet was pointed normal to and directly toward the cover glass surface with little or no horizontal directional component. Debris clouds where there was less than a 1.3-fold difference between length (the longer dimension) and width were assigned to the radial category, The second category was ellipsoid where a debris cloud was produced that was between 1.3 to 2 times longer than its width, resulting from a detectable horizontal directional component in the fluid jet. The third category, denoted as “elongated” was where the inertial cavitation resulted in a large horizontal directional component of the fluid jet which distorted the debris cloud into an elongated shape such that its length was greater than 2 times the width.

Results

Debris Cloud Observation

A series of still frames from the collected videos showing different microbubble debris cloud forms is shown in Figure 3.2. Figure 3.2A, B and C show two microbubbles at an edge-to-edge distance of 36 μm . These microbubbles did not appear to influence one another's cavitation behavior and both created radial debris clouds. Figure 3.2D, E, and F show microbubbles at a starting distance of 8.0 μm . Some interaction appears to have occurred between the bubbles and distorted their fluorescent debris clouds into ellipsoid shapes. Figure 3.2G, H, and I show microbubbles at a starting distance of 9.3 μm . The microbubbles appear to have interacted with each other to distort both of their debris clouds into highly elongated forms that extend well beyond the original locations of the microbubbles. The debris cloud shape could not have been a result of Bjerknes forces alone since it extends beyond the original microbubble locations. The debris field could have been produced by the fluid jets having a significant directional component that was horizontal to the glass surface pushing the lipid debris out along the glass surface.

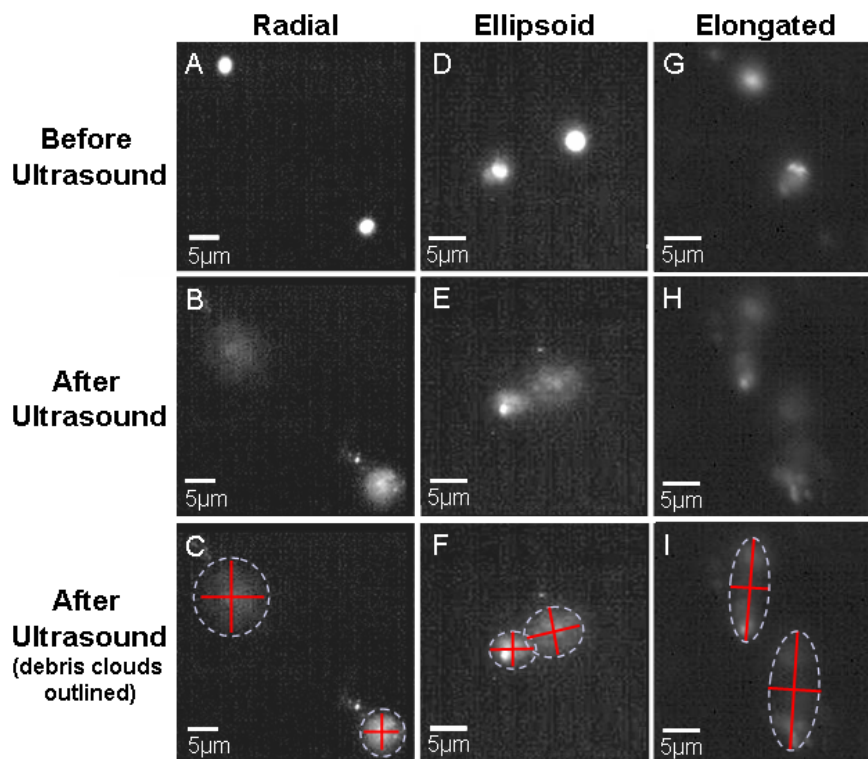


Figure 3.2 Still frames from videos showing examples of the three categories of debris cloud expansion. (A) Two fluorescent microbubbles are shown before ultrasound exposure with an edge-to-edge distance of $36\ \mu\text{m}$. (B) The two microbubbles did not appear to interact with each other during cavitation and the resulting debris clouds from cavitation are both radial in shape as shown in frame C. (D) Here the microbubbles have an edge-to-edge distance of $8.0\ \mu\text{m}$ before ultrasound exposure. (E) The microbubbles interacted with one another and distorted the shape of the resulting two debris clouds created by the cavitation shockwave to be ellipsoid in shape as shown in frame F. (G) Here the two microbubbles have edge-to-edge distance of $9.3\ \mu\text{m}$ before ultrasound exposure. (H) The microbubbles interacted with each other during cavitation and a horizontal directional component of the jet was formed resulting in a long distortion of both of the lipid debris clouds. (I) The dimensions depicted indicate two elongated debris clouds with lengths greater than 2 times their heights.

Figure 3.3 shows three microbubbles that are in physical contact with one another before exposure to ultrasound. The resulting debris cloud took an elongated shape indicating a horizontal directional component of the fluid jet.

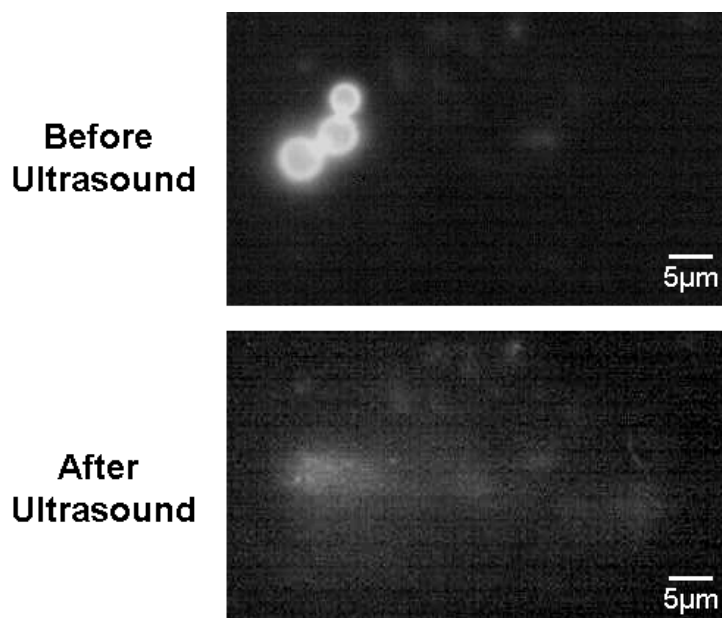


Figure 3.3 Three microbubbles are in physical contact with one another before ultrasound exposure. Upon exposure to ultrasound the resulting elongated lipid debris cloud shows the formation of a horizontal directional component in the fluid jet. All other microbubble pairs or triplets in physical contact prior to ultrasound exposure were also observed to form elongated debris clouds.

Analysis of Debris Cloud Shape Dependence on Inter-Microbubble Distance and Microbubble Size

A total of 76 microbubbles were analyzed for debris cloud shape, microbubble size, and inter-bubble distance. The data is summarized in Table 3.1.

Table 3.1 Summary of microbubble data acquired from video analysis.

		N	Mean	Std. Deviation	Std. Error	95% Confidence Interval for the Mean		Min	Max
						Lower Bound	Upper Bound		
Distance Between Microbubbles in μm	Radial	25	55.5902	41.05703	8.21141	38.6427	72.5377	17.90	169.17
	Ellipsoid	11	22.1024	9.74174	2.93724	15.5578	28.6470	9.37	38.54
	Elongated	40	10.6507	9.66026	1.52742	7.5612	13.7402	.00	35.90
	Total	76	27.0909	31.92386	3.66192	19.7960	34.3858	.00	169.17
Microbubble Diameter in μm	Radial	25	2.6106	.73308	.14662	2.3080	2.9132	1.40	4.91
	Ellipsoid	11	2.7336	1.02695	.30964	2.0437	3.4235	1.93	5.67
	Elongated	40	4.2110	2.00580	.31715	3.5695	4.8525	1.42	11.35
	Total	76	3.4707	1.73875	.19945	3.0734	3.8680	1.40	11.35

Box plots of the inter-microbubble distances for the three different cavitation debris cloud shape categories are shown in Figure 3.4. The data was not normally distributed so a two-tailed nonparametric Kruskal-Wallis Test was performed at the 0.05 significance level. A significant difference was found in inter-microbubble distance between the three debris cloud shape categories ($p < 0.001$). Post hoc comparisons using the Dunn-Sidak adjustment showed a significant difference between the inter-microbubble distances that resulted in radial debris clouds and those that resulted in elongated debris clouds ($p < 0.001$). There was also a significant difference between the distances that resulted in ellipsoid debris clouds and elongated debris clouds ($p = 0.041$). The difference between the microbubble distances that resulted in radial debris clouds and those that resulted in ellipsoid debris clouds trended towards significance ($p = 0.067$). All statistical calculations were performed using IBM® SPSS® Statistics Version 21 software.

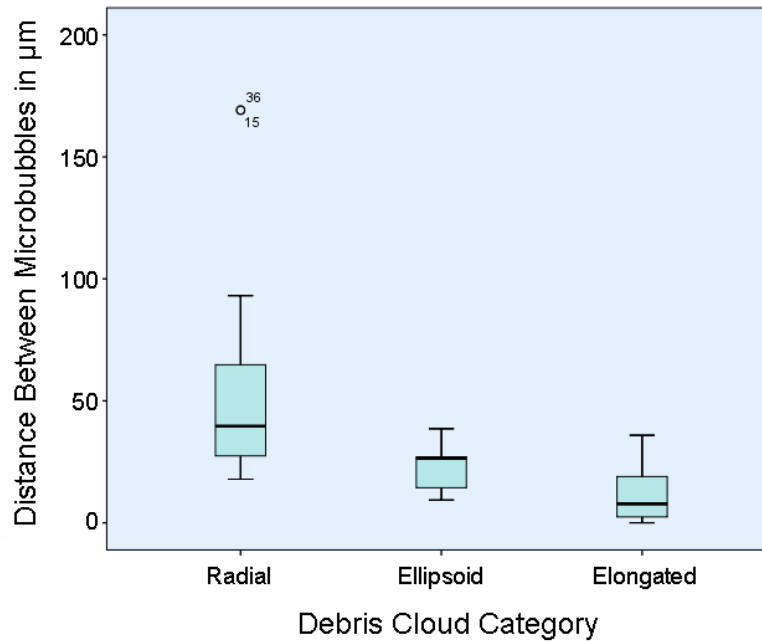


Figure 3.4 Box plots of the distance between the microbubble and its nearest neighbor in microns for each of the three debris cloud expansion categories. Whiskers denote maxima and minima and the median is represented as the horizontal line. Outliers were defined as any points that were two standard deviations away from the mean and are indicated as open circles. The radial and elongated debris cloud categories and the ellipsoid and elongated categories were found to be statistically significant from each other ($p < 0.001$ and $p = 0.041$, respectively) with regard to inter-microbubble distance. The difference in inter-bubble distances resulting in radial and ellipsoid debris clouds trended toward significance ($p = 0.067$).

Box plots of the diameter of the microbubbles in the three different debris cloud expansion categories are shown in Figure 3.5. There was no significant difference between the microbubble diameters of bubbles that produced radial and ellipsoid debris clouds ($p = 1$) using the same statistical test described for the above comparisons of inter-bubble distance. There was a significant difference between the diameters of bubbles that produced radial debris clouds and those that resulted in

elongated debris clouds ($p < 0.001$). This difference was likely a result of the larger microbubbles being generally closer to one another than the smaller bubbles in the study population, perhaps caused by the manner in which these bubbles settled at the liquid-coverslip interface. It is possible that the larger microbubbles created flow patterns around their perimeter as they rose up in the fluid due to buoyancy forces. These flow patterns could have pulled the microbubbles together before they stopped their motion at the interface with the glass coverslip. There was also a significant difference between the diameters of bubbles that produced ellipsoid debris clouds and elongated debris clouds ($p = 0.009$) which was likely also caused by the closer inter-bubble distance seen with larger microbubbles.

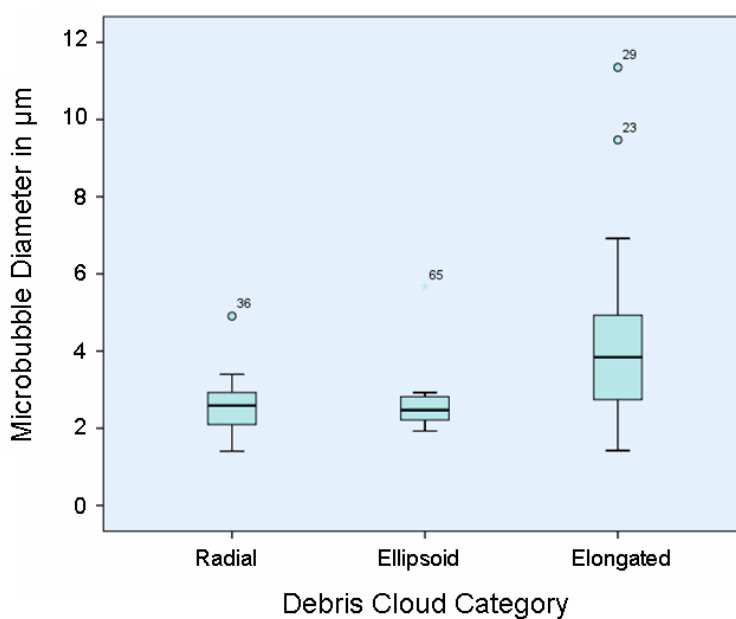


Figure 3.5 Box plots for the diameter of the microbubbles in each of the three debris cloud expansion categories. Whiskers denote maxima and minima and the median is represented as a horizontal line. Outliers were defined as any points that were two standard deviations away from the mean and are indicated as open circles.

A scatter plot of the diameter of the microbubble versus the inter-microbubble distance is shown in Figure 3.6 and is color coded to the three different debris cloud categories. A clear pattern can be seen where radial debris cloud expansion occurs at the larger inter-microbubble distances and ellipsoid and elongated debris clouds occur only at the smaller distances. Ellipsoid formation was observed to begin occurring at inter-microbubble distances of 37 μm . Below 10 μm in inter-microbubble distance, bubbles were seen to exclusively produce elongated debris clouds.

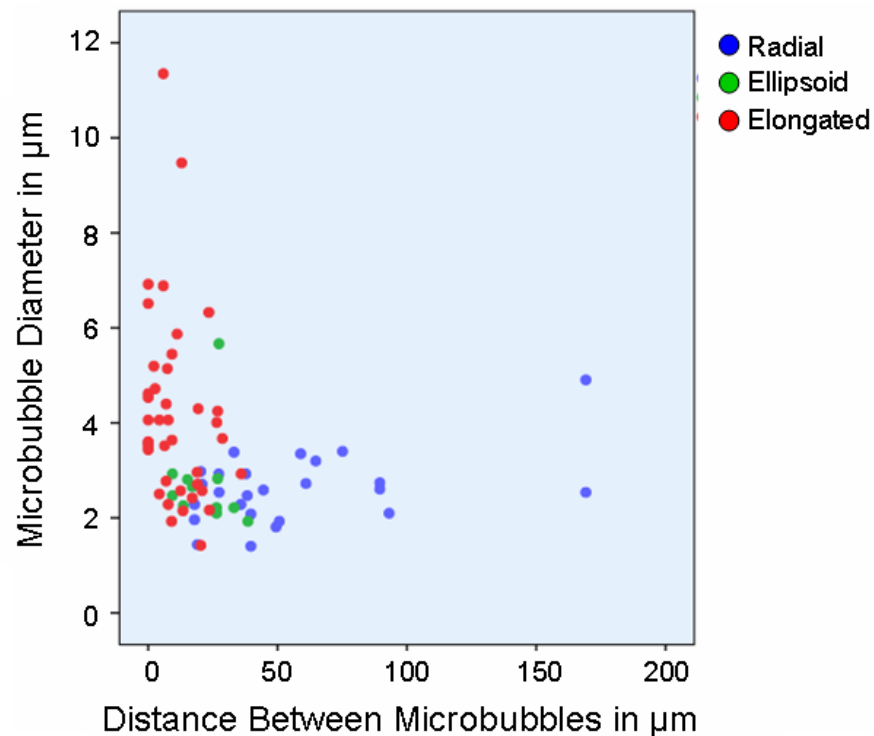


Figure 3.6 Scatter plot showing the diameters of the microbubbles plotted against distance between the microbubble and its nearest neighbor. Points are color-coded to the shape of the debris cloud. A trend is observed where radial expansion is seen at larger inter-microbubble distances and ellipsoid and elongated debris cloud formation are seen at the shorter distances.

Discussion

As can be seen in Figures 3.2 and 3.3, the distance between microbubbles had an impact on the morphology of the resulting fluorescent lipid debris cloud. These debris clouds were produced by the fragmentation of the fluorescent lipid monolayer that surrounded and stabilized the surface of the original microbubbles. The morphology of the debris cloud was highly influenced by fluid flow and revealed information about the directional components of the fluid jet resulting from microbubble collapse. In our experimental setup, the interaction between microbubbles began to distort the shape of the debris cloud at inter-microbubble distances shorter than 37 μm resulting in ellipsoid debris clouds. At an inter-microbubble distance of around 25 μm the microbubbles were interacting more extensively and the microbubble cavitation events more frequently resulted in elongated forms indicating a substantial horizontal directional component to the fluid jet. Microbubbles that had less than 10 μm of separation or were in physical contact with one another prior to ultrasound exposure were always seen to result in elongated debris clouds.

Two types of interactions were likely occurring between microbubbles in this study when ensonified with ultrasound. The first was the influence of microstreaming fluid flow around each microbubble that occurred as the microbubbles started to oscillate just before the cavitation event. The second were the secondary Bjerknes forces that caused microbubble attraction. This microbubble attraction is shown in Figure 3.2D and E. In Figure 3.2D the microbubbles start at a center-to-center distance

of 11.0 μm but the resulting debris clouds in Figure 3.2E have a center-to-center distance of 6.5 μm indicating that the microbubbles attracted each other before they cavitated. If the microbubbles were attracted to one another just before the cavitation event then the microstreaming occurring around each microbubble could also easily influence the individual microbubble oscillations. This influence would grow in intensity as the microbubbles became closer to one another causing distortions in the collapse of the microbubble towards the glass surface and creating horizontal directional components in the jet. In this particular experimental setup, the inter-bubble distance at which the microstreaming and Bjerknes forces appeared to start to influence the microbubble oscillations and jetting direction was at 37 μm . At distances around 25 μm the microstreaming and secondary Bjerknes forces were repeatedly intense enough to create a higher incidence of horizontal directional components in the fluid jet. These distances may vary depending on microbubble lipid shell stiffness and ultrasound pressure applied.

The formation of elongated and ellipsoid debris clouds did not appear to be influenced by the size of the microbubble at sizes below 4 μm in diameter. Above 4 μm in diameter the microbubbles all had inter-microbubble distances below 30 μm except for one microbubble that was isolated and had a radial debris cloud. The population subset of microbubbles below 4 μm in diameter shows a statistically significant difference in inter-microbubble distance between those bubbles that formed elongated debris clouds and those that had radial debris clouds ($p < 0.001$) using the same statistical test as described above for comparisons of inter-microbubble distance. However, for this same population of bubbles below 4 μm , there was no statistically

significant difference in bubble size between all three groups ($p = 0.169$). This supports that for microbubbles less than 4 μm in diameter, which is the relevant size range for clinically-used microbubbles, the more dominant factor for formation of horizontal directional components in the jet was the distance between the microbubbles and not their size.

The formation of horizontal directional components in the fluid jet can be a desirable trait because the energy is concentrated into a smaller volume and is directed at more cells, resulting in a longer distance of influence across the capillary wall. It is also more likely to cause extensive capillary ruptures and endothelial cell death which would be beneficial when trying to degrade the endothelium of tumor tissue in an effort to enhance the extravasation of subsequently administered drug or drug delivery vehicles.

Horizontal directional components in the jet could be increased significantly in the tumor region by assuring that the microbubbles are preset in sufficient concentrations so that they would be no more than 25 μm apart from one another. Achieving these high concentrations might require prohibitively high dose administration to the patient. One potential option to overcome this limitation is the incorporation of endothelial targeting agents which help the bubbles to accumulate in closer proximity. Another option is tethering the microbubbles together using ligand binding which would allow them to be pre-coupled prior to administration. Using dilute concentrations of the binding agents followed by a blocking agent would allow for predominantly microbubble dimer formation and prevent microbubbles from cross-linking into larger cluster networks. This would ensure that the microbubbles were

close enough to cause substantial horizontal directional components in the jet similar to the situation shown in Figure 3.3.

Conclusions

The starting distance between microbubbles prior to ultrasound exposure had a significant effect on the shape of the resulting lipid debris cloud. This debris cloud shape was influenced by directional components of the fluid jet resulting from inertial cavitation. In our experimental configuration, inter-microbubble distances greater than 37 μm resulted in jets that were directed straight at the glass interface creating circular debris clouds. This indicates that at this distance the microbubbles were not interacting with one another. At distances less than 37 μm microbubble microstreaming and secondary Bjerknes forces began to influence and distort microbubble oscillations resulting in detectable horizontal directional components creating ellipsoid-shaped debris clouds. At distances less than 10 μm significant elongation of the debris clouds was observed in every instance indicating that a strong horizontal directional component was created in the fluid jet. Microbubbles that were in physical contact with one another exclusively formed these elongated debris clouds. Physically attaching microbubbles together in pairs could help ensure formation of a horizontal directional component in the jet to maximize capillary damage for in-vivo drug delivery applications.

Acknowledgements

Support was provided by Grant Numbers T32 CA121938 and R25 CA153915 from the National Cancer Institute. The content is solely the responsibility of the authors and does not necessarily represent the official views of the National Cancer Institute or the National Institutes of Health.

Chapter 3, in full, has been submitted for publication of the material as it may appear in the Journal of the Acoustical Society of America, 2014, Carolyn Schutt, Stuart Ibsen, William Thrift, Sadik Esener, Acoustical Society of America 2014. The dissertation author was the primary investigator and author of this paper.

Chapter 4

Toward Light-Activated Localized Prodrug Nanoparticle Therapy:
Drug Delivery Nanoparticles formed from Light-Activated Doxorubicin
Prodrug Monomers

Abstract

A major challenge facing nanoparticle-based drug delivery vehicles with chemotherapy payloads is accumulation in healthy tissue through passive extravasation as well as active uptake by the reticulo-endothelial system. These healthy tissues get a dose of the active drug once the nanoparticles begin to break down resulting in dose limiting side effects. To address this issue, we have designed and characterized a new nanoparticle that is entirely comprised of light-activatable prodrug monomers of the chemotherapy agent doxorubicin. Pure doxorubicin was released from the particles only when exposed to 365 nm light. The non-activated prodrug particles had a cellular toxicity that was 30 times less than pure doxorubicin. These nanoparticles are prepared through a reproducible single-step self-assembly process and have an average diameter of around 100 nm. The nanoparticles are made entirely from prodrug monomers and thus achieve the maximum possible prodrug loading capacity since no support structure or coating was required to prevent loss of payload from the nanoparticle. Cellular localization studies showed that prodrug carried by the nanoparticles passed into the cell cytoplasm but did not associate with the nucleus or DNA like pure doxorubicin. Preventing doxorubicin association with the nucleus contributed to the reduced toxicity of the nanoparticle. Exposure to 365 nm light increased the toxicity of the nanoparticle sample to A549 human lung cancer cells by releasing pure doxorubicin which then showed normal bioactivity. The reduced toxicity of these nanoparticles and controllable release of pure doxorubicin with 365 nm light exposure makes these light activated nanoparticles promising for *in*

vivo studies where light emitting diodes can activate the prodrug selectively in the tumor tissue. This could reduce pure doxorubicin concentrations in healthy tissues that actively and passively accumulate the nanoparticles.

Introduction

Cancer is a disease of uncontrolled cellular replication that occurs simultaneously with normal healthy cell replication. Most chemotherapy drugs take advantage of cancer's uncontrolled growth by interfering with some aspect of replication. A main goal for chemotherapy development is to allow systemically distributed drugs to differentiate healthy replication from tumor replication to prevent the dose-limiting side effects experienced by patients.

To address this problem, the field of drug delivery looks to physically encapsulate these drugs in a vehicle which carries its payload systemically through healthy tissue with minimal release. However, these vehicles need to release their payload in the tumor tissue either by preferential accumulation with slow drug release or by a tumor-specific triggering event. An example is FDA-approved Doxil®, the liposomal formulation of the chemotherapy drug doxorubicin (DOX) [117, 129]. Doxil® particles dramatically change the pharmacokinetics and biodistribution [130] of DOX due to their 80-120nm size [53] and polyethylene glycol (PEG) surface coatings. Free DOX has a circulation half-life of 15-20 min [131] while Doxil® has a half-life of 42 hours [53]. The particle size range that allows Doxil® to achieve long circulation times also allows the Doxil® to passively extravasate through

discontinuous endothelium, like that found in the tumor [117]. This allows the systemically circulating particles to pass through tissue with continuous endothelium with minimal accumulation, such as through sensitive heart tissue [41, 132, 133], while preferentially accumulating within the tumor tissue. Once accumulated in the tumor, Doxil® slowly releases the payload through dissolution of the internal crystallized DOX. The majority of the vehicles are eventually cleared from circulation by the liver and the spleen.

Other places in the body naturally have discontinuous endothelium which allows particles of this size to accumulate. Such places include the creases of the hands and feet where it is thought that constant motion causes natural microdamage to the blood vessels allowing Doxil® particles to extravasate [134]. The skin ulcerations and irritation that results from the DOX release in these regions is known as Palmar-plantar erythrodysesthesia and is a major dose-limiting side effect [135].

Doxil® will also accumulate in the bone marrow [136, 137] through the reticulo-endothelial system (RES) [136], and by extravasation [115] due to the bone marrow's discontinuous endothelium [138]. The bone marrow cells have a very high replication rate [139] and are very sensitive to drugs that affect replication. The released payload from these accumulated nanoparticles can cause dose-limiting myelosuppression [135].

This unintentional accumulation of the nanoparticles in the RES and through passive extravasation into healthy tissue is a major concern. There is no particle size window that will avoid extravasation but allow long circulation times [53, 115]. PEG

surface coatings can delay accumulation, especially in the RES, but over time the particles still accumulate in these regions.

The nanoparticles designed in this work address the toxicity from nonspecific and non-targeted accumulation by being comprised entirely of prodrug. Prodrugs are covalently modified versions of the active drug that display significantly reduced toxicity from the original drug but have the ability to be restored to a therapeutic form when triggered. If the trigger is tumor-specific then the nanoparticles can accumulate in the healthy tissue and release prodrug with substantially lower toxic side effects.

The prodrug used here has recently been developed to use a photocleavable linker [140] covalently bound to DOX to render it less toxic to tissue with the unique ability to restore full therapeutic function when photo-triggered [50]. The compound, called DOX-PCB, was created by blocking the free amine located on the sugar moiety with a nitrophenyl group conjugated to a short polyethylene glycol linker and terminated with a biotin (PCB) as seen in Figure 4.1.

Three dimensional modeling of the molecular conformation of DOX-PCB in water using ChemDraw is shown in Figure 4.2. This hairpin shape results from the hydrophobic aglycone structure of DOX interacting with the hydrophobic nitrophenyl group. This gives the molecule a hydrophobic region and a hydrophilic tail region consisting of the PEG linker and biotin. This structure also allows the monomers to self-assemble into nanoparticles, due to the dual hydrophobic/hydrophilic nature of the molecule, upon injection into aqueous solution using a nanoprecipitation process.

The choice of the prodrug trigger that restores the drug to its therapeutic form is critical to assure tumor specificity. The use of light is different from traditional

triggers that rely on the biochemistry of the tumor. These biochemical triggers include differences in the microenvironment between tumor and normal tissue such as tumor-associated hypoxia or low pH [45, 46], as well as enzymatic cleavage by enzymes which the tumor over-expresses [42-44]. The main challenge is that these biochemical triggers are often present in both tumor and normal tissue [48, 49], especially the liver where there is a high level of enzymatic activity.

The light-based trigger can achieve a higher level of specificity than biochemical triggers because the activating wavelength of light can be delivered specifically to the tumor tissue using light emitting diode (LED) technology. Recent developments in LED manufacturing enable elements to be made as thin as a human hair [141] which could allow them to be inserted [51] or implanted anywhere a biopsy needle, endoscope, or catheter can go. The photocleavable linker in DOX-PCB is resistant to metabolic degradation which prevents undesired activation of the prodrug in healthy tissue regions, including the liver [50, 142], but is activated by exposure to 365 nm light. This wavelength showed low absorption by internal tissue [143] including DNA [144] but had high absorption by melanin [145] preventing external sources from causing uncontrolled release within the body.

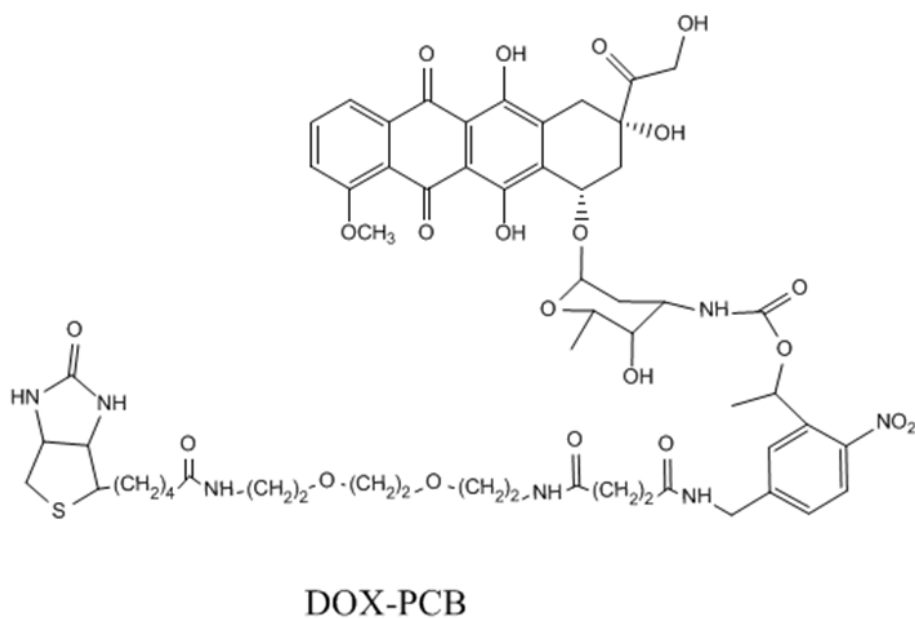


Figure 4.1 Molecular structure of DOX-PCB. The DOX molecule is attached to a photocleavable nitrophenyl compound that has a short polyethylene glycol linker attached to a biotin molecule at the opposite end.

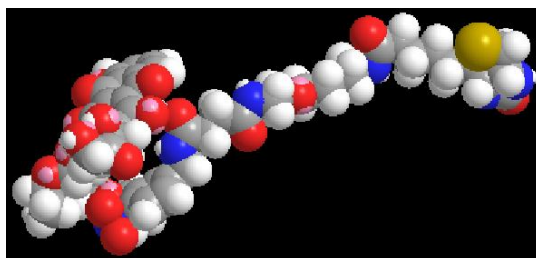


Figure 4.2 Three dimensional conformation of the DOX-PCB prodrug monomer.

Materials and Methods

Materials

Doxorubicin hydrochloride (DOX) was purchased from Qventas (Branford, CT) and Sigma (St. Louis, MO). Water soluble photocleavable biotin–NHS (PCB) was purchased from Ambergen (Watertown, MA). High pressure liquid chromatography (HPLC) grade acetonitrile was purchased from Fisher Scientific (Fairlawn, NJ). The human lung cancer cell line A549 was purchased from the American Type Culture Collection (Manassas, VA). Dulbecco’s Modified Eagle Medium (DMEM) cell culture media and trypsin-EDTA (ethylenediaminetetraacetic acid) for cell culture were purchased from Mediatech, Inc. (Manassas, VA). The penicillin-streptomycin used as a media supplement and the DMEM media without phenol red were purchased from Gibco (Invitrogen, Grand Island, NY). Fetal bovine serum used as a supplement in the DMEM media was purchased from Hyclone (Logan, UT). Dulbecco’s phosphate buffered saline (DPBS) was purchased from Hyclone Laboratories Inc. (Logan, UT). All water was purified using the Milli-Q purification system from Millipore Corporation (Billerica, MA). XTT was purchased from Sigma (St. Louis, MO).

DOX-PCB Nanoparticle Synthesis

The DOX-PCB monomers were synthesized using the procedure described in Ibsen et al. [50]. To form nanoparticles from the DOX-PCB prodrug, a single-step nanoprecipitation method was used. The DOX-PCB monomer was first dissolved in

acetonitrile at a concentration of 0.1 mg/ml. A 168 μ l volume of this solution was aspirated into a 1 ml syringe fitted with a 30 gauge 1 inch needle, and then added dropwise to 2 ml of ultrapure water under vortex. The hydrophobic ends of the prodrug molecules clustered together to form particles in order to minimize contact with the water. The resulting sample was stirred gently for 48 hours at room temperature while open to the atmosphere to evaporate the acetonitrile. This evaporation was performed to help ensure the stability of the nanoparticles and the biocompatibility of the sample. The sample was protected from ambient light during the stirring process.

The particles were then concentrated using a centrifugal evaporator to remove the desired amount of water. The particles did not aggregate as they were concentrated under the centrifugal force. Care was taken to ensure the evaporation rate did not result in the freezing of the water. DOX-PCB concentration was measured through light absorption using a Nanodrop ND-1000 spectrophotometer (Thermo Fisher Scientific, Waltham, MA). All DOX-PCB nanoparticle solution concentrations are given in terms of DOX-PCB molecule content.

Particle Characterization

The DOX-PCB nanoparticles were characterized using three different methods. The size distribution of the particles was first evaluated by the Nanoparticle Tracking Analysis (NTA) technique using a NanoSight LM10 system (NanoSight Ltd., Amesbury, UK) at room temperature. Two samples of 300 μ l volume were introduced into the viewing unit for the particles to be tracked and sized on a particle-by-particle

basis using the NTA technique. Size is reported as the average of the peak value of the size distribution from each sample. A video clip of the particles' Brownian motion was also acquired using the NanoSight system.

The size results acquired by NTA were confirmed using a Zetasizer Nano-ZS dynamic light scattering (DLS) system (Malvern Instruments, Worcestershire, UK) at room temperature with backscattering angle of 173°. Size measurements were obtained in triplicate along with polydispersity indices. Zeta potential measurements were also acquired in triplicate using this instrument.

Finally the surface and shape morphology of the nanoparticles were evaluated using scanning electron microscopy (SEM) with a Phillips XL30 SEM system. The manufactured nanoparticle sample was diluted on the order of 10,000 times from its original concentration to allow observation of individual particles. A 2 µl sample of the diluted sample was placed on the surface of a polished silicon wafer fragment and allowed to dry at room temperature overnight. The sample was coated with chromium and then imaged.

Light Activated Drug Release Characterization

The nanoparticle samples were evaluated for their release of pure DOX after receiving various amounts of 365 nm light exposure. Samples of 10 µl of DOX-PCB nanoparticles at 31 µM were placed into individual wells in a 96-well flat bottom assay plate (BD Biosciences, San Jose, CA) with opaque black walls and a clear bottom. The black walls helped to prevent reflections of 365 nm light inside the well and ensure uniformity of exposure between samples. The clear lid of the plate was

fitted on top to help reduce the evaporation rate of the water. The samples were exposed to 2.3 mW/cm^2 of light from a Mercury Short Arc HBO bulb from OSRAM (München, Germany) with a 330–380 nm bandpass filter for increasing durations of time from 0 to 60 min. This measured light intensity took into account the absorption of 365 nm light by the lid. The samples were then collected and their volumes adjusted with water to 10 μl if any evaporation occurred.

In an in-vivo application, the DOX that was released from the nanoparticles would immediately diffuse away from the particle and associate with plasma proteins, cellular proteins, and DNA. In the specific case of this experiment the DOX-PCB nanoparticles were suspended at a high concentration in pure water which could allow the free DOX released from the particles to immediately associate with other particles. To help prevent DOX from being sequestered into other particles, the 365 nm light exposed samples were then mixed with dimethyl sulfoxide (DMSO) in a 0.2/1 v/v ratio. The samples were then bath sonicated for 5 min. The presence of DMSO in the sample helped to keep the released DOX in solution so that it could be quantified by LC-MS/MS.

The DOX content of the samples was then quantified by LC-MS/MS using an Agilent 1260 liquid chromatograph (LC) system coupled with a Thermo LCQdeca mass spectrometer (MS). The LC-MS/MS analysis used positive ion mode electrospray ionization (ESI) as the ion source with source voltage of 5 kV, capillary temperature of 250°C , auxiliary gas flow rate of 20 units, and sheath gas flow rate of 80 units. A CAPCELL MG III C-18 column (Catalog number 92744, ID $2.0\text{mm} \times$ length 50 mm, particle size 3 μm) was used (with guard column) for LC separation.

The mobile phase A was 5% methanol in water with 0.1% formic acid. The mobile phase B was pure methanol with 0.1% formic acid. The LC gradient was increased from 30% mobile phase B to 95% mobile phase B in a duration of 10 minutes, then held at 95% B for 5 minutes, brought back to 30% B in 1 minute, and then held at 30% B for 6 minutes. The LC flow rate was held at 0.20 ml/min. Using these LC conditions, the DOX and the two isomers of DOX-PCB were separately eluted from the LC column with a retention time of about 9.8 minutes for DOX, and about 13.2 and 13.7 minutes for the two isomers of DOX-PCB. DOX had a molecular ion peak at m/z 544 ($[M+H]^+$). Under positive ion mode ESI-MS/MS analysis, a major fragment peak of DOX was seen at m/z 396.8 with a normalized collision energy of 30%. Both of the DOX-PCB isomers had molecular ion peaks at m/z 1244.4 ($[M+Na]^+$). Under positive ion mode, the ESI-MS/MS analysis showed a major fragment peak ($[M+Na]^+$) at m/z 848.3 with a normalized collision energy of 35%. Selected reaction monitoring (SRM) mode was used to acquire the m/z 396.8 fragment ion peak which were used for quantification of the DOX.

Cellular Localization

The intracellular localization of the DOX-PCB nanoparticles and pure DOX was studied using the PTK2 epithelial cell line. These cells were used because they are susceptible to DOX and remain flat during mitosis, allowing for enhanced visualization of the nuclear region. This visualization capability was important since one of the main therapeutic modes of action for DOX is through DNA intercalation. The DOX-PCB nanoparticles and pure DOX are both naturally fluorescent which

allowed them to be easily tracked through the cell. The PTK2 cells were plated in glass bottom petri dishes (MatTek Corporation, Ashland, MA) and were incubated in advanced MEM Media from Gibco (Invitrogen, Grand Island, NY) with 2% fetal bovine serum, nonessential amino acids, 110 mg/L sodium pyruvate, and without penicillin-streptomycin or L-Glutamine.

A 1 ml media solution of DOX-PCB nanoparticles was prepared by first adding 10x DPBS to a 4.1 μM solution of DOX-PCB nanoparticles in water to achieve a 1x DPBS concentration, and then adding the resulting solution to a phenol-red free formulation of the advanced MEM media described above to achieve a final DOX-PCB content of 2 μM . This spiked media sample was then added to the glass bottom petri dish along with PTK2 cells seeded which had the previous incubation media removed. A 1 ml media solution of 2 μM DOX was prepared in the same manner with the DPBS content matched to the above nanoparticle solution, and the DOX media solution was exposed to the cells in the same manner as described above. The cells were incubated with the spiked media samples for 2 hours. Live fluorescent images of the cells were obtained using a Zeiss Axiovert 200 M Microscope (Zeiss, Thornwood, NY) using an HCred1 rhodamine filter cube from Chroma (Rockingham, VT, USA) and a 63x phase III, NA 1.4 oil immersion objective. All microscope control and imaging utilized the RoboLase system [146].

To study the change in cellular localization after activation, the cells incubated with the DOX-PCB nanoparticles were exposed to the 365 nm light source for 60 seconds. The cells were then allowed to incubate in the 365 nm light-exposed media for 1 hour. The cells were reanalyzed using the microscopy system described above.

The RoboLase system allowed the same cells that were imaged before 365 nm light exposure to be relocated and imaged again after 365 nm light exposure.

Cytotoxicity

An IC₅₀ study was conducted to determine the toxicity of the DOX-PCB nanoparticles before and after 365 nm light exposure relative to free DOX using the human lung cancer cell line A549 which was purchased from the American Type Culture Collection (ATCC) (Manassas, VA, USA). The cells were grown on sodium pyruvate-free DMEM media containing L-glutamine, 4.5 g/L of glucose, penicillin-streptomycin and 10% Fetal Bovine Serum. The adherent cells in the expansion flask were detached using Trypsin (.25% T / 2.21 mM EDTA) and plated onto a 96-well plate at a density of 10⁴ cells per well in 100 μL of media. The cells were incubated at 37°C overnight to allow them to adhere to the bottom of the well.

Experiments were run in two replicates under three different conditions. The first condition was incubation with pure DOX, the second was incubation with DOX-PCB nanoparticles with no 365 nm light exposure, and the third was incubation with DOX-PCB nanoparticles that had previously been exposed to 60 min of 365 nm light from the same light source used in the light-activated drug release characterization study.

The spiked media samples were prepared ahead of time using stock solutions of 200 μM DOX and 200 μM DOX-PCB nanoparticles in water. A sample of the pure DMEM media described above was concentrated to 80% of the original volume. The concentrated media was rediluted to its original volume using the stock solutions of

drug to achieve solutions of DOX and DOX-PCB nanoparticles at 13.3 μM in the media. A 1/3 serial dilution was then performed to create concentrations that ranged from 13.3 μM to 2.0 nM. The 80% volume concentrated media rediluted to 100% volume with pure sterile water with no drug added was used as the control for each condition. The incubation media in each well was then replaced with the above prepared solutions causing minimal disturbance to the cells. The cells were allowed to incubate at 37°C for 72 h.

At 72 hours, the In Vitro Toxicology Assay Kit (TOX2) from Sigma Aldrich was used to perform an XTT cell viability assay. Phenol red free DMEM Media containing 10% Fetal Bovine Serum and penicillin-streptomycin from Gibco was used for the XTT assay to prevent phenol red interference with the absorption measurements. After 30 min of incubation time, the absorbance of each well was measured using a Tecan Infinite M200 plate reader (San Jose, CA, USA). The collected absorbance values were used to create percent viability vs. dose curves with the PRISM 4.0 program from GraphPad Software Inc. (La Jolla, CA, USA) using the sigmoidal dose-response (variable slope) curve fit.

Results

Particle Characterization

Nanoparticles were reproducibly formed via nanoprecipitation of the DOX-PCB prodrug monomer. Size results obtained from Dynamic Light Scattering (DLS) showed that the DOX-PCB nanoparticles had a unimodal size distribution with an

average diameter of 102.5 ± 1.6 nm as shown in Table 4.1. Size results obtained from Nanoparticle Tracking Analysis (NTA, Table 4.1) confirmed the nanoparticle size at around 100 nm in diameter. Zeta potential was measured at -41.6 ± 3.6 mV, which supports that the nanoparticles have sufficient repulsive interactions to be stably monodispersed in solution. Scanning electron microscope images of the particles are shown in Figure 4.3. The particles are spherical in shape with a size range that appears slightly smaller than the results obtained by DLS and NTA, which may be an effect of the nanoparticle drying preparation used for SEM. The particles maintained a stable size in water at 4°C for over 6 months. The DOX-PCB nanoparticles were able to be concentrated to at least 0.22 mg/ml without aggregation indicating that the monomers on the outer layer of the nanoparticle most likely oriented themselves such that the PEG chain interfaced with the water and prevented hydrophobic interactions between particles and subsequent aggregation.

Table 4.1 Characterization of DOX-PCB nanoparticle size and zeta potential (mean \pm standard deviation).

Diameter by DLS (nm)	Polydispersity Index	Diameter by NTA (nm)	Zeta Potential (mV)
102.5 ± 1.6	0.120 ± 0.012	96.5 ± 6.4	-41.6 ± 3.6

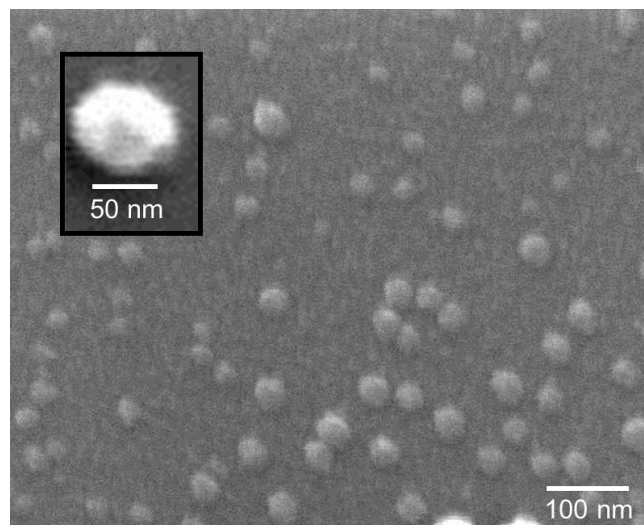


Figure 4.3 Scanning electron microscope image of the DOX-PCB nanoparticles produced by the nanoprecipitation process of the DOX-PCB monomer. The wide field view shows the uniformity of the nanoparticle structures. Inset: SEM image of a single DOX-PCB nanoparticle.

Light-Activated Drug Release Characterization

The DOX activation and release profile with 365nm light exposure time is shown in Figure 4.4. It can be seen that a linear relationship existed between the dose of 365 nm light and the amount of released DOX ($R^2 = .93$). A higher dose of 365 nm light, either in intensity or duration, would result in higher amounts of released DOX.

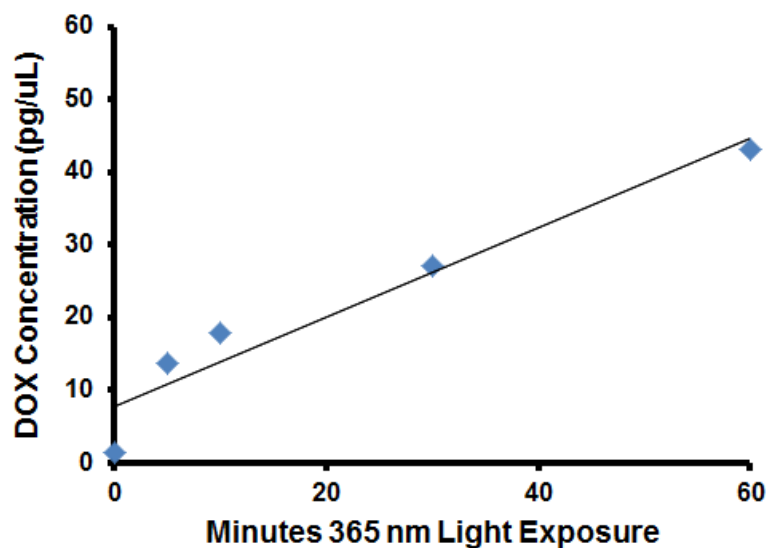


Figure 4.4 The concentration of released DOX from the DOX-PCB nanoparticles increased linearly with the duration of 365 nm light exposure ($R^2 = .93$).

Cellular Localization

The localization of free DOX and the DOX-PCB nanoparticles in the PTK2 kidney epithelial cell line is shown in Figure 4.5. Both DOX and DOX-PCB are inherently fluorescent allowing them to be tracked within a cell. The PTK2 cells were chosen due to their unique tendency to remain flat during replication improving the ability to image the nuclear region and determine cellular localization. One of the known modes of therapeutic action of pure DOX is as a DNA intercalator [147] and it has also been observed to have therapeutic effect through interactions with DNA polymerase I and topoisomerase II. Free DOX is seen to strongly associate with the cell nuclei as seen in panel 1B. Prior to 365 nm light exposure, the DOX-PCB in the nanoparticles can be seen in the cell cytoplasm. The cell nuclei do not show any

significant fluorescent signal prior to 365 nm light exposure. After exposure to the 365 nm light, the nuclei of the cells show increased fluorescence supporting that the DOX released from the nanoparticles was behaving as therapeutically expected and associating with the nuclear region.

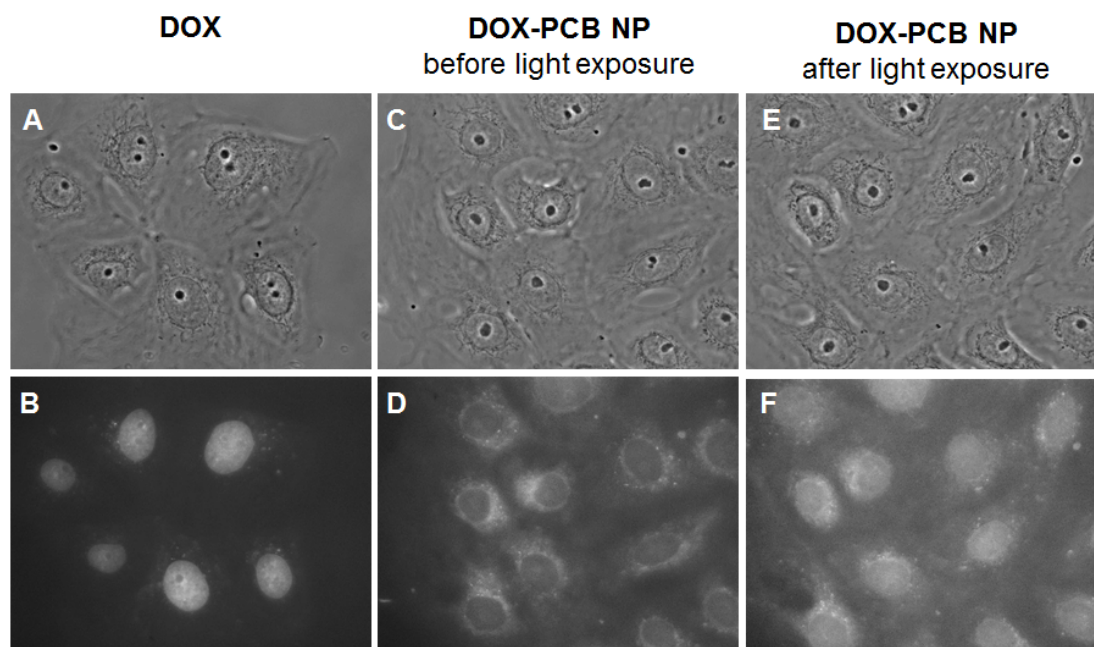


Figure 4.5 Light microscopy images of DOX and DOX-PCB nanoparticle localization within live PTK2 kidney epithelial cells. Panels A, C, and E are phase contrast images of the cells and panels B, D, and F are fluorescent images of the same field of view as the panel directly above. Panels C, D, E, and F show the same group of cells before and after 365 nm light exposure. (A, B) DOX is seen to associate strongly with the cell nuclei. (C, D) DOX-PCB entered the cells but did not associate with the nuclei prior to 365 nm light exposure. (E, F) After 365 nm light exposure, the nuclei show increased fluorescence supporting that free DOX was released from DOX-PCB.

Cytotoxicity

The IC₅₀ data for A549 human lung cancer cells is shown in Figure 4.6. The nanoparticles show a reduction in toxicity of 30 times compared to pure DOX. Upon exposure to 365 nm light pure DOX was released from the nanoparticles resulting in a reduction of the IC₅₀.

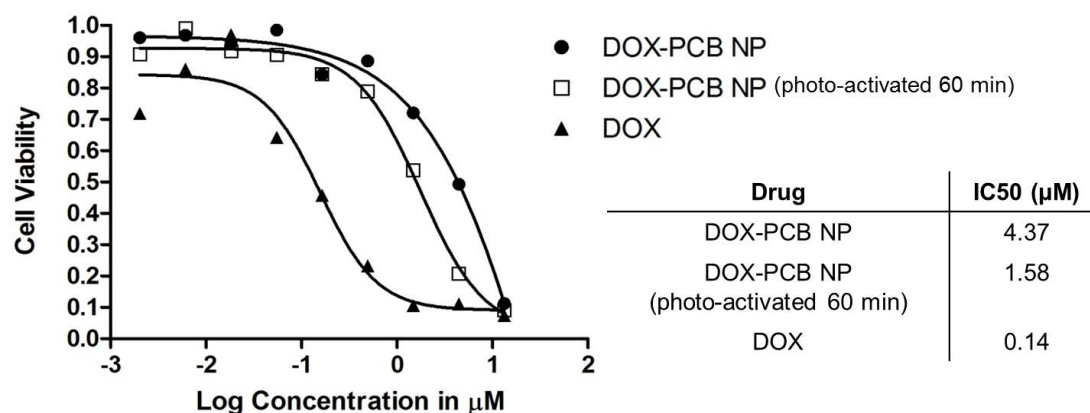


Figure 4.6 Cell toxicity results on human lung cancer cells of DOX-PCB prodrug nanoparticles, photoactivated DOX-PCB nanoparticles and free DOX. DOX-PCB prodrug nanoparticles show significantly reduced toxicity from free DOX, with DOX-PCB yielding a 30-fold higher IC₅₀ value (drug concentration at which cellular viability was reduced by 50%). The DOX-PCB nanoparticles that were photo-activated for 60 minutes displayed an increased cellular toxicity compared to unexposed DOX-PCB nanoparticles.

Discussion

Nanoparticles of light-activatable prodrug monomer were successfully fabricated using a single-step nanoprecipitation process. The self-assembly method is reproducible and relatively simple, giving it strong potential for future scale-up. These spherical nanoparticles of around 100 nm in diameter were formed using only the light-activatable prodrug monomer without the need for any support scaffolding. This maximized the payload capacity by utilizing the entire volume of the nanoparticle to carry prodrug. This is different from most other nanoparticle designs that require a scaffolding or structural barrier to contain the drug payload. These structural components take up valuable volume inside the nanoparticle which reduces the amount of payload that can be loaded. The particles described here have a near-100% loading efficiency of the prodrug as determined by high pressure liquid chromatography showing very low quantities ($< 2\%$) of DOX-PCB left in the supernatant after the nanoparticles were removed from the solution through filtration.

The DOX-PCB nanoparticles displayed a 30-fold reduction in cellular toxicity prior to activation as compared to pure DOX. The fluorescent DOX-PCB was found in the cytoplasm of the PTK2 cells but not in the nuclear DNA as shown in Figure 4.5. The lack of fluorescent signal in the nucleus before 365 nm light exposure supports that the delivered DOX-PCB prodrug did not have any DNA interactions such as intercalation. This could partially account for the reduction in the toxicity of the DOX-PCB nanoparticles compared to free DOX. It is unknown if the DOX-PCB was in

monomer form or in nanoparticle form inside the PTK2 cells because the 100 nm diameter particles were not resolvable with the microscopy system. Future studies will determine if the cells endocytose the nanoparticles with subsequent dissolution to monomer form or if the nanoparticles stay intact within the cell.

Pure DOX was released from the nanoparticles in a linear relation with the amount of 365 nm light exposure. The increase in fluorescence of the nucleus of the PTK2 cells after 365 nm light exposure supports that the released DOX was bioavailable and had fully toxic DNA intercalation properties. This DNA intercalation would account for the sample's observed increase in cellular toxicity. The percentage of DOX-PCB monomers that convert to pure DOX can be increased by using higher power LED light sources or by increasing the exposure time. The release of more DOX increases the cellular toxicity of the DOX-PCB nanoparticle sample and would result in a further reduction of the IC50.

The size and surface characteristics of the DOX-PCB nanoparticles are similar to Doxil® and it is likely that these particles would accumulate both in the tumor and in specific sites of healthy tissue including the bone marrow in a similar manner to Doxil®. However, in the case of DOX-PCB nanoparticles, pure DOX would only be released inside the 365 nm light-exposed tumor tissue. By adjusting the intensity of the 365 nm light the DOX release rate can be tailored to match that of Doxil® or could be increased to make DOX bioavailable at faster rates. The reduced toxicity of the DOX-PCB nanoparticle compared to free DOX could result in significantly reduced bone marrow toxicity as well as reduced skin ulcerations in the hands and feet which would significantly improve patient quality of life during treatment.

Conclusions

The proof of concept work described here demonstrates the ability to form nanoparticles self-assembled entirely from light-activated prodrug monomers. These particles have an average diameter of about 100 nm and feature PEG interfacing between the bulk of the particle and the water. The DOX-PCB prodrug nanoparticles did not show any evidence of DOX interaction with cellular DNA. These particles were shown to be 30 times less toxic to A549 human lung cancer cells compared to pure DOX. Upon exposure to 365 nm light, pure DOX was released from the nanoparticles with a linear dose response. The released DOX was shown to be bioavailable increasing the toxicity of the sample. The stability and size properties of the DOX-PCB nanoparticles along with the ability to release DOX when exposed to 365 nm light make these particles promising for future *in vivo* studies on tumor localized drug delivery.

Acknowledgements

Support was provided by Grant Numbers T32 CA121938, R25 CA153915, and 5 U54 CA119335 from the National Cancer Institute. The content is solely the responsibility of the authors and does not necessarily represent the official views of the National Cancer Institute or the National Institutes of Health. The authors also

wish to thank Dr. Yongxuan Su and the Molecular Mass Spectrometry Facility at the University of California San Diego Department of Chemistry and Biochemistry for their work with the mass spectrometry analysis.

Chapter 4, in full, is currently being prepared for submission for publication of the material. Carolyn Schutt, Stuart Ibsen, Eran Zahavy, Santosh Aryal, Michael Berns, Sadik Esener. The dissertation author was the primary investigator and author of this material.

Dissertation Conclusions

This dissertation develops and demonstrates the initial feasibility of a new localized tumor detection technique using acousto-fluorescence contrast agents. This dissertation additionally investigates two localized drug delivery strategies using microbubbles to potentially enhance extravasation and developing a new light-activated prodrug nanoparticle.

Acousto-Fluorescent Contrast Agent Development

The thermal treatment techniques used on the microbubble contrast agent were able to evenly distribute the fluorescent dye over the surface of the microbubble. The heating portion of the treatment raised the lipids in the monolayer above their melting point allowing Brownian motion to mix the different species including the lipophilic dye. The rapid-cooling phase of the treatment was able to solidify the lipids into place preserving the homogeneous distribution. The slower cooling rates investigated allowed the lipid to once again partition into isolated islands before eventual solidification. The homogeneous distribution allowed the dye molecules to separate sufficiently from one another during the microbubble expansion phase to change their self-quenching efficiency resulting in a significant ten-fold increase in detectable fluorescence intensity modulations.

This thermally-induced change in the microbubble surface nanostructure improved the surface dye self-quenching efficiency to the extent that higher harmonic

fluorescence intensity modulations were now detectable in addition to the fundamental frequency. These harmonic fluorescence modulations had not previously been observed and open the possibility of using the higher harmonic signals to further increase the signal to noise ratio of detected fluorescence modulation signals.

Acousto-Fluorescent Contrast Agent Detection

The fluorescence modulated signal generated at the fundamental frequency by the contrast agent microbubbles was detected for the first time in a scattering media environment. This was achieved through the use of a lock-in amplifier and was enabled by the consistent generation of a modulated-fluorescence signal of detectable amplitude made possible by the microbubble rapid-cooling technique developed in this dissertation. The signal to noise ratio of the modulated fluorescence signal was higher than the signal to noise ratio of the modulated scattering signal. The scattered light modulation signal of the microbubbles was lost in the bulk scattering of the media whereas the production of the fluorescence modulation was independent of scattering and was less affected.

Investigation of Inter-microbubble Distance on Fluid Jet Direction

The distance between microbubbles prior to ultrasound exposure was shown to have a significant effect on the shape of the resulting lipid debris cloud. This debris cloud shape was influenced by directional components of the fluid jet resulting from inertial cavitation. In our experimental configuration, inter-microbubble distances greater than 37 μm resulted in jets that were directed straight at the glass interface

creating circular debris clouds and supporting that at this distance the microbubbles were not interacting with one another. At distances less than 37 μm microbubble microstreaming and secondary Bjerknes forces began to influence and distort microbubble oscillations resulting in detectable horizontal directional components creating ellipsoid-shaped debris clouds. At distances less than 10 μm significant elongation of the debris clouds was observed in every instance indicating a strong horizontal directional component was created in the fluid jet. Microbubbles that were in physical contact with one another exclusively formed these elongated debris clouds. Physically attaching microbubbles together in pairs could help ensure formation of a horizontal directional component in the jet to maximize capillary damage for in-vivo drug delivery applications.

Photoactivatable Chemotherapy Prodrug Nanoparticles

The DOX-PCB chemotherapy prodrug monomers were successfully nanoprecipitated into stable, monodispersed nanoparticles with a diameter of about 100 nm. No other components were required to create the nanoparticles or to serve as structural scaffolding. These particles were shown to be 30 times less toxic to A549 human lung cancer cells compared to pure DOX. Upon exposure to 365 nm light, pure DOX was released from the nanoparticles with a linear dose response and was shown to be bioavailable and to have normal DNA intercalation properties. The stability and size properties of the DOX-PCB nanoparticles along with the ability to release DOX when exposed to 365 nm light make these particles promising for future *in vivo* studies on tumor localized drug delivery.

Dissertation Future Directions

Future work with the ultrasound-modulated fluorescent microbubbles will incorporate near-infrared lipophilic fluorophores into the microbubble shell. The near-infrared wavelengths are better able to penetrate through tissue and will allow more of the generated fluorescent photons to exit the tissue and reach the detector. Additional work will also be aimed at incorporating chemically-sensitive dyes into the microbubble that allow for detection of the chemical tumor microenvironment. Potential dyes for incorporation include ruthenium-(II) based dyes which show oxygen-responsive fluorescence quenching [90, 148] and could be investigated for use in the detection of hypoxia.

Another future adaptation of the blinking microbubble design will be to incorporate a chemiluminescent or bioluminescent agent such as luciferase, along with a quencher particle, onto the microbubble surface. The luciferase would be used in place of a traditional fluorescence dye that requires light excitation. Luciferase substrate would need to be provided in sufficient concentration for light emission. Use of the chemiluminescent dye will help to increase the signal to noise ratio because there will no longer be any excitation light flooding the tissue. The only detectable light will be from microbubbles directly within the focal zone of the ultrasound. In order to produce a near-infrared emission from this bubble design for enhanced tissue penetration, the luciferase could be pre-conjugated to a near-infrared dye at the resonance energy transfer distance prior to incorporation on the luciferase-dye pair on the microbubble surface.

Future work involving the harmonic fluorescent modulation signals will investigate using the lock-in amplifier to detect these signals from within scattering media. A potential issue for harmonic detection is that the lower incidence of higher harmonic signals may not provide signals of long enough duration for the lock-in amplifier to extract. Future work will be needed to investigate the ability of the feasibility of this detection approach.

Future work in the area of ultrasound-induced fluid jet formation for microcapillary damage will look at tethering the microbubbles together in pairs at distances close enough to promote the formation of horizontally-directed fluid jets. These horizontally-directed jets would affect a larger surface area of the target capillary. The microbubble pairs can be created through ligand binding using dilute concentrations of the binding agent to allow for predominantly microbubble dimer formation.

Future work with the light-activatable chemotherapy prodrug nanoparticles will look to evaluate their long-term circulation capabilities. Future development will involve synthesis of a nanoparticle that coats the outside surface of the DOX-PCB nanoparticle with a lipid and pegylated lipid membrane layer. This lipid layer may allow for enhanced circulation time and biostability. Different targeting ligands can be incorporated into the surface of the nanoparticles to help them accumulate in the tumor tissue. Future work will also focus on designing a long-term implantable version of the activating LED so the activating light can be delivered to the tumor tissue for an extended duration in clinical settings.

As development of both localized detection and localized therapy strategies continues in parallel, ensuing studies can look at the ability to use these strategies in concert. Investigations will be directed toward the eventual goal of using the localized light-activated chemotherapy in spatially localized tumor regions detected through use of the fluorescence modulating microbubble contrast agents. Ultrasound-induced damage directed along the tumor capillary wall could be used to further enhance the localized accumulation of chemotherapy prodrug nanoparticles prior to light activation.

References

1. Richards MA, Westcombe AM, Love SB, Littlejohns P, Ramirez AJ. Influence of delay on survival in patients with breast cancer: a systematic review. *The Lancet* 1999;353(9159):1119-1126.
2. Metzger ML, Dome JS. Current Therapy for Wilms' Tumor. *The Oncologist* 2005;10(10):815-826.
3. Cohen LS, Escobar PF, Scharm C, Glimco B, Fishman DA. Three-dimensional power Doppler ultrasound improves the diagnostic accuracy for ovarian cancer prediction. *Gynecologic oncology* 2001;82(1):40-48.
4. Halpern EJ, Verkh L, Forsberg F, Gomella LG, Mattrey RF, Goldberg BB. Initial experience with contrast-enhanced sonography of the prostate. *American Journal of Roentgenology* 2000;174(6):1575-1580.
5. Albrecht T, Mattrey RF. 31 Tumor Imaging with Ultrasound Contrast. *Trends in Contrast Media* 1999:367.
6. Miao H, Fukatsu H, Ishigaki T. Prostate cancer detection with 3-T MRI: comparison of diffusion-weighted and T2-weighted imaging. *European journal of radiology* 2007;61(2):297-302.
7. Johnson JO, Mattrey RF, Phillipson J. Differentiation of seminomatous from nonseminomatous testicular tumors with MR imaging. *AJR American journal of roentgenology* 1990;154(3):539-543.
8. Decyk M, Mattrey R. MRI and Ultrasound Imaging of Lymph Nodes. *From Local Invasion to Metastatic Cancer: Springer, 2009.* p. 115-122.
9. Pastorino U, Bellomi M, Landoni C, De Fiori E, Arnaldi P, Picchio M, et al. Early lung-cancer detection with spiral CT and positron emission tomography in heavy smokers: 2-year results. *The Lancet* 2003;362(9384):593-597.
10. Pisano ED, Gatsonis C, Hendrick E, Yaffe M, Baum JK, Acharyya S, et al. Diagnostic performance of digital versus film mammography for breast-cancer screening. *New England Journal of Medicine* 2005;353(17):1773-1783.
11. Rosenberg RD, Yankaskas BC, Abraham LA, Sickles EA, D. LC, M. GB, et al. Performance benchmarks for screening mammography. *Radiology* 2006;241(1):55-66.

12. Janssen HL, Haustermans KM, Balm AJ, Begg AC. Hypoxia in head and neck cancer: how much, how important? *Head Neck* 2005;27(7):622-638.
13. van Veen RL, Amelink A, Menke-Pluymers M, van der Pol C, Sterenberg HJ. Optical biopsy of breast tissue using differential path-length spectroscopy. *Phys Med Biol* 2005;50(11):2573-2581.
14. Vaupel P, Schlenger K, Knoop C, Hockel M. Oxygenation of human tumors: evaluation of tissue oxygen distribution in breast cancers by computerized O₂ tension measurements. *Cancer Res* 1991;51(12):3316-3322.
15. Intes X, Djeziri S, Ichalalene Z, Mincu N, Wang Y, St-Jean P, et al. Time-domain optical mammography SoftScan: Initial results. *Academic Radiol* 2005;12(10):1355
16. Tromberg BJ, Shah N, Lanning R, Cerussi A, Espinoza J, Pham T, et al. Noninvasive in vivo characterization of breast tumors using photon migration spectroscopy. *Neoplasia* 2000;2(1):26-40.
17. Peters VG, Wyman DR, Patterson MS, Frank GL. Optical properties of normal and diseased human breast tissues in the visible and near infrared. *Physics in medicine and biology* 1990;35(9):1317.
18. Zanelli CI, DeMarta S, Hennige CW, Kadri MM. Beamforming for Therapy with High Intensity Focused Ultrasound (HIFU) Using Quantitative Schlieren. *IEEE Ultrasonics Symposium* 1993:1233-1238.
19. Bloch SH, Wan M, Dayton PA, Ferrara KW. Optical observation of lipid-and polymer-shelled ultrasound microbubble contrast agents. *Applied physics letters* 2004;84(4):631-633.
20. Chin CT, Lancée C, Borsboom J, Mastik F, Frijlink ME, de Jong N, et al. Brandaris 128: A digital 25 million frames per second camera with 128 highly sensitive frames. *Review of scientific instruments* 2003;74(12):5026-5034.
21. Chomas JE, Dayton P, May D, Ferrara K. Threshold of fragmentation for ultrasonic contrast agents. *Journal of biomedical optics* 2001;6(2):141-150.
22. Postema M, van Wamel A, Folkert J, de Jong N. High-speed photography during ultrasound illustrates potential therapeutic applications of microbubbles. *Medical physics* 2005;32:3707.
23. Schutt CE, Benchimol MJ, Hsu MJ, Esener SC. Ultrasound-modulated fluorescent contrast agent for optical imaging through turbid media. *SPIE*

- Optical Engineering+ Applications; 2011: International Society for Optics and Photonics; 2011. p. 81650B-81650B-81657.
24. Benchimol MJ, Hsu MJ, Schutt CE, Hall DJ, Mattrey RF, Esener SC. Phospholipid/carbocyanine dye-shelled microbubbles as ultrasound-modulated fluorescent contrast agents. *Soft Matter* 2013;9:2384–2388.
 25. Tannock I. Cell kinetics and chemotherapy: a critical review. *Cancer treatment reports* 1978;62(8):1117-1133.
 26. Straus DJ, Wong GY, Liu J, Oppenberg J, Filippa DA, Gold JWM, et al. Small non-cleaved-cell lymphoma (undifferentiated lymphoma, Burkitt's type) in American adults: results with treatment designed for acute lymphoblastic leukemia. *The American journal of medicine* 1991;90(1):328-337.
 27. Tomlinson IPM, Novelli MR, Bodmer WF. The mutation rate and cancer. *Proceedings of the National Academy of Sciences* 1996;93(25):14800-14803.
 28. Hanahan D, Folkman J. Patterns and emerging mechanisms of the angiogenic switch during tumorigenesis. *cell* 1996;86(3):353-364.
 29. Folkman J. What is the evidence that tumors are angiogenesis dependent? *Journal of the National Cancer Institute* 1990;82(1):4-7.
 30. Demetri GD, Cesne AL, Chawla SP, Brodowicz T, Maki RG, Bach BA, et al. First-line treatment of metastatic or locally advanced unresectable soft tissue sarcomas with conatumumab in combination with doxorubicin or doxorubicin alone: A Phase I/II open-label and double-blind study. *European Journal of Cancer* 2012;Online.
 31. Wood AJJ, Shapiro CL, Recht A. Side effects of adjuvant treatment of breast cancer. *New England Journal of Medicine* 2001;344(26):1997-2008.
 32. Singal PK, Iliskovic N. Doxorubicin-induced cardiomyopathy. *New England Journal of Medicine* 1998;339(13):900-905.
 33. Skyba DM, Price RJ, Linka AZ, Skalak TC, Kaul S. Direct in vivo visualization of intravascular destruction of microbubbles by ultrasound and its local effects on tissue. *Circulation* 1998;98(4):290-293.
 34. Stieger SM, Caskey CF, Adamson RH, Qin S, Curry F-RE, Wisner ER, et al. Enhancement of vascular permeability with low-frequency contrast-enhanced ultrasound in the chorioallantoic membrane model. *Radiology* 2007;243(1):112-121.

35. Jain RK. Normalization of tumor vasculature: an emerging concept in antiangiogenic therapy. *Science* 2005;307(5706):58-62.
36. Vogel A, Lauterborn W, Timm R. Optical and acoustic investigations of the dynamics of laser-produced cavitation bubbles near a solid boundary. *Journal of Fluid Mechanics* 1989;206(1):299-338.
37. Lauterborn W, Kurz T. Physics of bubble oscillations. *Reports on Progress in Physics* 2010;73(10):106501.
38. Kodama T, Tomita Y. Cavitation bubble behavior and bubble–shock wave interaction near a gelatin surface as a study of in vivo bubble dynamics. *Applied Physics B* 2000;70(1):139-149.
39. Denny WA. Prodrug strategies in cancer therapy. *Eur J Med Chem* 2001;36:577-595.
40. Denny WA. Tumor-activated Prodrugs—A New Approach to Cancer Therapy. *Cancer Investigation* 2004;22(4):604-619.
41. Giorgio Minotti PM, Emanuela Salvatorelli, Gaetano Cairo, Luca Gianni. Anthracyclines: Molecular Advances and Pharmacologic Developments in Antitumor Activity and Cardiotoxicity. *Pharmacol Rev* 2004;56:185–229.
42. K. Bristol HRH, D.P. Berger, S.P. Langdon, H.H. Fiebig, and O. Fodstad. The Antitumour Activity of the Prodrug N-l-leucyl-doxorubicin and its Parent Compound Doxorubicin in Human Tumour Xenografts. *European Journal of Cancer* 1998;34(10):1602-1606.
43. Gopin A, Ebner S, Attali B, Shabat D. Enzymatic Activation of second-generation dendritic prodrugs: Conjugation of self-immolative dendrimers with PEG via click chemistry. *Bioconjugate Chem* 2006;17:1432-1440.
44. Shamis M, Lode HN, Shabat D. Bioactivation of self-immolative dendritic prodrugs by catalytic antibody 38C2. *JACS* 2004;126:1726-1731.
45. Lutz F, Tietze MN, Thomas Mollers, Roland Fischer, Karl-Heinz Glusenkamp, Manfred F. Rajewsky, and Eckhard Jahde. Proton-mediated Liberation of Aldophosphamide from a Nontoxic Prodrug: A Strategy for Tumor-selective Activation of Cytocidal Drugs. *Cancer Research* 1989;49:4179-4184.
46. J.Martin Brown WRW. Exploiting Tumor Hypoxia in Cancer Treatment *Nature Reviews Cancer* 2004;4:437-447.

47. Barbara M. Mueller WAW, Ralph A. Reisfeldt. Antibody Conjugates with Morpholinodoxorubicin and Acid-Cleavable Linkers. *Bioconjugate Chem* 1990;1:325-330.
48. Park J, Hong K, Kirpotin D, Colbern G, Shalaby R, Baselga J, et al. Anti-HER2 Immunoliposomes: Enhanced Efficacy Attributable to Targeted Delivery. *Clinical Cancer Research* 2002;8:1172–1181.
49. Vaupel P, Kallinowski, F., Okunieff, P., . Blood Flow, Oxygen and Nutrient Supply, and Metabolic Microenvironment of Human Tumors: A Review. *Cancer Research* 1989;49:6449-6465.
50. Ibsen S, Zahavy E, Wrasidlo W, Berns M, Chan M, Esener S. A Novel Doxorubicin Prodrug with Controllable Photolysis Activation for Cancer Chemotherapy. *Pharmaceutical Research* 2010;27(9):1848-1860.
51. Ibsen S, Zahavy E, Wrasidlo W, Hayashi T, Norton J, Su Y, et al. Localized In-Vivo Activation of a Photoactivatable Doxorubicin Prodrug in Deep Tumor Tissue. *Photochemistry and photobiology* 2013;In press.
52. Zhang L, Gu FX, Chan JM, Wang AZ, Langer RS, Farokhzad OC. Nanoparticles in medicine: therapeutic applications and developments. *Clinical Pharmacology & Therapeutics* 2007;83(5):761-769.
53. Gabizon A, Catane R, Uziely B, Kaufman B, Safra T, Cohen R, et al. Prolonged Circulation Time and Enhanced Accumulation in Malignant Exudates of Doxorubicin Encapsulated in Polyethylene-glycol Coated Liposomes. *Cancer Research* 1994;54:987-992.
54. Fujimoto JG. Optical coherence tomography for ultrahigh resolution in vivo imaging. *Nature biotechnology* 2003;21(11):1361-1367.
55. Cosgrove D. Ultrasound contrast agents: An overview. *European Journal of Radiology* 2006;60(3):324–330.
56. Korpanty G, Carbon JG, Grayburn PA, Fleming JB, Brekken RA. Monitoring response to anticancer therapy by targeting microbubbles to tumor vasculature. *Clinical Cancer Research* 2007;13(1):323-330.
57. Chin CT, Lance'e C, Borsboom J, Mastik F, Frijlink ME, Jong Nd. Brandaris 128: A digital 25 million frames per second camera with 128 highly sensitive frames. *Review of Scientific Instruments* 2003;74(12):5026-5034.
58. Goldberg BB, Liu J-B, Forsberg F. Ultrasound contrast agents: A review. *Ultrasound in Medicine & Biology* 1994;20(2):319–333.

59. Schutt EG, Pelura TJ, Hopkins RM. Osmotically Stabilized Microbubble Sonographic Contrast Agents *Acad Radiol* 1996;3:S188-S190.
60. Schutt EG, Klein DH, Mattrey RM, Riess JG. Injectable microbubbles as contrast agents for diagnostic ultrasound imaging: the key role of perfluorochemicals. *Angewandte Chemie International Edition* 2003;42(28):3218-3235.
61. Ferrara K, Pollard R, Borden M. Ultrasound Microbubble Contrast Agents: Fundamentals and Application to Gene and Drug Delivery. *Annu Rev Biomed Eng* 2007;9:415-447.
62. Borden MA, Pu G, Runner GJ, Longo ML. Surface phase behavior and microstructure of lipid/PEG-emulsifier monolayer-coated microbubbles. *Colloids and Surfaces B: Biointerfaces* 2004;35(3):209-223.
63. Kim DH, Costello MJ, Duncan PB, Needham D. Mechanical properties and microstructure of polycrystalline phospholipid monolayer shells: Novel solid microparticles. *Langmuir* 2003;19(20):8455-8466.
64. Shimanouchi T, Ishii H, Yoshimoto N, Umakoshi H, Kuboi R. Calcein permeation across phosphatidylcholine bilayer membrane: Effects of membrane fluidity, liposome size, and immobilization. *Colloids and Surfaces B: Biointerfaces* 2009;73(1):156-160.
65. Pu G, Borden MA, Longo ML. Collapse and shedding transitions in binary lipid monolayers coating microbubbles. *Langmuir* 2006;22(7):2993-2999.
66. Borden MA, Dayton P, Zhao S, Ferrara KW. Physico-chemical properties of the microbubble lipid shell [ultrasound contrast agents]. *Ultrasonics Symposium, 2004 IEEE; 2004: IEEE; 2004. p. 20-23.*
67. Kwan JJ, Borden MA. Lipid monolayer dilatational mechanics during microbubble gas exchange. *Soft Matter* 2012;8(17):4756-4766.
68. Chaudhuri KD. Concentration quenching of fluorescence in solutions. *Z Phys A-Hadron Nucl* 1959;154(1):34-42
69. Chen RF, Knutson JR. Mechanism of fluorescence concentration quenching of carboxyfluorescein in liposomes: energy transfer to nonfluorescent dimers. *Anal Biochem* 1988;172(1):61-77.

70. Druzhinin SI, Demyashkevich AB, Uzhinov BM. Concentration dependence of the quenching of the fluorescence of acridine cation in aqueous solutions. *J Appl Spectrosc* 1979;30(2):238-239.
71. Yuan B. Ultrasound-modulated fluorescence based on a fluorophore-quencher-labeled microbubble system. *J Biomed Opt* 2009;14(2):240-243.
72. Hsu MJ, Eghtedari M, Goodwin AP, Hall DJ, Mattrey RF, Esener SC. Characterization of individual ultrasound microbubble dynamics with a light-scattering system. *Journal of biomedical optics* 2011;16(6):0670021-0670024.
73. Guan J, Matula TJ. Using light scattering to measure the response of individual ultrasound contrast microbubbles subjected to pulsed ultrasound in vitro. *The Journal of the Acoustical Society of America* 2004;116:2832.
74. Dean CE, Marston PL. Critical angle light scattering from bubbles: an asymptotic series approximation. *Applied optics* 1991;30(33):4764-4776.
75. Feshitan JA, Chen CC, Kwan JJ, Borden MA. Microbubble size isolation by differential centrifugation. *Journal of colloid and interface science* 2009;329(2):316-324.
76. Borden MA, Martinez GV, Ricker J, Tsvetkova N, Longo M, Gillies RJ, et al. Lateral phase separation in lipid-coated microbubbles. *Langmuir* 2006;22(9):4291-4297.
77. Vickery SA, Dunn RC. Direct observation of structural evolution in palmitic acid monolayers following Langmuir-Blodgett deposition. *Langmuir* 2001;17(26):8204-8209.
78. Jin Z-H, Josserand Vr, Foillard Sp, Boturyn D, Dumy P, Favrot M-C, et al. In vivo optical imaging of integrin $\alpha_5\beta_1$. *Molecular cancer* 2007;6:41.
79. Yong K-T, Roy I, Law W-C, Hu R. Synthesis of cRGD-peptide conjugated near-infrared CdTe/ZnSe core-shell quantum dots for in vivo cancer targeting and imaging. *Chem Commun* 2010 46(38):7136-7138.
80. Cheong W-F, Prael SA, Welch AJ. A review of the optical properties of biological tissues. *Quantum Electronics, IEEE Journal of* 1990;26(12):2166-2185.
81. Gladkova ND, Petrova GA, Nikulin NK, Radenska Lopovok SG, Snopova LB, Chumakov YP, et al. In vivo optical coherence tomography imaging of human skin: norm and pathology. *Skin Research and Technology* 2000;6(1):6-16.

82. Li A, Kwong R, Cerussi A, Merritt S, Hayakawa C, Tromberg B. Method for recovering quantitative broadband diffuse optical spectra from layered media. *Applied optics* 2007;46(21):4828-4833.
83. Wang LV. Ultrasound-mediated biophotonic imaging: a review of acousto-optical tomography and photo-acoustic tomography. *Disease Markers* 2004;19(2):123-138.
84. Wang L, Jacques SL, Zhao X. Continuous-wave ultrasonic modulation of scattered laser light to image objects in turbid media. *Optics letters* 1995;20(6):629-631.
85. Leveque S, Boccara AC. Ultrasonic tagging of photon paths in scattering media: parallel speckle modulation processing. *Optics letters* 1999;24(3):181-183.
86. Wang LV. Mechanisms of ultrasonic modulation of multiply scattered coherent light: a Monte Carlo model. *Optics letters* 2001;26(15):1191-1193.
87. Mahan GD, Engler WE, Tiemann JJ, Uzgiris E. Ultrasonic tagging of light: theory. *Proceedings of the National Academy of Sciences* 1998;95(24):14015-14019.
88. Tu J, Guan J, Qiu Y, Matula TJ. Estimating the shell parameters of SonoVue microbubbles using light scattering. *The Journal of the Acoustical Society of America* 2009;126:2954.
89. Niu C-G, Gui X-Q, Zeng G-M, Yuan X-Z. A ratiometric fluorescence sensor with broad dynamic range based on two pH-sensitive fluorophores. *Analyst* 2005;130(11):1551-1556.
90. McEvoy AK, McDonagh CM, MacCraith BD. Dissolved oxygen sensor based on fluorescence quenching of oxygen-sensitive ruthenium complexes immobilized in sol-gel-derived porous silica coatings. *Analyst* 1996;121(6):785-788.
91. Zhang G, Palmer GM, Dewhurst MW, Fraser CL. A dual-emissive-materials design concept enables tumour hypoxia imaging. *Nature materials* 2009;8(9):747-751.
92. Helmlinger G, Yuan F, Dellian M, Jain RK. Interstitial pH and pO₂ gradients in solid tumors in vivo: high-resolution measurements reveal a lack of correlation. *Nature medicine* 1997;3(2):177-182.

93. Burns PN. Instrumentation for contrast echocardiography. *Echocardiography* 2002;19(3):241-258.
94. Burns PN, Powers JE, Hope Simpson D, Uhlendorf V, Fritzsche T. Harmonic contrast-enhanced Doppler as a method for the elimination of clutter: in vivo duplex and color studies. *Radiology* 1993;189:285.
95. Meade ML. Advances in lock-in amplifiers. *Journal of Physics E: Scientific Instruments* 1982;15(4):395.
96. Yuan B, Liu Y, Mehl PM, Vignola J. Microbubble-enhanced ultrasound-modulated fluorescence in a turbid medium. *Applied Physics Letters* 2009;95(18):181113-181113-181113.
97. Yao G, Wang LV. Theoretical and experimental studies of ultrasound-modulated optical tomography in biological tissue. *Applied Optics* 2000;39(4):659-664.
98. Driver I, Feather JW, King PR, Dawson JB. The optical properties of aqueous suspensions of Intralipid, a fat emulsion. *Physics in medicine and biology* 1989;34(12):1927.
99. Michels R, Foschum F, Kienle A. Optical properties of fat emulsions. *Optics Express* 2008;16(8):5907-5925.
100. Ibsen S, Schutt CE, Esener S. Microbubble-mediated ultrasound therapy: a review of its potential in cancer treatment. *Drug Design, Development and Therapy* 2013;7:1-15.
101. Lentacker I, Geest BGD, Vandenbroucke RE, Peeters L, Demeester J, Smedt SCD, et al. Ultrasound-Responsive Polymer-Coated Microbubbles That Bind and Protect DNA. *Langmuir* 2006;22(17):7273-7278.
102. Klibanov A. Microbubble Contrast Agents Targeted Ultrasound Imaging and Ultrasound Assisted Drug-Delivery Applications. *Investigative Radiology* 2006;41(3):354-362.
103. Unger E, McCreery T, Sweitzer R, Caldwell V, Wu Y. Acoustically Active Lipospheres Containing Paclitaxel: A New Therapeutic Ultrasound Contrast Agent. *Investigative Radiology* 1998;33(12):886-892.
104. Liu Y, Miyoshi H, Nakamura M. Encapsulated ultrasound microbubbles: Therapeutic application in drug/gene delivery. *Journal of Controlled Release* 2006;114:89-99.

105. Kheirrolomoom A, Dayton P, Lum A, Little E, Paoli E, Zheng H, et al. Acoustically-active microbubbles conjugated to liposomes: Characterization of a proposed drug delivery vehicle. *Journal of Controlled Release* 2007;118:275–284.
106. Collis J, Manasseh R, Liovic P, Tho P, Ooi A, Petkovic-Duran K, et al. Cavitation microstreaming and stress fields created by microbubbles. *Ultrasonics* 2010;50(2):273-279.
107. Kodama T, Tomita Y. Cavitation bubble behavior and bubble–shock wave interaction near a gelatin surface as a study of in vivo bubble dynamics. *Appl Phys B* 2000;70:139–149.
108. Bao S, Thrall BD, Miller DL. Transfection of a Reporter Plasmid Into Cultured Cells by Sonoporation in Vitro. *Ultrasound in Med & Biol* 1997;23(6):953-959.
109. Koch S, Pohl P, Cobet U, Rainov NG. Ultrasound Enhancement of Liposome-Mediated Cell Transfection is Caused by Cavitation Effects. *Ultrasound in Med & Biol* 2000;26(5):897–903.
110. Zarnitsyn V, Rostad C, Prausnitz M. Modeling Transmembrane Transport through Cell Membrane Wounds Created by Acoustic Cavitation. *Biophysical Journal* 2008;95(9):4124-4138.
111. Li ZG, Luo KQ, Ohl CD, Zhang JB, Liu AQ. A Single-Cell Membrane Dynamic from Poration to Restoration by Bubble-Induced Jetting Flow. 15th International Conference on Miniaturized Systems for Chemistry and Life Sciences 2011:94-96.
112. Okada K, Kudo N, Niwa K, Yamamoto K. A basic study on sonoporation with microbubbles exposed to pulsed ultrasound. *J Med Ultrasonics* 2005;32:3-11.
113. Ibsen S, Benchimol M, Simberg D, Schutt C, Steiner J, Esener S. A novel nested liposome drug delivery vehicle capable of ultrasound triggered release of its payload. *Journal of Controlled Release* 2011;155(3):358–366.
114. Schneider M. Characteristics of SonoVue™. *Echocardiography* 1999;16(s1):743-746.
115. Gaumet M, Vargas A, Gurny R, Delie F. Nanoparticles for drug delivery: the need for precision in reporting particle size parameters. *European journal of pharmaceutics and biopharmaceutics* 2008;69(1):1-9.

116. Feinstein SB, Shah PM, Bing RJ, Meerbaum S, Corday E, Chang B-L, et al. Microbubble dynamics visualized in the intact capillary circulation. *Journal of the American College of Cardiology* 1984;4(3):595-600.
117. Gabizon AA. Pegylated Liposomal Doxorubicin: Metamorphosis of an Old Drug into a New Form of Chemotherapy. *Cancer Investigation* 2001;19(4):424-436.
118. Laginha KM, Verwoert S, Charrois GR, Allen T. Determination of Doxorubicin Levels in Whole Tumor and Tumor Nuclei in Murine Breast Cancer Tumors. *Clin Cancer Res* 2005;11(19):6944-6949.
119. Miller MW, Miller DL, Brayman AA. A Review of In Vitro Bioeffects of Inertial Ultrasonic Cavitation from a Mechanistic Perspective. *Ultrasound in Med & Biol* 1996;22(9):1131-1154.
120. Brujan EA, Ikeda T, Matsumoto Y. Jet formation and shock wave emission during collapse of ultrasound-induced cavitation bubbles and their role in the therapeutic applications of high-intensity focused ultrasound. *Physics in medicine and biology* 2005;50(20):4797.
121. Crum LA. Surface Oscillations and Jet Development in Pulsating Bubbles. *Journal De Physique* 1979;40(11):285-288.
122. Wang QX, Yeo KS, Khoo BC, Lam KY. Nonlinear interaction between gas bubble and free surface. *Computers & fluids* 1996;25(7):607-628.
123. Chen H, Brayman AA, Kreider W, Bailey MR, Matula TJ. Observations of translation and jetting of ultrasound-activated microbubbles in mesenteric microvessels. *Ultrasound in medicine & biology* 2011;37(12):2139-2148.
124. Caskey CF, Stieger SM, Qin S, Dayton PA, Ferrara KW. Direct observations of ultrasound microbubble contrast agent interaction with the microvessel wall. *The Journal of the Acoustical Society of America* 2007;122:1191.
125. Stride E, Saffari N. Microbubble ultrasound contrast agents: a review. *Proceedings of the Institution of Mechanical Engineers, Part H: Journal of Engineering in Medicine* 2003;217:429-447.
126. Leighton TG. Bubble population phenomena in acoustic cavitation. *Ultrasonics Sonochemistry* 1995;2(2):S123-S136.
127. Ibsen S, Benchimol M, Esener S. Fluorescent Microscope System to Monitor Real-Time Interactions between Focused Ultrasound, Echogenic Drug Delivery Vehicles, and Live Cell Membranes. *Ultrasonics* 2012;In Press.

128. Miller DL, Thomas RM. Ultrasound Contrast Agents Nucleate Inertial Cavitation In Vitro. *Ultrasound in Med & Biol* 1995;21(8):1059- 1065.
129. Miele E, Spinelli GP, Miele E, Tomao F, Tomao S. Albumin-bound formulation of paclitaxel (Abraxane® ABI-007) in the treatment of breast cancer. *International Journal of Nanomedicine* 2009;4:99–105.
130. Gabizon A, Tzemach D, Mak L, Bronstein M, Horowitz AT. Dose dependency of pharmacokinetics and therapeutic efficacy of pegylated liposomal doxorubicin (DOXIL) in murine models. *Journal of drug targeting* 2002;10(7):539-548.
131. Johansen PB. Doxorubicin Pharmacokinetics after Intravenous and Intraperitoneal Administration in the Nude Mouse. *Cancer Chemother Pharmacol* 1981;5:267-270.
132. Pawan K. Singal NI. Doxorubicin-Induced Cardiomyopathy. *The New England Journal of Medicine* 1998 September 24;339(13):900-905.
133. Olson RD MP. Doxorubicin cardiotoxicity: analysis of prevailing hypotheses. *FASEB J* 1990;4(13):3076-3086.
134. Charrois G, Allen T. Multiple Injections of Pegylated Liposomal Doxorubicin: Pharmacokinetics and Therapeutic Activity. *J Pharmacol Exp Ther* 2003 306(3):1058-1067.
135. Judson I, Radford JA, Harris M, Blay JY, Van Hoesel Q, Le Cesne A, et al. Randomised phase II trial of pegylated liposomal doxorubicin (DOXILÂ®/CAELYXÂ®) versus doxorubicin in the treatment of advanced or metastatic soft tissue sarcoma: a study by the EORTC Soft Tissue and Bone Sarcoma Group. *European Journal of Cancer* 2001;37(7):870-877.
136. Gabizon A, Shmeeda H, Barenholz Y. Pharmacokinetics of pegylated liposomal doxorubicin. *Clinical pharmacokinetics* 2003;42(5):419-436.
137. Bao A, Goins B, Klipper R, Negrete G, Phillips WT. Direct 99mTc labeling of pegylated liposomal doxorubicin (Doxil) for pharmacokinetic and non-invasive imaging studies. *Journal of Pharmacology and Experimental Therapeutics* 2004;308(2):419-425.
138. Pasqualini R, Arap W, McDonald DM. Probing the structural and molecular diversity of tumor vasculature. *Trends in molecular medicine* 2002;8(12):563-571.

139. Rogers K. Blood: Physiology and Circulation: The Rosen Publishing Group, 2010.
140. Amit B, Zehavi U, Patchornik A. Photosensitive Protecting Groups of Amino Sugars and Their Use in Glycoside Synthesis. 2-Nitrobenzyloxycarbonylamino and 6-Nitroveratryloxycarbonylamino derivatives. *J Org Chem* 1974;39:192-196.
141. Ni T, Baudisch P. Disappearing mobile devices. Proceedings of the 22nd annual ACM symposium on User interface software and technology 2009; Victoria, British Columbia, Canada: Association for Computing Machinery; 2009. p. 101-110.
142. Miwa M, Ura M, Nishida M, Sawada N, Ishikawa T, Mori K, et al. Design of a novel oral fluoropyrimidine carbamate, capecitabine, which generates 5-fluorouracil selectively in tumours by enzymes concentrated in human liver and cancer tissue. *European Journal of Cancer* 1998;34(8):1274-1281
143. Yuanlong Yang EJC, Jason A. Koutcher, R.R. Alfano. UV Reflectance Spectroscopy Probes DNA and Protein Changes in Human Breast Tissues. *Journal of Clinical Laser Medicine & Surgery* 2001;19(1):35-39.
144. Sutherland J, Griffin, K. Absorption Spectrum of DNA for Wavelengths Greater than 300 nm. *Radiation Research* 1981;86(3):399-410.
145. J. Elisseeff KA, D. Sims, W.McIntosh, M. Randolph, and R. Langer. Transdermal photopolymerization for minimally invasive implantation. *Proc Natl Acad Sci* 1999;96:3104-3107.
146. Botvinick EL, Berns MW. Internet-based robotic laser scissors and tweezers microscopy. *Microscopy research and technique* 2005;68(2):65-74.
147. Gary J. Quigley AH-JW, Giovanni Ughetto, Gijs Van Der Marel, Jacques H. Van Boom, and Alexander Rich. Molecular structure of an anticancer drug-DNA complex: Daunomycin plus d(CpGpTpApCpG). *Proc Natl Acad Sci USA* 1980;77(12):7204-7208.
148. Ji J, Rosenzweig N, Jones I, Rosenzweig Z. Molecular oxygen-sensitive fluorescent lipobeads for intracellular oxygen measurements in murine macrophages. *Analytical chemistry* 2001;73(15):3521-3527.